



ÉCOLE
POLYTECHNIQUE
DE BRUXELLES

UNIVERSITÉ LIBRE DE BRUXELLES

Active Vibration Isolation System for Space Applications

Thesis presented by Vicente Aulë LAFARGA NEBOT

with a view to obtaining the PhD Degree in Engineering Sciences and
Technology ("Docteur en Sciences de l'Ingénieur et Technologie")
Academic year 2023-2024

Supervisor : Professor Christophe COLLETTE
[BEAMS Department]

Thesis jury :

Prof. Christophe COLLETTE (Université libre de Bruxelles and Université de Liège, Supervisor)

Prof. Patrick HENDRICK (Université libre de Bruxelles, Chair)

Prof. Arnaud DERAEMAERKER (Université libre de Bruxelles, Secretary)

Dr. Gonçalo RODRIGUES (Structures Engineer at European Space Agency)

Prof. Emeline SADOULET-REBOUL (Université de Franche-Comté)



Abstract

Mechanical vibrations propagating through the structure of a spacecraft can be detrimental to mission success whether by presenting a direct threat to the structural integrity of the spacecraft and sensitive scientific instruments during launch, or, in the case of much smaller amplitude loads called microvibrations, by inducing jitter of the line-of-sight of instruments and increasing noise levels of observations.

The transmission of such harmful vibrations can be mitigated by mounting sensitive payloads or sources of disturbance on passive isolating suspensions. While these passive systems are effective in filtering the vibrations occurring at frequencies above their own resonance, they end up amplifying the disturbances occurring at the suspension modes themselves. The curbing of the responses of these suspension modes can be achieved by resorting to elastomeric materials, but this approach is often accompanied by a degradation of the higher frequency isolation.

Alternatively, active vibration isolation systems present the big advantage of virtually eliminating the amplification by the suspension modes, while at the same time not degrading the high-frequency isolation present in undamped suspensions. This thesis investigates innovative concepts for active vibration isolation systems suited to spacecraft. It is based on soft suspensions, in which the load-path consists of integrated sensors and actuators, and therefore privilege simplicity, reliability, low mass and low power consumption which are essential characteristics for a space equipment. Two distinct applications were addressed.

For the case of reduction of the high mechanical loads generated by launch vehicles and imposed on spacecraft, the concept of a hybrid isolator was explored. By adding a passive layer in parallel to an active system developed earlier, which consists of piezoelectric stack shunted to a resistive-inductive load. This configuration allows to dissipate part of the mechanical energy in the system, reducing the power consumption of the active system, while at the same time providing fallback-damping performances in case of failure of the active component.

The second application provided filtering of microvibrations. It was implemented

as a Stewart Platform with its six legs formed by non-contact voice-coil actuators. These voice-coil actuators are self-sensing, in which the monitoring of their voltage and current produces an estimate of the relative velocity of the two sides of the platform and enables the active damping of the suspension modes.

The concept was validated experimentally with the test model of a reaction wheel and an isolation performance of -65 dB was obtained at 270 Hz. This consists of an improvement with relation to the vibration isolation systems described in the state-of-the art of space applications.

Keywords: Vibration isolation – Active control – Microvibrations – Payload comfort – Stewart platform

Acknowledgements

First and foremost I want to thank Prof. Christophe Collette for making all of this happen. He took a gamble on an Erasmus student back in 2016 with a master thesis proposal to continue the investigations into an active isolation system for payloads onboard launchers, and the rest, as they say, is history. It's been a long and winding road to get to where we are, but he has taught me that with a solution-oriented attitude, anything can happen. Thank you not only for showing to me how much I didn't know, but for actually taking the time to teach me. And oh boy did I learn. There is a graph somewhere that relates how much people think they know, and how much they actually know as they progress through life, and I feel like in the timeframe of one PhD I have gone through all the phases in that graph. So thank you for giving me the opportunity to do it. None of this would have been possible without your help and support.

I am also very grateful to Dr. Gonçalo Rodrigues, your extreme kindness and knowledge of space-systems has proven invaluable for the development of this thesis, and to my enjoyment carrying it out. Thank you for all the discussions, all your help, and your well timed injections of motivation into this project. It has been a pleasure working with you. I must also not forget to thank Dr. René Seiler and Florian Liebold, who took me in and allowed me to play for hours on end at their laboratory. Thank you for showing me the ropes, and for the deep dives into the world of reaction-wheel borne microvibrations. Thanks to them I now understand the beauty of waterfall plots.

I would also like to thank Prof. Arnaud Deraemaeker, aka "the most involved CA member in the history of CA members". Thank you for all the discussions about impact hammer testing and post-processing, thank you for all the time spent on SDT showing me how to play with condensed models, and thank you for always being available whenever I needed your help. I would also like to thank Prof. Patrick Hendrick for agreeing to listen to me ramble about springs at the end of each academic

year and accepting to be a part of my jury. I would also like to thank Prof. Emeline Sadoulet-Reboul for participating as a jury member in the revision and defense of my thesis.

As someone close to me likes to say, you actually get two salaries when work. The first one is the money you get in the bank. The second one is how you feel, as a function of the pleasure you get from actually going to work. In this regard, I am extremely happy, and it's thanks to all of my colleagues from the UC2 lab, who made this a wonderful experience. Jennifer Watchi, Loïc Amez-Droz, Mateo Tunon de Lara, Dimitri Piron, Mohit Verma, Ahmad Paknejad, Thomas Dehaeze, Clément Rigaut, Youness Tourtit, Franco Piñan, Adam Chafaï, Binlei Ding, Guoying Zhao, Haidar Lakkis, Anthony Amorosi and Cédric Dumoulin, this experience would not have been the same if I had not had the chance of sharing it with you. My work on this project was only possible thanks to the people that laid the groundwork, and collaborated with me throughout it, and for that I would like to thank: Adrien Souleille, Thibault Lampert, Sylvain Hellegouarch, Alan Rondnieau, Vincent Gadanho, Maël Baron and Thomas Causeret. I must also not forget the supporting cast, doing all the work behind the scenes: Arianne Ducornez, Anne-Cécile Muffat and Natascha Vander Heyden. Thanks to Jean Salvatore Mele and Geoffrey Vanbienne for their enthusiasm and willingness to fabricate crazy designs while letting me play in their fantastic workshops. And a big thank you to Axel Dero for all his IT support and teachings about communication protocols.

I would like to thank all of my friends and family for the invaluable support that they have given me throughout my life, and especially during the course of this thesis. "When will you finish?" I finally have an answer to that :). I love you all very much. Finally, a very special thank you to my partner, Esther Herranz: the champion of patience, the queen of encouragement, the bringer of joy. Thank you for doing what you do, thank your making the bad times good, and the good times great.

The research presented in this manuscript has been possible thanks to the funding provided by the Networking and Partnership Initiative from the European Space Agency under the contract NPI DNI 14894.

"If you want to find out the secrets of the universe, think in terms of energy, frequency and vibration"

-Nikola Tesla

Contents

List of Figures	ix
List of Tables	xvii
1 Introduction	2
1.1 Background	2
1.1.1 Payload comfort demonstrator	4
1.1.2 Micro-vibration isolation demonstrator	5
1.2 Thesis outline	6
1.3 Original aspects of this thesis	7
2 Isolation systems onboard spacecraft	8
2.1 Motivation	9
2.2 Disturbance reduction principles	9
2.2.1 Passive disturbance reduction	9
2.2.2 Active disturbance reduction principles	16
2.2.3 Hybrid disturbance reduction principles	18
2.3 Disturbance rejection during launch	18
2.4 Disturbance reduction during orbit and operation	21
2.4.1 Strategies	23
2.5 Multi-DOF Stages	29
3 Whole Spacecraft Vibration Isolation	34
3.1 Active vibration isolator	35
3.1.1 Single degree of freedom isolator	37
3.1.2 Flexible payload mounted on three isolators	38
3.1.3 Mounting on flexible supports	43
3.1.4 Summary	44

CONTENTS

3.2	Hybrid vibration isolator	44
3.2.1	Isolator architecture	46
3.2.2	Shunt selection	49
3.2.3	Criteria for parameter selection	53
3.2.4	Summary	56
4	Active Isolator for micro-vibrations	58
4.1	Motivation	59
4.2	Isolator Design	60
4.2.1	Brief description of the isolator	60
4.2.2	Struts	61
4.2.3	Supporting springs	63
4.2.4	Active control	70
4.3	Isolator Performance	76
4.3.1	Single DOF Experimental Characterization	76
4.3.2	Multi-DOF Experimental Characterization	80
4.3.3	Supplementary Tests	92
4.4	Payload Comfort Operating Mode	98
4.5	Conclusions	102
	Conclusions and Perspectives	103
	References	110
	Appendices	119
A	Equivalence of Force and Motion Transmissibilities	120
B	Current Injector Diagram	123

List of Figures

1.1	Effect of micro-vibrations on image capture. Left to right: decreasing levels of micro-vibrations [1]	3
1.2	From left to right: Concept of active isolator; Picture of an APA 100M from Cedrat-Technologies used for the experiments (one piezoelectric stack is used as a force sensor and the other one is used as an actuator)	5
1.3	(a) 3D model of the isolator with the actuators highlighted in dark blue; (b) isolator with reaction wheel in operating conditions	6
2.1	1 degree-of-freedom mass-spring-dashpot system of mass m , stiffness k and damping c	10
2.2	Motion and Force transmissibilities and Compliance transfer function. Note the equal magnitude of the transmissibilities with the negative sign represented by the 180° phase shift	11
2.3	Effect on the transmissibility of reducing the stiffness by up to a factor 5. Note how the magnitude at 100 Hz decreases with each successive reduction in stiffness, improving the isolation of the system	12
2.4	Effect on the compliance of reducing the stiffness by up to a factor 5. Note how the magnitude at DC increases with each successive reduction in stiffness, degrading the resistance to motion for a given input force	13
2.5	Picture of the inside of a washing machine with diagram for illustrative purposes. Note the suspension spring connecting the drum and the chassis for vibration isolation purposes	14
2.6	Effect on the transmissibility of increasing the damping. Note how increasing the damping decreases the magnitude at resonance, but increases the magnitude at high frequency	15
2.7	Installation of a whole-spacecraft vibration isolation system [2]	19

LIST OF FIGURES

2.8	Comparison of the measured responses of an instrument without isolation at the interface (red curve) and with isolation at the interface (pink curve) [3]	20
2.9	Control Structure Interaction (CSI) Testbed, where optical payload simulator is mounted onto the spacecraft using a passive/active hexapod isolator comprised of six long-stroke actuators [4]	20
2.10	Prototype of a whole spacecraft active isolation system using curved beams and voice coils [5]	21
2.11	Full isolation system with reaction wheel [6] (left) and isolator spring-damper element cutaway (right) [7].	25
2.12	Thales Alenia Space Reaction Wheel Isolator (left) fitted with a Rockwell Collins Deutschland reaction wheel (right) [8]	25
2.13	Reaction wheel isolation assembly, with the spring elements mated to the cradle and bottom bracket	26
2.14	Spacecraft bus, isolator strut assembly, tower and primary mirror backplane [9]	28
2.15	Details of the isolator strut assembly [9]	29
2.16	A multi-supported platform	30
3.1	From left to right: Concept of active isolator; Picture of an APA 100M from Cedrat-Technologies used for the experiments (one piezoelectric stack is used as a force sensor and the other one is used as an actuator); Simplified model of a one DOF payload mounted on such isolator	36
3.2	Matrix of transfer functions from input (w,f,F) to output (F_s, x_1) in open loop (blue curves) and closed loop (dashed red curves)	38
3.3	Experimental setup showing the active mount with a dummy mass on top	39
3.4	Open loop and closed loop transfer function between the actuator and the force sensor. Comparison between the model (solid curve) and the experiment (dashed curve)	39
3.5	Single DOF system. Comparison between the theoretical (solid curve) and the experimental (crosses) root-locus	40
3.6	Right: Picture of the experimental set-up. It consists of a flexible payload mounted on a set of three isolators. Left: a simplified sketch of the set-up, showing only the vertical direction	40
3.7	Mode shapes and corresponding resonance frequencies of the first 6 modes	41

3.8	Vertical excitation. Top left: transfer function between the shaker noise and one force sensor; bottom left: integrated (downwards) RMS value of the force measured by one force sensor; top right: transmissibility between the table top w and m_2 ; bottom right: transmissibility between the table top w and m_1	42
3.9	Horizontal excitation. Top left: transfer function between the shaker noise and one force sensor; bottom left: integrated (downwards) RMS value of the force measured by one force sensor; top right: transmissibility between the horizontal motion of the table top (u) and horizontal motion of m_2 (y_2); bottom right: transmissibility between the horizontal motion of the table top (u) and horizontal motion of m_1 (y_1)	42
3.10	Flexible payload mounted on a set of three isolators, including a flexible structure below the isolator: picture and simplified sketch showing only the vertical direction	43
3.11	Transmissibilities x_1/x_0 and x_2/x_0 between the flexible support and the payload for various values of the control gain, when the structure is excited in the vertical direction	44
3.12	Piezoelectric stack with shunt connection (S_s) and the two shunt options studied: Resistive (R) and Resistive-Inductive (RL)	45
3.13	Root locus of experimental (crosses) and analytical results (solid line) of the active isolator in 3.1 where the sensor stack is shunted with a resistance	45
3.14	Schematic of the series (left) and parallel (right) hybrid isolator configurations. S_s represents the shunted piezoelectric stack	46
3.15	Root locus showing the correlation between resistance and damping, where the location of the pole connecting the yellow and green loops is a function of the value of the resistance in the shunt	48
3.16	Transmissibility between the two sides of the isolators shown in Fig. 3.14, where the control gain and shunt parameters have been tuned for equal behavior and performance	48
3.17	Control effort required to drive the actuator with the different strategies, to achieve the performance levels seen in Fig. 3.16	49
3.18	Transmissibility of the 1-DOF model for the different strategies	50
3.19	Control effort required to drive the actuator with the different strategies to achieve the performances shown in Fig. 3.18	50

LIST OF FIGURES

3.20	Schematic of the 2-DOF model in the parallel configuration	51
3.21	Transmissibility of the 2-DOF model for the different strategies	52
3.22	Control effort required to drive the actuator with the different strategies to achieve the performances shown in Fig. 3.21	53
3.23	Relationship between stiffness ratio and control effort (F_s/w in N/m) for equal transmissibility performance	54
3.24	Relationship between damping and control effort (F_s/w in N/m) for varying the stiffness ratios. First mode	55
3.25	Relationship between damping and control effort (F_s/w in N/m) for varying the stiffness ratios. Second mode	55
3.26	Damping of the first mode as a function of the second mode, for different control effort ($CE = F_s/w$ in N/m)	56
4.1	(a) 3D model of the isolator with the actuators highlighted in dark blue; (b) isolator with reaction wheel in operating conditions	61
4.2	Schematic views of the cubic configuration of a Stewart platform. (a) Isometric view; (b) top view	62
4.3	Full view and cross-section of example models of a) a guided voice coil actuator, where the flexure ensures the co-linear motion between the magnet and the coil; b) a frameless voice coil actuator without a guiding system as implemented in the concept described in this article.	63
4.4	CAD view of actuator support. (a) Front view; (b) rear view	64
4.5	CAD view of source plate indicating the spring locations.	64
4.6	FEA of the brackets suspending the top plate showing the first local deformation mode at 1395 Hz.	66
4.7	CAD view of different suspension system configurations. (a-b) On-ground clamp system and mounting configuration; (c-d) zero-g clamp system and mounting configuration	67
4.8	Test setup to evaluate the spring's stiffness. Left to right: clamped static force sensor, spring assembly, horizontal translation stage.	67
4.9	Force (blue) and stiffness (red) of each spring assembly consisting of two springs in parallel as a function of the induced extension. The average stiffness for each spring assembly can be found in the subtitle. The natural length of the springs is 19 mm	68

4.10	Test setup to evaluate the dynamics of each spring assembly. From left to right: electrodynamic shaker, piezoelectric force sensor, spring assembly, piezoelectric force sensor, blocked end.	69
4.11	Force transmissibility, phase, and coherence for each spring assembly pair. A resonance can be seen at low frequency corresponding to the moving mass of the shaker, followed by a -40 dB/dec roll-off, with resonances of the test setup appearing at 200 Hz and 315 Hz. The local deformation modes of the springs can be seen between 500 - 700 Hz.	69
4.12	Picture of the setup used to validate the self-sensing technique. A beam clamped at one end is fitted with a voice coil at its free end with a laser vibrometer recording the velocity at the same location. The voice coil serves both as an actuator and as a sensor	72
4.13	Velocity of the free end of the beam shown in Fig. 4.12 showing a good match between the reference velocity and the self-sensed velocity 72	72
4.14	Block diagram representation of the active control loop. Note that decentralized control is used, with each voice-coil actuator working independently	73
4.15	Open loop transfer function between the self-sensed velocity and the force injected in one actuator showcasing alternating poles and zeroes 74	74
4.16	Bode plot of the controller used in decentralized loops at each voice-coil actuator	75
4.17	Loop gain and stability margins of the system obtained by multiplying the open loop transfer function by the controller	76
4.18	Experimental setup at ULB to verify the platform's passive and active isolation performance. The platform is mounted through an adapter plate on an electrodynamic shaker (1). Two accelerometers are coaxially placed along the center axis of the platform to compute the transmissibility, (2) at the base of the isolator (hidden in the picture) to record the input motion, and (3) on top of the RW dummy to record the output motion.	77
4.19	Experimental transmissibility of the isolator in axial direction. The response of the passive system is shown in blue, attaining 60 dB of isolation at 100 Hz, while the response of the active system is shown in red and puts in evidence the damping of the suspension mode . . .	79

LIST OF FIGURES

4.20	Isolator performance characterization setup showing the cable routing solution. The isolator and reaction wheel are mounted on a dynamometric Kistler table which is bolted on an optical table supported by pneumatic isolators	80
4.21	Force and torque PSD of the background noise in the experimental room. [unit] corresponds to N for the forces and Nm for the torques. The peaks observed between 20 - 50 Hz correspond to environmental noise and are present in all the measurements	81
4.22	Huddle test results in the X direction, showing the coherent portion of the signal in blue indicating measured quantities, and the incoherent portion of the signal in red giving an indication of the level of the resolution of the sensors	82
4.23	Force transmissibility of the Kistler table, showing that they have no impact until 300 Hz on the recorded measurements	83
4.24	Assessment of RW cable impact on the isolator's dynamics. An equal excitation is injected in every voice coil resulting in a purely vertical excitation which is recorded by an accelerometer on top of the reaction wheel	84
4.25	Assessment of RW cable impact on the isolator's dynamics. Multi-directional excitation is created by injecting current in one voice coil and recording the motion with a second coil in self-sensing mode. The vertical axis shows the transfer function between the injected force and the measured relative velocity. The low impact of the reaction wheel cable is observed	85
4.26	Plant identification showcasing a comparison between the results obtained at ULB (blue) and at ESTEC with (yellow) and without the RW cable (red). Although there are differences in the frequency of two of the poles and zeroes, they are insignificant towards the performance of the active control	86
4.27	Power spectral density of Forces ($U = N$) and Moments ($U = Nm$) measured in the hard-mounted configuration. The effect of the unbalance on the measured signals can be seen in the slope from low frequency up to 130 Hz	87
4.28	Power spectral density of Forces ($U = N$) and Moments ($U = Nm$) with the reaction wheel mounted on the isolator. Control off. The effect of the unbalance is compensated by the roll-off of the isolator	88

4.29	Power spectral density of Forces ($U = N$) and Moments ($U = Nm$) with the reaction wheel mounted on the isolator. Control on. Damping of the low frequency resonances can be observed.	89
4.30	Test configurations to compute the force transmissibility of the isolator. (a) Hard-mounted configuration used as reference; (b) Isolated configuration used for measuring disturbances with isolation platform.	89
4.31	Force PSD in the X direction for independent passive coast downs from 7800 rpm, illustrating the repeatability of the disturbances created during a passive coast down of the reaction wheel	90
4.32	(a) Power spectral density of the force in the X-direction. The background noise dominates the signal between 20 - 50 Hz and after 130 Hz; (b) corresponding transmissibility with and without control, showcasing an increase at 130 Hz due to the abrupt decrease of the magnitude of the input excitations, which when isolated is limited by the resolution of the sensors. This results in an inaccurate representation of the transmissibility above 130 Hz	91
4.33	Transmissibility comparison, control off and control on for each direction ($X, Y, Z, \theta_x, \theta_y$). Isolation of -60 dB at 130 Hz, limited by background noise >130 Hz.	93
4.34	(a) Picture of the experimental setup with shaker vertically mounted on the reaction wheel; (b) corresponding diagram	94
4.35	Power spectral density of the forces in the vertical direction measured at the shaker and at the dynamometer, with the background noise measurement to check the effectiveness of the input excitation	95
4.36	Zoomed in (90 - 1000 Hz) force transmissibility in the vertical direction showing a reduction in the transmissibility of 65 dB at 270 Hz, and an increase towards 400 Hz due to the resonance of the Kistler table in the vertical direction	95
4.37	Contour plots of the Force PSD as a function of wheel speed and frequency. Columns = output directions, rows = setup configuration.	97
4.38	Waterfall plot of the force in the Z direction during a stepped spin-up with increments of +100 rpm at 60 s intervals showing the effectiveness of the active control in the vertical (Z) direction. Control off (blue), control on (red).	98
4.39	Comparison between the qualification requirements and the recreated input signal PSD	100

LIST OF FIGURES

4.40	Uncontrolled and controlled motion transmissibilities of the isolator	100
4.41	Uncontrolled and controlled stroke of the system when applying the random input shown in Fig. 4.39	101
4.42	Actuator force required to achieve the performances shown in Fig's 4.40- 4.41	101
A.1	1 DOF system with base motion and input forces as inputs, and mass motion and transmitted force as outputs	120
B.1	Current injector developed by Michel Osée	123

List of Tables

2.1	Numeric values used to evaluate the one-dof system shown in Fig. 2.1	11
4.1	Parameters chosen for the design of the springs in spring steel EN-10270-3 Type 302.	65
4.2	Numeric values from the actuator's datasheet [10] used to estimate the self-sensed velocity according to Eq. 4.6 for the voice coil shown in Fig. 4.12	71

Chapter 1

Introduction

1.1 Background

Mechanical vibrations propagating through the structure of a spacecraft can be detrimental to mission success in multiple ways. On one hand, forces generated by the launch vehicle are a direct threat to the structural integrity of sensitive scientific and commercial payloads and even support the equipment in the satellite platforms. The most severe dynamic loads arise from the ignition of the motors, the pressure fluctuations in the booster, and the separation of stages, which can then excite the resonance frequencies of the spacecraft. On the other hand, extremely low-amplitude loads, in the order of micro- or milli-g, generated by on-board mechanisms functioning during spacecraft operations can become equally detrimental to the successful accomplishment of the mission. These disturbances are broadband, propagate through the spacecraft structure being amplified by their lightly damped resonances, and can reach payloads with sufficient amplitude to destabilize the line-of-sight or fully compromise signal-to-noise ratios. An example of the effect of micro-vibrations on the performances of an imager is presented in Fig. 1.1, where the image quality can be seen to improve as the level of microvibrations in the spacecraft is reduced.

In order to reduce the transmission of these dynamic forces, sensitive payloads or disturbing sources can be mounted on passive isolating suspensions, comprising passive-only elements that filter-out loads occurring at frequencies above the resonance frequency of the suspension. However, this reduction of transmissibility at higher frequencies comes at the expense of harmful amplifications of the disturbances at the suspension modes themselves, where the payload or disturbance source bounce on the flexibility of the suspension. To some extent, the amplification by the suspension modes can be mitigated by increasing the damping with passive

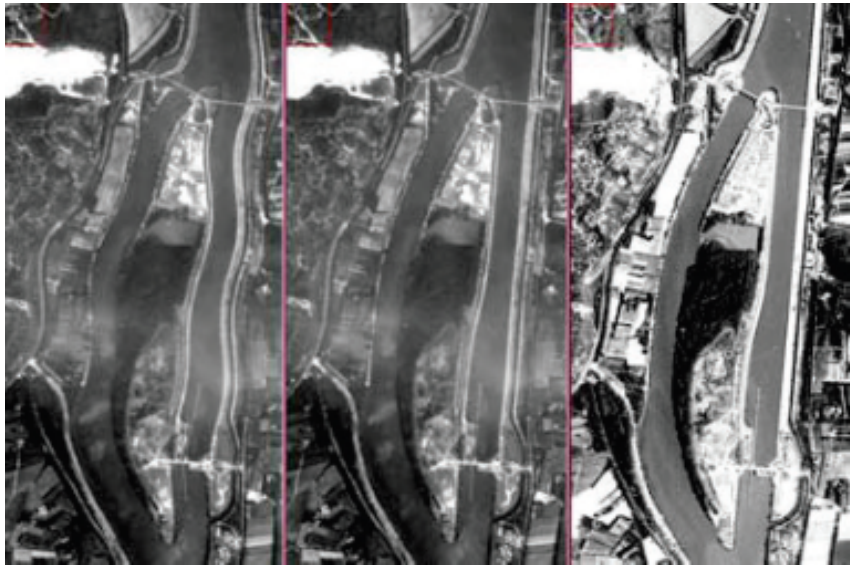


Figure 1.1: *Effect of micro-vibrations on image capture. Left to right: decreasing levels of micro-vibrations [1]*

components, usually by means of elastomers. However, typical implementations of passive damping tend to reduce the effectiveness of the higher frequency isolation.

The big advantage of active isolation systems resides in their capability to very effectively reduce or eliminate the amplification at the resonance, with a reduced impact on the roll-off of transmissibility at the frequencies above it. But such enhanced isolation performance comes at the expense of added complexity of the system in the form of sensors, actuators, the required control electronics and power sources. Furthermore, closed-loop systems must be designed and validated robustly in order to prevent dynamic instabilities and ending up actually amplifying the disturbances they are aimed to curb.

Any active vibration isolation or damping system that is suited to embark on, or be interfaced with a spacecraft, must therefore be subject to simplicity, reliability and lightweight design drivers. Therefore, concepts showing multi-function integration, and collocation among sensors, actuators, and structural elements and minimizing energy consumption, e.g. by resorting to its harvesting in the environment, must be privileged when designing active vibration cancellation systems for space systems must be privileged.

This thesis summarizes the investigations carried out in innovative concepts showing the potential for making active vibration isolation systems more attractive to be integrated into spacecraft. Two different configurations were explored addressing two very different types of requirements. One aims at reducing the high mechanical loads generated by Launch Vehicles and imposed on spacecraft, in what is termed as

enhancement of Payload Comfort. While the second one consists of filtering the micro-vibrations arising from the more modest disturbance forces and moments generated by reaction wheels, which are a recurrent actuator of Attitude and Orbital Control Systems of many spacecraft. Nonetheless, the two systems developed to tackle these two different applications of vibration isolation share the main architectural features, as both consisted of soft suspensions, in which the elements forming the unavoidable load path between source and payload consisted of integrated sensors and actuators, which were collocated to provide guaranteed stability during closed-loop operation.

1.1.1 Payload comfort demonstrator

The isolation suspension developed to provide payload comfort was conceived as a modular system consisting of a replication of active elements consisting of piezoelectric stacks integrated with elliptical metallic flexures that amplify their force. The commercially available elliptically amplified piezoelectric stacks were modified in that the piezoelectric element was split into two independent stacks, one stack being used as a force sensor, and the other as a force actuator. The resulting concept is shown in Fig. 1.2.

The control loops connecting the sensors to the actuators consisted of independent and decentralized Integral Force Feedback. The system was experimentally validated with three isolator active elements, but which could be modularly increased to accommodate satellites with a larger mass. The satellite was represented by a dynamic model consisting of dummy masses interconnected by flexible metallic blades and was sized to show the natural frequencies representative of those of a small spacecraft. The setup was excited with random white noise exciting all the modes of the system simultaneously, and the effectiveness of the Integral Force Feedback was put in evidence by enabling a reduction of the transmissibility by more than a factor of 10 at the resonances of the suspension modes and the flexible modes of the model representing the spacecraft.

As part of this thesis, the concept of a hybrid isolator was explored with the objective of reducing the power consumption, while at the same time providing fallback-damping performances in case of failure of the active part and increasing the inherent stiffness of the system. It consisted of adding a passive layer in parallel to the active system described just above, which consists of a shunted piezoelectric stack, which instead of being connected to a power supply is connected to a resistive-inductive load and transducers, extracts and dissipates part of the mechanical energy the system.

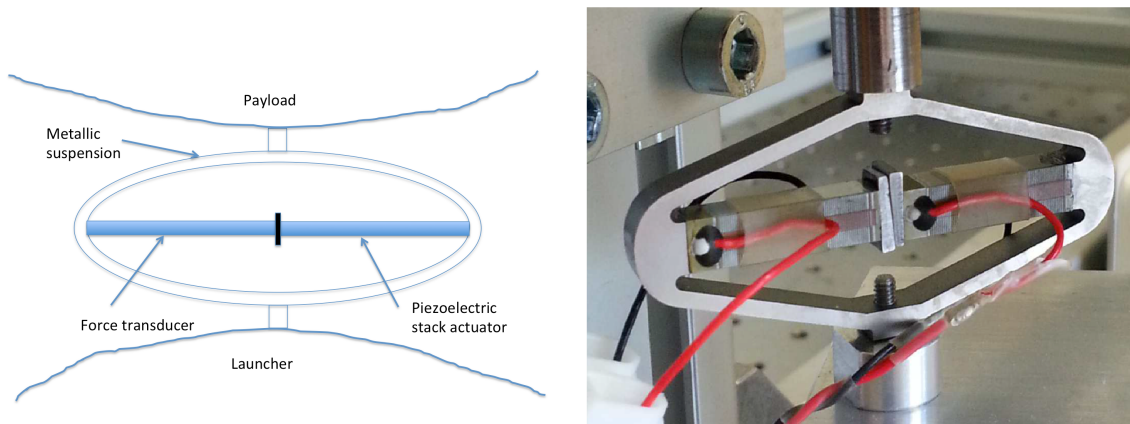


Figure 1.2: *From left to right: Concept of active isolator; Picture of an APA 100M from Cedrat-Technologies used for the experiments (one piezoelectric stack is used as a force sensor and the other one is used as an actuator)*

1.1.2 Micro-vibration isolation demonstrator

Additionally, an innovative concept of an active isolation platform for micro-vibrations was successfully developed and validated. The working principle consisted of the introduction of a suspension mode at low frequencies, i.e., around 5 Hz, and while the natural roll-off enabled high levels of isolation at high frequency, the amplification of the suspension modes was artificially damped with active control. The architecture of this isolation system is based on a Stewart Platform with the two sides of the platform interacting isostatically in the six degrees-of-freedom via frameless voice coil actuators, while the suspension modes were ensured by means of soft springs. The voice coil actuators are self-sensing, in which the monitoring of their voltage and current produces an estimate of the relative velocity of the two sides of the platform, thereby enabling the active damping of the suspension modes. A CAD view of the isolation platform is presented alongside a picture of the built system in Fig. 1.3.

The isolation platform was initially tested at the Precision Mechatronics Laboratory (PML) at Université Libre de Bruxelles (ULB), which allowed for tuning of the active control parameters. The setup was then moved to the Mechanisms Laboratory at the European Space Research and Technology Centre (ESTEC) site of the European Space Agency for testing with a test model of a reaction wheel. An isolation performance of -65 dB was attained at 270 Hz, which consisted of an improvement in the performance in relation to the vibration isolation systems described in the state-of-the-art of space applications.

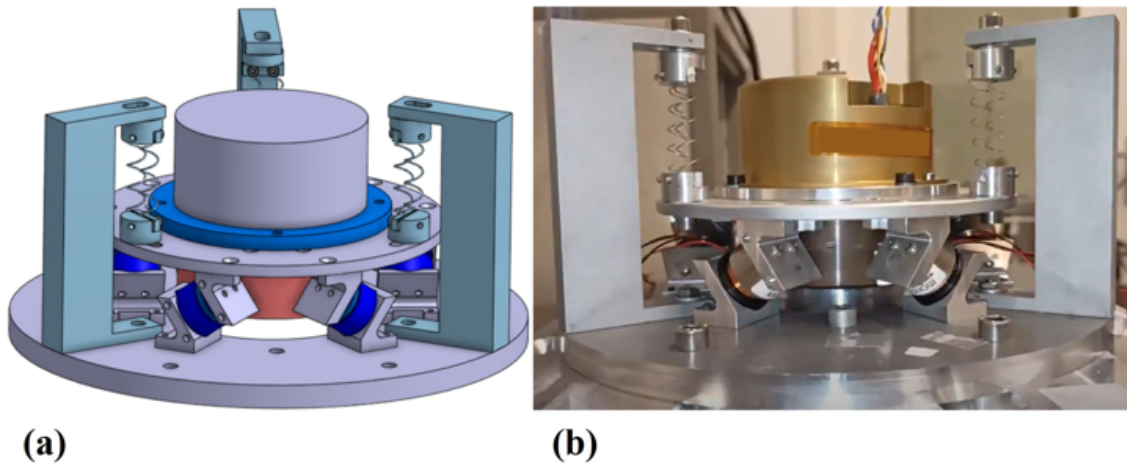


Figure 1.3: (a) 3D model of the isolator with the actuators highlighted in dark blue; (b) isolator with reaction wheel in operating conditions

1.2 Thesis outline

The thesis is organized into four parts.

Chapter 1 introduces the principles, of passive, active, and hybrid vibration isolation, and then reviews the state-of-the-art of disturbance rejection systems tailored to provide Payload Comfort during launch and mitigate micro-vibrations during operation.

Chapter 2 reports the research activities carried out in the scope of Payload Comfort applications, describing the design, assembly, and testing of a demonstrator of an active vibration isolator to be introduced at the level of the interface of a spacecraft. It consists of the modular assembly of active flexures and implementing the control law of Integral Force Feedback. The chapter then concludes the investigations on adding a passive element in the form of a resistive-inductive shunt to dissipate the energy from the mechanical disturbances.

Chapter 3 describes the development and testing of the vibration isolation system for micro-vibrations generated by reaction wheels. It consists of a Stewart-Gough platform with six legs consisting of frameless self-sensing voice coils which enable the mechanical decoupling between the two sides of the platform and provide active damping of the suspension modes. Furthermore, this chapter assesses the feasibility of extending the system to also mitigate the launch loads for the payloads and equipment for which it primarily aims at canceling the micro-vibrations.

Chapter 4 draws on the conclusions and sketches the perspectives for future work on the concepts researched.

1.3 Original aspects of this thesis

This thesis describes the introduction and validation of several novel concepts in active vibration isolation of space applications. Both for enabling payload comfort in the face of the mechanical launch environment, and to protect sensitive payloads during in-orbit operation from spacecraft-borne disturbances.

For the payload comfort application, the research reported in this thesis builds on the concept previously developed by the PML group of an isolation platform consisting of the modular assembly of active flexures formed by elliptically amplified piezoelectric stack split into independent sensor and actuator parts installed in series. This research led to a new configuration flexure with a third piezoelectric stack shunted to a resistor and an inductance and with a performance optimized thanks to the development of specialized metrics.

The Stewart-Gough platform developed for micro-vibration isolation was implemented by means of frameless voice coils which operate in self-sensing mode, which is considered to be a novel approach. This choice of architecture lead to a system showing extreme simplicity with isolation performances superior to those reported on the literature.

Chapter 2

Isolation systems onboard spacecraft

Contents

2.1	Motivation	9
2.2	Disturbance reduction principles	9
2.2.1	Passive disturbance reduction	9
2.2.2	Active disturbance reduction principles	16
2.2.3	Hybrid disturbance reduction principles	18
2.3	Disturbance rejection during launch	18
2.4	Disturbance reduction during orbit and operation	21
2.4.1	Strategies	23
2.5	Multi-DOF Stages	29

This chapter explores the developments in isolation systems onboard a spacecraft. A brief introduction to the strategies used to achieve a reduction in the transmitted vibrations is followed by an overview of both flight-tested systems and systems in their conceptual design stages. These can be subdivided into two categories: whole spacecraft isolation systems, where the goal is to protect a whole spacecraft from the mechanical disturbances of the launch environment, and component-specific isolation systems. Component-level systems can be further subdivided into two types according to their purpose: launch load protection and operational load protection.

2.1 Motivation

Every payload delivered to orbit is subjected to a harsh launch environment with high-magnitude disturbances and shocks. The high loads seen during launch can cause issues in the spacecraft ranging from optical misalignment, and payload malfunction, to complete spacecraft failure. This environment creates the need to overbuild the payloads in order to ensure their survival, adding mass and complexity to the system.

Likewise, once a satellite is in orbit, mechanical disturbances with amplitude of micro or milli-g propagating onboard spacecraft can be very detrimental to the accomplishment of their missions. These disturbances can compromise the fine pointing required in high-resolution imaging telescopes employed for Earth remote sensing [11], astronomical observations [9], or inter-satellite laser communications [12]. Such micro-vibrations can also increase the noise levels of particularly sensitive instruments rendering their measurements useless, as is the case of high-precision accelerometers used in gravimetric missions [13], optical interferometers [14], or reference oscillators [15].

2.2 Disturbance reduction principles

Multiple techniques can be used to reduce the magnitude of vibrations being transmitted through a complex structure such as a spacecraft. These techniques can be split into two main categories, passive and active strategies. Passive strategies benefit from being simple to implement, lower cost solutions with respect to active strategies. However, they are limited in terms of the performance they can deliver.

The objective of this section is to introduce some basic principles, which have been useful to understand for the development of the research projects explained in this thesis.

2.2.1 Passive disturbance reduction

A widespread approach to mitigate the propagation of disturbances onboard a spacecraft is to use passive means. This entails the use of components that rely on their physical properties in order to affect the magnitude of the disturbances passing through them. Thus avoiding the need for an external power supply.

In order to explore this subject let's take the one degree-of-freedom system shown in Fig. 2.1 as an example. The equations of motion in the time domain of such a

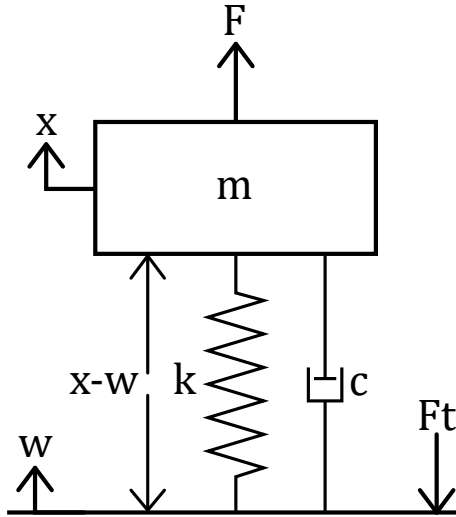


Figure 2.1: 1 degree-of-freedom mass-spring-dashpot system of mass m , stiffness k and damping c

system are

$$\begin{aligned} m\ddot{x} + c(\dot{x} - \dot{w}) + k(x - w) &= F \\ F_t &= -c(\dot{x} - \dot{w}) - k(x - w) \end{aligned} \quad (2.1)$$

where m is the suspended mass, whose displacement is represented by x upon which a force F is acting. The damping and stiffness are c and k respectively, and w is the ground motion. F_t is the force transmitted to the base. These equations can be stated in the frequency domain by taking the Laplace transform resulting in

$$\begin{aligned} ms^2X + cs(X - W) + k(X - W) &= F \\ F_t &= -cs(X - W) - k(X - W) \end{aligned} \quad (2.2)$$

From the above equation, the motion and force transmissibilities (the ratio of the forces is also called isolation factor) and the compliance transfer functions can be obtained to evaluate the performance of this system as a disturbance rejection stage.

$$\begin{aligned} T_{WX} &= \frac{X}{W} = \frac{cs + k}{ms^2 + cs + k} \\ T_{FFt} &= \frac{F_t}{F} = -\frac{cs + k}{ms^2 + cs + k} = -\frac{X}{W} \end{aligned} \quad (2.3)$$

$$T_{FX} = \frac{X}{F} = \frac{1}{ms^2 + cs + k} \quad (2.4)$$

Plotting the above transfer functions for a system with the values in Table 2.1 results in the plots found in Fig. 2.2. These plots are discussed further in the

subsections which follow.

Table 2.1: *Numeric values used to evaluate the one-dof system shown in Fig. 2.1*

Parameter	\mathbf{m} [kg]	\mathbf{k} [N/m]	ξ	$\mathbf{c} = 2\xi\sqrt{km}$ [N/(m/s)]
Value	1	1000	0.1	6.325

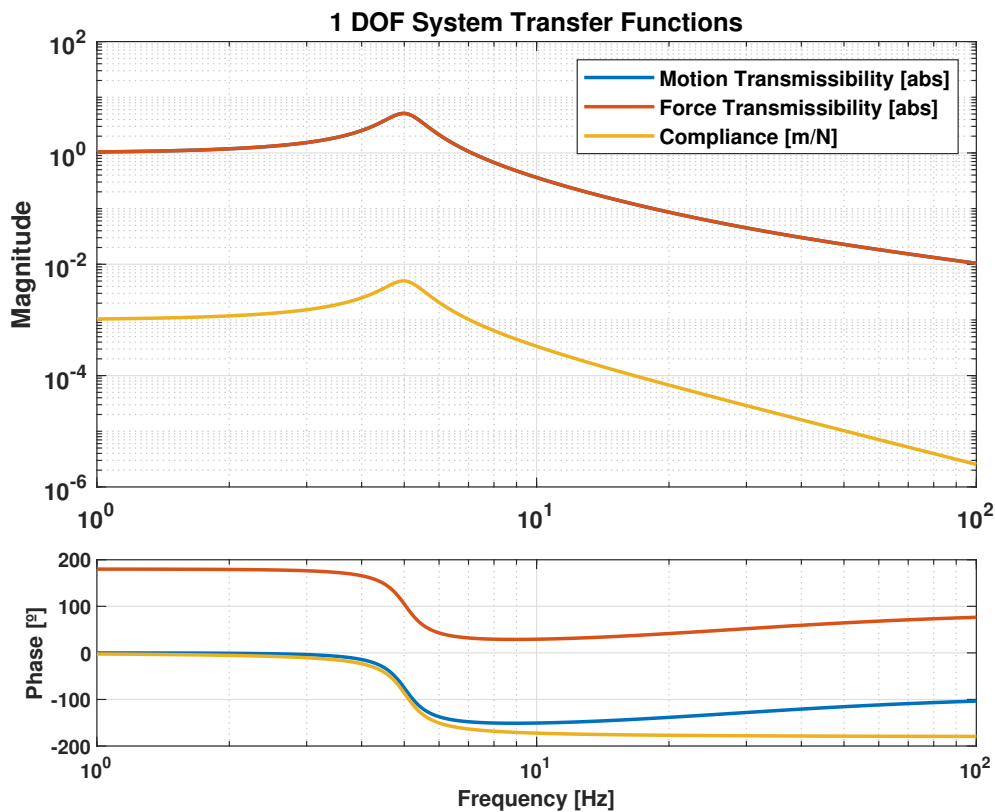


Figure 2.2: *Motion and Force transmissibilities and Compliance transfer function. Note the equal magnitude of the transmissibilities with the negative sign represented by the 180° phase shift*

In the transmissibility, at frequencies below the resonance the mass follows the base motion, resulting in no deflection of the suspension ie. $(x - w) = 0$. At the resonance frequency of the system $\omega_n = \sqrt{\frac{k}{m}}$, the motion of the suspended mass is amplified by the dynamics of the system, only limited by the damping, resulting in a motion ratio higher than 1. Passive isolation occurs in the frequency bandwidth above the resonance of the system, in the roll-off part of the transfer function, at a frequency $\omega = \sqrt{2}\omega_n$ where the magnitude drops below 1. After this point, in undamped systems, the curve has a slope of -40 dB/decade.

Disturbance reduction principles

The frequency at which isolation starts, and therefore the magnitude of the maximum achievable isolation for such a system is a function of its resonance frequency. It would therefore seem optimal to select the resonance frequency as low as possible in order to maximize the isolation provided by a system. The effect that varying the resonance frequency of a system has on the transmissibility is shown in Fig. 2.3. The resonance frequency of a system is proportional to the square root of the stiffness, and inversely proportional to the square root of the suspended mass. The compliance represents the ratio of motion of the suspended mass for a given input force. Fig. 2.4 shows the effect that changing the resonance frequency of a system has on the compliance. As can be observed, if the resonance frequency is reduced by decreasing the stiffness, the compliance below the resonance increases, resulting in a larger motion of the mass in that bandwidth for a given input force. An equilibrium needs to be found between the desirable isolation and the maximum permissible motion of the system when designing a passive isolation system.

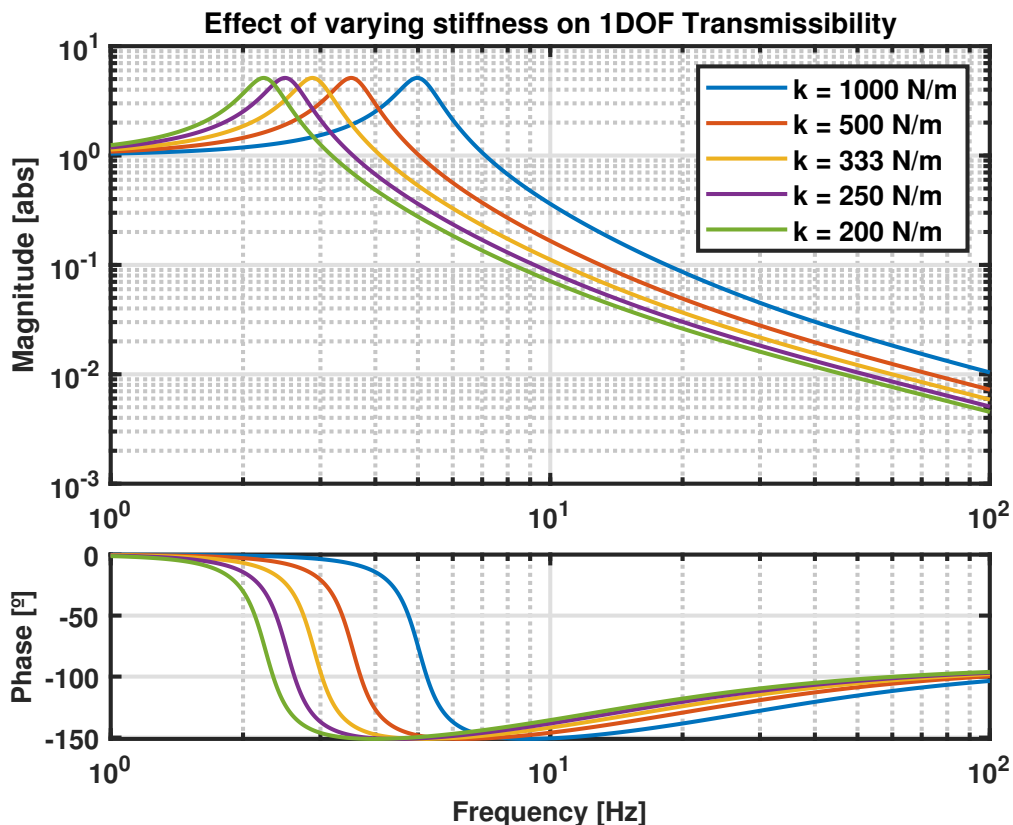


Figure 2.3: Effect on the transmissibility of reducing the stiffness by up to a factor 5. Note how the magnitude at 100 Hz decreases with each successive reduction in stiffness, improving the isolation of the system

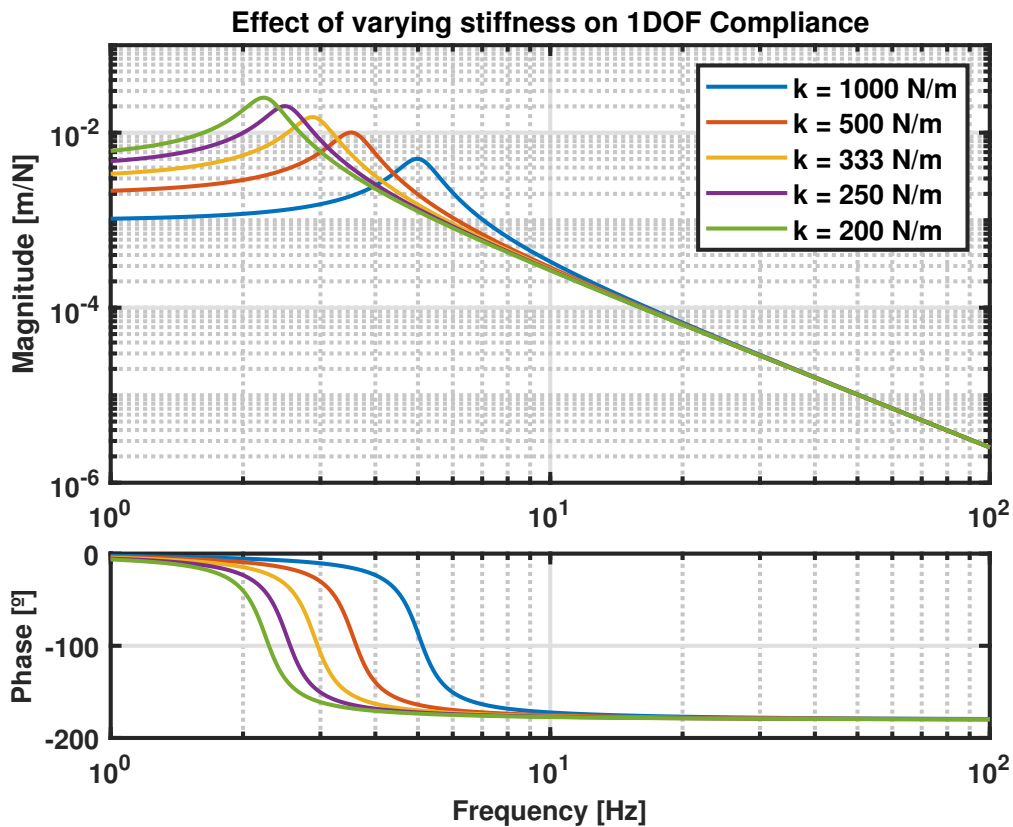


Figure 2.4: *Effect on the compliance of reducing the stiffness by up to a factor 5. Note how the magnitude at DC increases with each successive reduction in stiffness, degrading the resistance to motion for a given input force*

Passive isolators can be found in everyday objects which take advantage of this natural isolating property of dynamic systems. Car suspensions can be tuned to take advantage of this phenomenon, where the stiffness of the springs connecting the chassis to the tyres is tuned to provide comfort to the occupants by having a low resonance frequency and thus filtering out the ground imperfections [16]. Similarly, the drums in washing machines are also suspended by springs as seen in Fig. 2.5, in order to reduce the noise and force transmission of the washing machine when it enters operation.

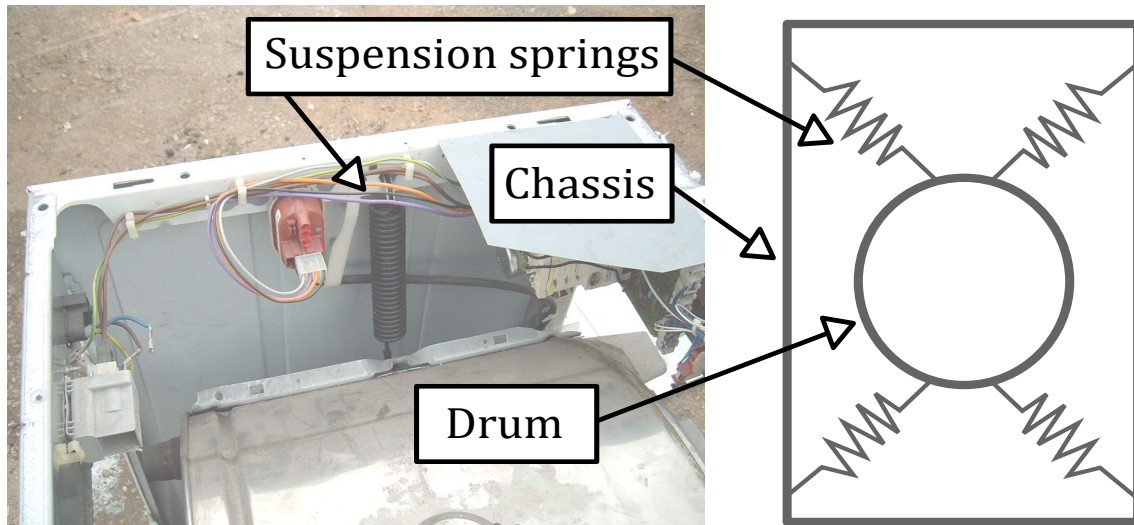


Figure 2.5: *Picture of the inside of a washing machine with diagram for illustrative purposes. Note the suspension spring connecting the drum and the chassis for vibration isolation purposes*

As seen previously, damping mainly plays a role in the magnitude of the motion of a system at its resonance. However, by appearing as a frequency dependent term in the numerator of the transmissibility in Eq. 2.3, it also has a negative impact on the dynamics of the system at high frequency. Figure 2.6 shows the effect of varying the damping for the system pictured in Fig. 2.1. As the damping increases, the magnification at resonance is successfully contained, however, this is done at the expense of a degradation of the roll-off, and therefore the isolation of the system.

This is the natural trade-off between isolation and damping, which can only be circumvented by the use of active control as will be shown in the following section.

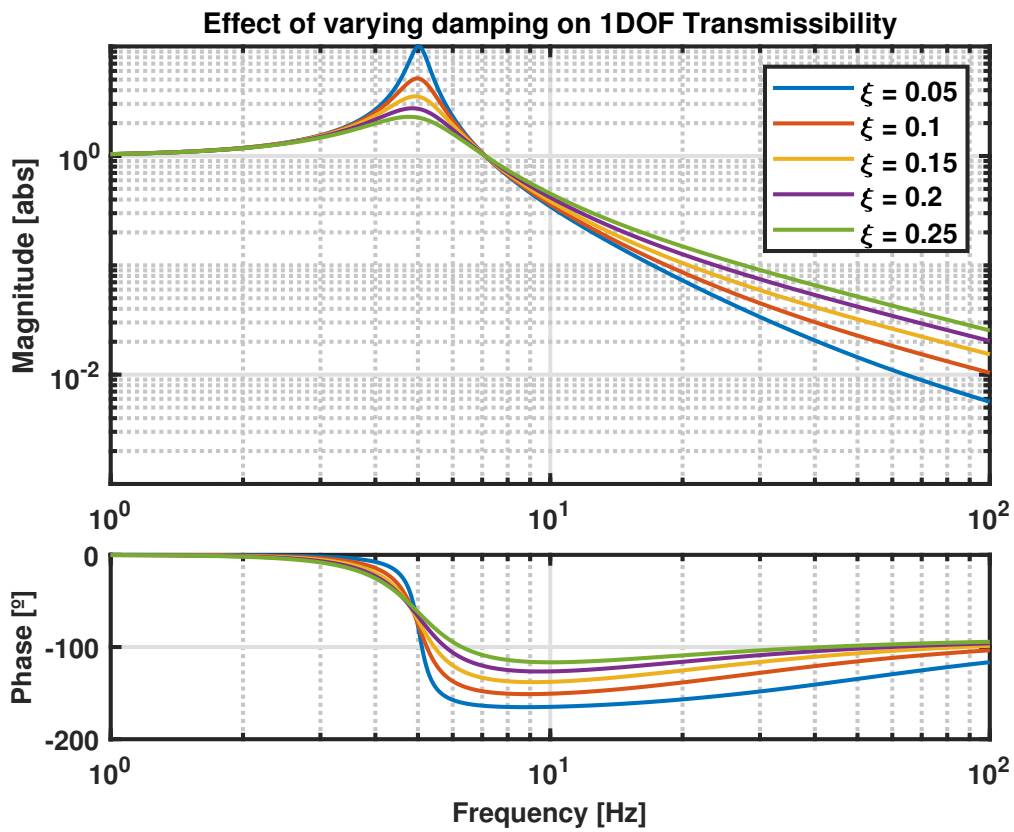


Figure 2.6: *Effect on the transmissibility of increasing the damping. Note how increasing the damping decreases the magnitude at resonance, but increases the magnitude at high frequency*

2.2.2 Active disturbance reduction principles

Active disturbance rejection refers to the use of an external energy source combined with a means of acting on the system in order to achieve a reduction of the motion. The transfer function used to shape the signal introduced by the actuator is the controller. When performing feedback control, the signal from a sensor is used as input to the controller.

Depending on the typology of the sensors, actuators, and controllers used, different goals can be achieved. The two types of sensors used in disturbance reduction are motion sensors, capable of measuring displacement, velocity, or acceleration, and force sensors. As previously shown in Section 2.2.1, varying different parameters in the equation of motion can affect both the transmissibility and the compliance transfer functions. By selecting an appropriate combination of sensors, actuators, and control strategy, different parameters can be targeted in order to achieve the desired performance. The relationship between the desired goals and the control architecture is presented in this subsection.

The most straightforward way to increase the isolation of a system is to reduce its resonance frequency. This can be done by acting on the stiffness and mass terms of the equation of motion, which translates into injecting a force proportional to the displacement or acceleration of a system [17]. These magnitudes can be recovered from an absolute motion sensor on the mass or a relative motion sensor placed between the mass and its base.

However, the aforementioned strategies have a non-negligible impact on the compliance of the system which needs to be taken into account when assessing their performance. There therefore exists an optimization problem between the amount of isolation needed and the amount of deformation allowed in a system.

Dissipating energy from the system will invariably introduce damping into it. An approach to this is to apply a modifier to the velocity term in the equation of motion of a system. This approach can be called velocity feedback. The modifier can be applied to the absolute velocity of the system \dot{x} , or to the relative velocity $\dot{x} - \dot{w}$. The set in Eq.(2.5) represents the force resulting from the absolute or relative velocity of the system, where H is the controller applied.

$$\begin{aligned} f_{abs} &= -H(\dot{x}) \\ f_{rel} &= -H(\dot{x} - \dot{w}) \end{aligned} \tag{2.5}$$

Applying active control to the system in Fig. 2.1 results in the following set of equations of motion:

$$\begin{aligned}
 &ms^2X + cs(X - W) + k(X - W) = F + f_{abs} \longrightarrow \\
 &\rightarrow ms^2X + cs(X - W) + k(X - W) = F - H(s)sX
 \end{aligned} \tag{2.6}$$

$$\begin{aligned}
 &ms^2X + cs(X - W) + k(X - W) = F + f_{rel} \longrightarrow \\
 &\rightarrow ms^2X + cs(X - W) + k(X - W) = F - H(s)s(X - W)
 \end{aligned}$$

Solving to obtain the corresponding motion transmissibilities results in

$$T_{abs} = \frac{k + cs}{ms^2 + cs + k + H(s)s} \tag{2.7}$$

$$T_{rel} = \frac{k + cs + H(s)}{ms^2 + cs + k + H(s)s} \tag{2.8}$$

By analyzing the numerators of Eq's (2.7, 2.8) an interesting property of performing absolute motion control comes to light. While performing relative motion control has a similar impact on the motion transmissibility as passively adding damping to a system, this is not the case for absolute motion control. Increasing the damping of the system through this method does not affect the roll-off of the motion transmissibility.

However, adding damping to a system through relative motion control still retains a main advantage over passively adding damping. Through active control, there is authority over the frequency bandwidth on which the damping is applied. By actively applying damping in the frequencies around the resonance instead of over the whole spectrum, the overall damping introduced into the system is limited, and the degradation of the roll-off at higher frequencies and hence the impact on the isolation is reduced.

The alternative to motion sensing is force sensing. A typical example is Integral Force Feedback (IFF) where the input to the actuator is the integrated signal of the measured force. Since the measured force is proportional to the acceleration of the system, the integrated signal results in a value proportional to the velocity, and therefore contributes to adding damping to the system [18]. Improved performances can be achieved by using advanced controllers as proposed in [19] which further improve the performance of the system at low frequency while reducing its impact on the compliance.

2.2.3 Hybrid disturbance reduction principles

In hybrid vibration isolation systems, different mechanisms are often employed in combination to achieve better vibration attenuation across a broader frequency range or to address specific challenges. Active vibration isolation systems often require continuous power to operate sensors, actuators, and control systems. In contrast, hybrid systems can utilize passive elements to handle lower frequency vibrations, reducing the overall power consumption. This can be particularly advantageous in applications where power efficiency is a concern, such as portable devices, and remote installations, or in scenarios where the overall size and weight of the package is a concern. Passive elements in hybrid systems contribute to overall robustness and reliability. Passive damping mechanisms are inherently simpler and less prone to failure compared to active components, which rely on complex electronic and mechanical systems. The combination of passive and active elements can enhance system resilience and ensure continued operation even in the event of component failure, achieving a fail-safe condition through ensuring a minimum level of performance retention in case of failure of the active part [20].

2.3 Disturbance rejection during launch

The goal of disturbance rejection during launch is to protect sensitive equipment from the dynamic loads seen during take-off and up to separation of the spacecraft from the launch vehicle.

Current vibration isolation systems are aimed at isolating vibrations in a spacecraft environment [21]. To do so in a reliable and light manner, passive isolators are used. When compared to active solutions, these types of isolators are cheaper to manufacture and install, and more lightweight, thereby enabling the haul of heavier cargo, and they are fail-safe. The simplicity and scalability of these systems enable their widespread use. There are no power supplies, sensors, or actuators that could fail and no control loop that could become unstable.

An example of a flight-proven passive isolator is the CSA-Uniflex [22], which reduces the propagation of vibrations in the axial direction through a spacecraft. The system consists of a set of damped flexible elements composed of a steel frame with an inner lining of viscoelastic material. Placed at the interface between the launcher and the spacecraft, just above the separation point, the array of flexures damp vibrations mainly in the vertical direction due to their lower stiffness in comparison with the horizontal direction. Via this construction (Fig. 2.7), the system achieves

vibration isolation at high frequencies. However, low frequency vibrations (<20 Hz) are not completely damped, and are even accentuated at some points during the flight. Another solution can be found in [3], similar in construction to the previous one, but capable of absorbing launch loads in both the axial and in-plane directions. When including such systems into the architecture, a magnification of the response at the natural frequency of the system with the isolators can be observed, as shown in Fig. 2.8.

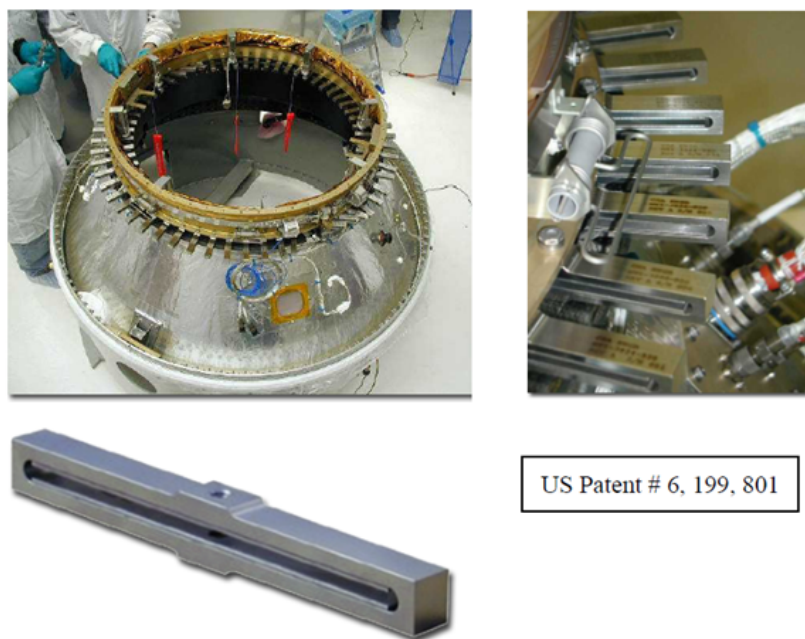


Figure 2.7: *Installation of a whole-spacecraft vibration isolation system [2]*

Regarding active solutions, [4] presents an active hexapod in a Stewart-Gough platform configuration. This hexapod's parameters are tuned to have a resonance frequency of 0.4 Hz. A test setup with a detailed view of the actuator is presented in Fig. 2.9. A capacitive displacement sensor in series with a voice coil is used in each leg for active control. The low natural frequency of the hexapod allows for high isolation at frequencies past the resonance, and through active control, the amplification at the resonance is successfully reduced. However, in the roll-off of the transfer function, sudden peaks appear, degrading the isolation performance of the isolator. This is a common drawback of platforms with this design, where local flexibilities along the struts give rise to resonant modes reducing the effectiveness of this solution.

An approach similar in philosophy to the Soft-ride presented above, but combined with active control is introduced in [5]. In this case, curved beams are used for structural support and tuning of the resonance frequency, at the interface between

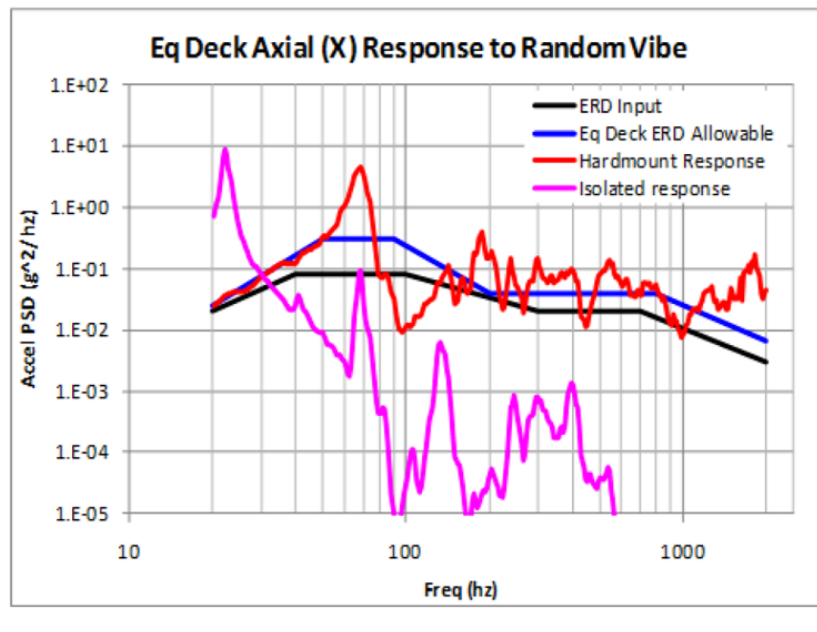


Figure 2.8: Comparison of the measured responses of an instrument without isolation at the interface (red curve) and with isolation at the interface (pink curve) [3]

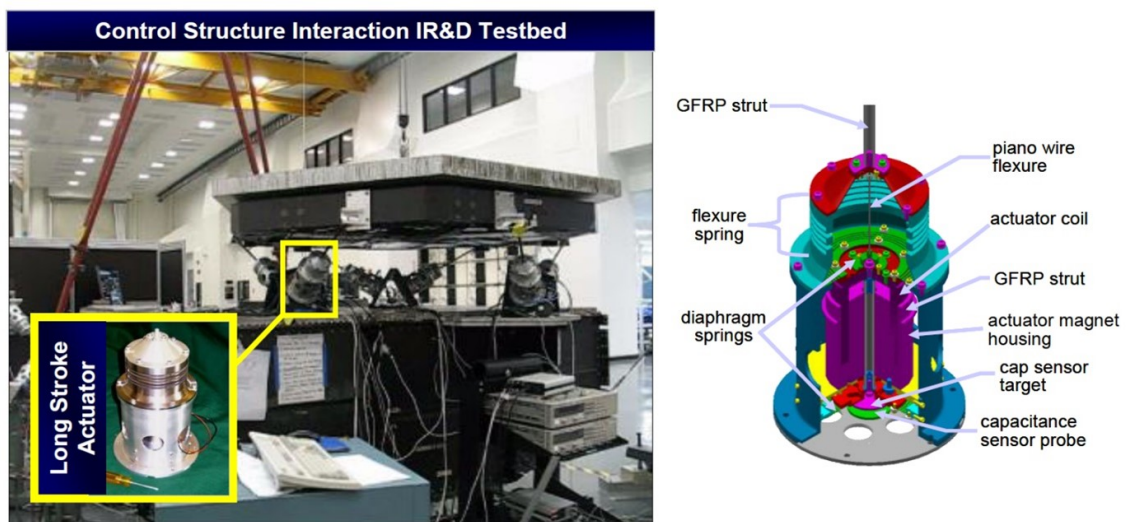


Figure 2.9: Control Structure Interaction (CSI) Testbed, where optical payload simulator is mounted onto the spacecraft using a passive/active hexapod isolator comprised of six long-stroke actuators [4]

the launcher and the satellite. The voice coils installed inside the payload adapter are used to improve the performance with active control. This solution is presented in Fig. 2.10.

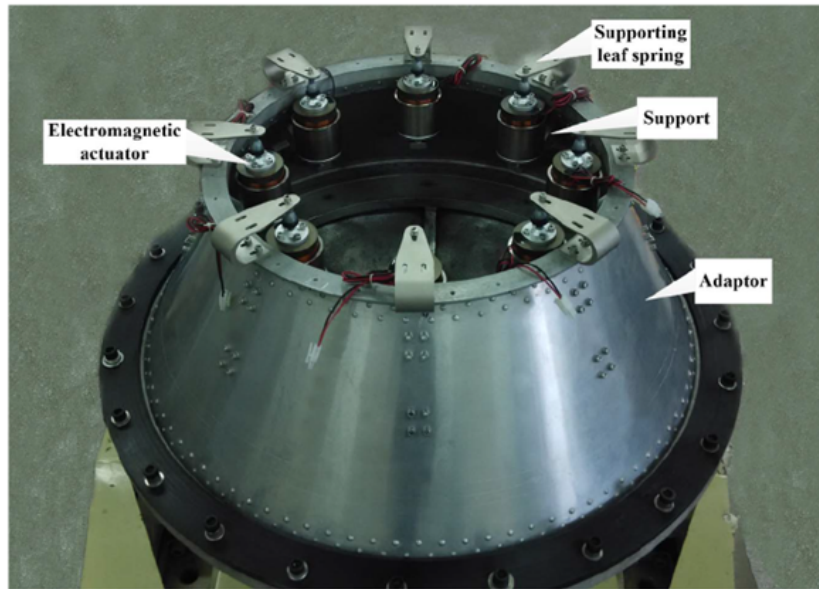


Figure 2.10: *Prototype of a whole spacecraft active isolation system using curved beams and voice coils [5]*

Other solutions worth noting are: a passive platform with 8 legs which provides fail-safe advantages, retaining performances in the event of failure of up to two of its legs [23], a light-weight composite payload adapter ring with similar performances as the Soft-ride approach [24], the placement of tuned mass dampers on different locations of the spacecraft in order to reduce local modes [4], and a conical adapter with bonded piezoelectric patches to act as sensors and actuators [25].

2.4 Disturbance reduction during orbit and operation

Once the launch vehicle reaches the spacecraft's injection orbit, the separation is triggered. This is the last dynamic event related to launch and marks the start of orbit operation for the spacecraft. After the necessary Launch and Early Orbit Phase activities are completed, the spacecraft is put into nominal mode and its onboard systems become operational. Once this state is achieved, the sensitive payloads onboard the spacecraft need to be protected from the mechanical disturbances introduced by the different components required to operate and maintain

the spacecraft.

The main sources of micro-vibrations onboard satellites consist of mechanisms such as cryocoolers, mirror and antenna pointing mechanisms, solar array drive mechanisms, and reaction wheels. In particular, reaction wheels are a prevalent actuator for the attitude control of satellites, which operate by repeatedly transferring angular momentum to and from a flywheel to the spacecraft. To enable attitude change maneuvers with the required agility, the flywheels used have considerable inertia and can operate continuously at high spin rates. Therefore, minor unbalances of their inertia properties and imperfections in the bearings used for flywheel suspension and their internal components originate disturbance forces and moments. These disturbances are broadband, mainly occurring at the spinning rate of the reaction wheel and its harmonics, and propagate through the spacecraft structure being amplified by their lightly damped resonances, finally reaching sensitive instruments with sufficient amplitude to affect their operation. Often, reaction wheels are the largest pointing and vibration disturbance in spacecraft.

The management of the micro-vibration problem needs to take place at the system level, including the definition of performance budgets, and the implementation of engineering methods that encompass simulation, testing, and definition and verification of overall micro-vibration levels and interface requirements [26–28]. The process for minimizing the micro-vibration disturbances then involves design and operational aspects. On the design side, sources and receivers should be accommodated within the satellite far away from each other, if allowed by their function. The introduction of damping systems or isolation layers can be considered together with a trade-off to be performed between sources and receivers. The overlap of frequencies shall be avoided between excitation sources, structural resonant modes, and susceptibilities of receivers. Moreover, this frequency control must be extended to the operational concepts, by scheduling the operation of mechanisms in a way that minimizes the impact of their disturbances. In the case of reaction wheels, this translates into constraining their usable speed range and establishing specific pointing control strategies.

Dennehy and Alvarez-Salazar [29] have presented an extensive review of challenges, lessons learned, and potential solutions regarding spacecraft micro-vibrations. The severity of the micro-vibration problem is ranked in terms of the pointing stability requirements of a mission, and different design solutions are recommended. For instance, reaction wheel isolation platforms are typically necessary for missions with pointing stability in the range between 10 and 0.1 arcsec, which correspond, eg. to the Chandra X-Ray, and the European Space Agency - European Organisation for the Exploitation of Meteorological Satellites Meteosat Third Generation (ESA-

EUMETSAT MTG) with its infrared and ultraviolet imagers and sounders [30]. Dual-stage passive isolation is recommended when pointing stability in the order of 0.01 arcsecs is required, eg. SIRTF. Missions requiring extreme stability resort to micro thrusters to actuate their attitude control systems instead of reaction wheels [31]. Such micro thrusters produce very limited mechanical disturbances and operate by ejecting cold gas, or by accelerating tiny charged droplets, metallic ions, or plasma by means of an electrical field. Micro thrusters become essential for pointing stability better than 0.01 arcsec, such as in the case of GAIA, the currently under development Nancy Grace Roman Space Telescope, and the more ambitious HABEX and LUVOIR.

The drawback of employing micro thrusters is that they significantly constrain the design of the spacecraft with a distributed infrastructure, including tubing, reservoirs, and the thrusters themselves. Moreover, the consumable propellant limits the operational lifetime of the spacecraft. Therefore, a strong interest remains to push the envelope of applicability of reaction wheels, and thereby improve the performance of vibration isolation systems capable of filtering the disturbances they create.

2.4.1 Strategies

There are three main approaches when it comes to reducing the magnitude of the disturbances reaching sensitive payloads:

- **Targeting the source** - modifications are implemented in the disturbance-generating apparatus in order to reduce the overall magnitude of the disturbances injected into the spacecraft
- **Targeting the interface** - instead of rigidly mounting the disturbance source or the sensitive equipment to the spacecraft, specialized mounts can be used which reduce the magnitude of the disturbances passing through them
- **Targeting the transmission path** - in cases where the sensitive equipment can be concentrated in one area of the spacecraft, vibration isolation measures can be placed between the different disturbance sources and the sensitive equipment

Targeting the source

The ideal solution to reduce the impact of disturbances is to not create them in the first place. There is a downward trend in the magnitude of the disturbances generated

by spacecraft components, however, due to the physical nature of the operation of these components, it is not feasible to completely eradicate the disturbances they create. Pointing mechanisms for solar panels and antennae inject vibrations into the spacecraft when moving. Reaction wheels and CMGs (control moment gyroscopes) create broad-band mechanical disturbances when spinning. Cryo-coolers give rise to narrow-band excitations when they engage their reciprocating action.

Improvements in bearing technology, as proposed in [32], where magnetic or even air bearings powered by small piezoelectric pumps succeed in significantly reducing the amplitude of the higher-order harmonics of the reaction wheel. When these harmonics cross frequencies with structural resonances of the reaction wheel they are amplified, injecting disturbances into the system. Reducing their amplitude, resulted in a reduction of the generated vibrations by up to a factor of 100. Another example of micro-vibration suppression at the source are cryocoolers. These systems reciprocate at a fixed speed, producing disturbances at frequencies related to their speed and their harmonics. Since the early 1990s active control means have been included in their electronics to curb the resulting vibrations they emit [33].

Targeting the interface

The main way to provide component-level vibration mitigation is by modifying the interface between the generating source or the sensitive payload and the spacecraft. This can be done by placing an isolator directly between the source and the spacecraft, by placing the isolator between the spacecraft and the precision payload, or by doing both. Similar to the payload comfort case, both active and passive solutions exist, sharing the advantages and disadvantages discussed in the previous section.

The extreme pointing stability required by the Hubble Space Telescope demanded that the disturbances generated by its reaction wheels be mitigated by supporting them on isolation mounts. Each of the three mounts consists of a pair of dampers involving springs and viscous fluid and are mounted parallel to the axis of spinning of the wheels [6, 7]. This architecture is shown in Fig. 2.11.

Alternatively, isolation suspensions can be implemented by means of elastomeric mounts, which have a simpler design and preserve better the high frequency isolation than viscous fluid dampers. Carte [8, 34] describes such a concept developed for isolating the disturbances of the reaction wheels of the MTG satellites, which rely on three elastomeric mounts tuned in stiffness, damping, and position with relation to the centre of gravity of the reaction wheel. These were qualified and embarked for flight and the reported axial transmissibility consists of -40dB of isolation at 200 Hz,

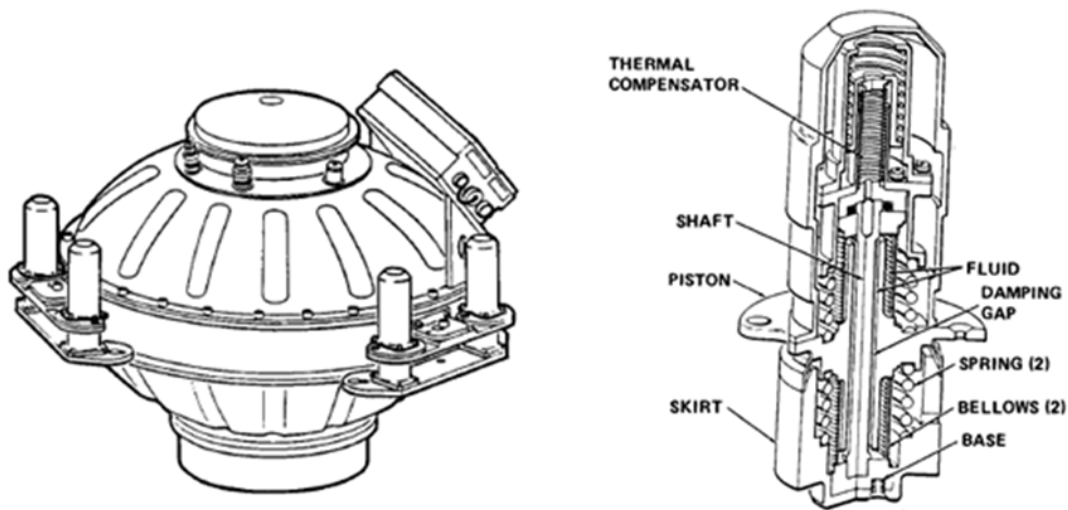


Figure 2.11: Full isolation system with reaction wheel [6] (left) and isolator spring-damper element cutaway (right) [7].

but come at the cost of an amplification of 20dB at the resonance frequency of 15 Hz of the suspension mode. This architecture is shown in Fig. 2.12.

As an alternative to the elastomeric mounts, a suspension formed by washers made of a shape memory alloy metallic mesh has been proposed by Kwon et al [35]. Results are reported for a micro-vibration test on a shaker, putting in evidence a highly damped suspension mode at 20 Hz. A less steep roll-off results in an isolation of -27dB at 200 Hz and about -47dB at 800 Hz, which is nonetheless very broadband, before the isolation is lost due to secondary resonances.

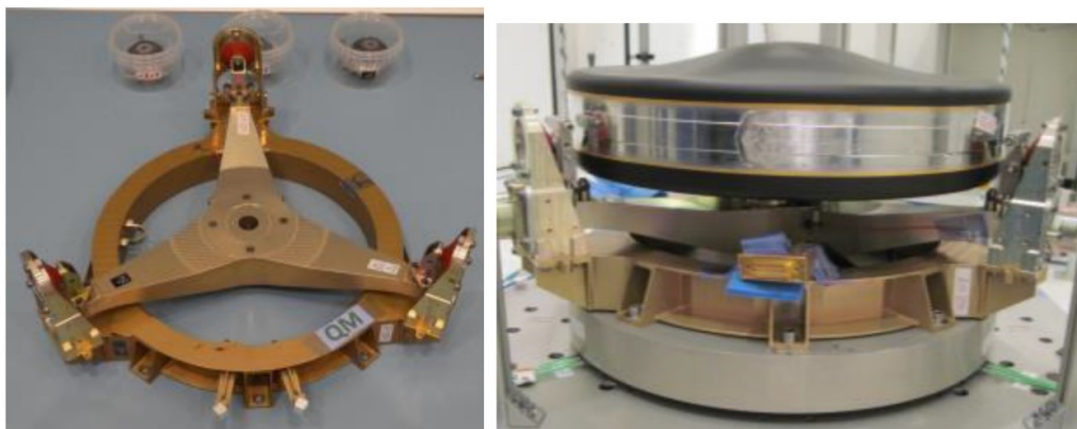


Figure 2.12: Thales Alenia Space Reaction Wheel Isolator (left) fitted with a Rockwell Collins Deutschland reaction wheel (right) [8]

Interesting concepts of suspensions based on flexures with elaborate geometries have also been proposed and analyzed, one fully three-dimensional by Kamesh et

al. [36] while Wei [37] proposes an in-plane two-dimensional flexure and predicts by analysis its performances in isolating the radial disturbances generated by a reaction wheel.

Isolation platforms in the form of a hexapod, allow independent authority over all six degrees of freedom. In the concept of the Stewart platform [38] two plates corresponding to the noisy and quiet sides are interconnected by six struts forming the edges of a cube and therefore orthogonally connected. This results in a compact configuration that minimizes the interaction between the struts and allows for applying an identical design for the six struts and a decentralized control in the case of active suspensions. Several concepts of isolating hexapod platforms have been proposed, both passive [39–41] as well as active [42–46].

A passive hexapod isolation platform, shown in Fig. 2.13, has been successfully flown in the NASA Chandra X-Ray Space Telescope [39]. The suspension is implemented by means of titanium slotted springs, bonded with viscoelastic material.

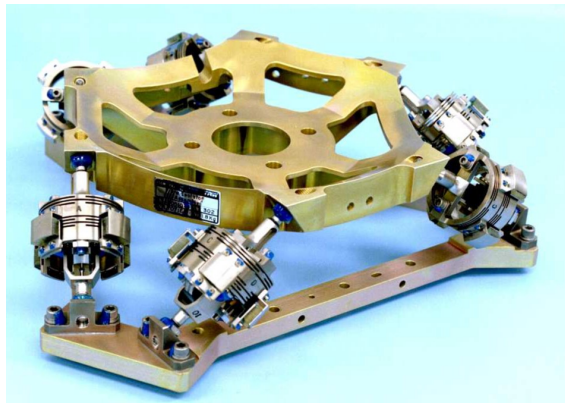


Figure 2.13: *Reaction wheel isolation assembly, with the spring elements mated to the cradle and bottom bracket*

Transmissibilities were published for the three translational directions, showing a suspension mode at 10 Hz with an amplification of 20 dB, followed by a roll-off with a maximum experimental isolation of -18dB at 100 Hz which is then lost at increasing frequencies due to the presence of secondary resonances [47].

This same design of isolation platform was then installed on board the James Webb Space Telescope [9]. However, in this mission, micro-vibrations are further reduced by installing a second layer of isolation, i.e. by supporting the Optical Telescope Element on a very flexible truss bonded with visco-elastic material.

More complex designs for the hexapod struts have evolved in the meanwhile. Honeywell further developed the fully passive D-strut viscous dampers operating on the Hubble Space Telescope [7], by adding voice coils moving in the direction

of active and hybrid concepts. Davis [43] reports the uni-axial testing of such a second-generation D-strut, in which an actively controlled strut exhibits a suspension mode at 15 Hz, with negligible amplification, followed by a sustained -20 dB isolation between 20 Hz and 200 Hz which improves to -60dB at 800 Hz.

A similar active concept is described by Lee in [48], further implementing force sensors. The performance of a full hexapod platform was experimentally characterized with the operation of a reaction wheel. The system exhibits suspension modes at 10 Hz and an isolation of -40dB is achieved at 100 Hz.

Furthermore, novel concepts of active struts have emerged more recently, in which the dampers with viscous fluids have been replaced by dampers based on electromagnetic shunting (via voice coils) with negative resistance synthesized with electrical circuits [45, 46]. Test results are reported for a hexapod with suspension modes at 2-3 Hz. The introduction of multiple flexible elements in series with masses, results in a two-degree-of-freedom system with a roll-off of the transmissibility of -80 dB / decade landing on an isolation of -60 dB at 100 Hz. However, due to the presence of secondary resonances, in particular bending modes of the struts, the isolation reverts to -20dB at 200 Hz and remains compromised above those frequencies.

It becomes clear from studying the available literature that the performance of a given isolation system is dependent on the characteristics of the roll-off of the transmissibility after the system's resonance. The main factors affecting this roll-off are: its starting point, given by the resonance frequency of the system, its slope, dependent on the damping of the system where lower damping results in a steeper slope, and the appearance of secondary resonances rising from local deformation modes in the transmission path of the disturbances. To maximize the isolation performance of a system it is therefore important for it to have a low resonance frequency, low damping, and no secondary resonances in the frequency band of interest for the isolation. However, a low value of damping required to preserve the high-frequency isolation results in a high amplification of the disturbances occurring at the resonance frequency of the isolator. To tackle this issue, active control, in the form of relative velocity feedback, is applied at frequencies around the suspension resonance.

The objective in the development of the active platform presented in this thesis is to improve the isolation performances with relation to those published in the literature available and presented above in the review of the state of the art, whilst maintaining a simple enough configuration to make the isolator attractive to be embarked on a satellite. The active platform presents a high isolation factor due to

Disturbance reduction during orbit and operation

its low resonance frequency and absence of local deformation modes up to 500 Hz, achieving 60 dB of reduction in the transmitted forces at 130 Hz, with a maximum recorded reduction of 65 dB at 270 Hz. Active control is used to damp the main suspension modes, reducing the amplification at their corresponding frequencies.

Targeting the transmission Path

In cases where the sensitive instruments can be localized in the spacecraft away from all the noise-generating equipment, it is possible to implement measures of vibration mitigation in the spacecraft's structure.

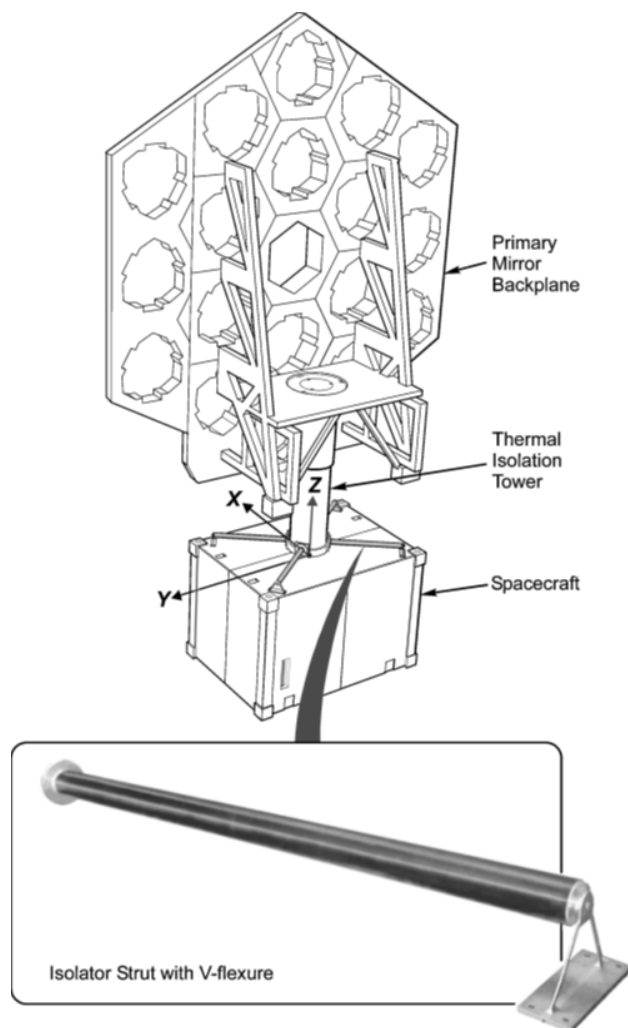


Figure 2.14: *Spacecraft bus, isolator strut assembly, tower and primary mirror backplane [9]*

In the previously mentioned JWST, the sensitive instruments in charge of capturing the light have been placed at one end of the spacecraft, opposite to the bus housing most of the operational equipment like reaction wheels. The architecture is

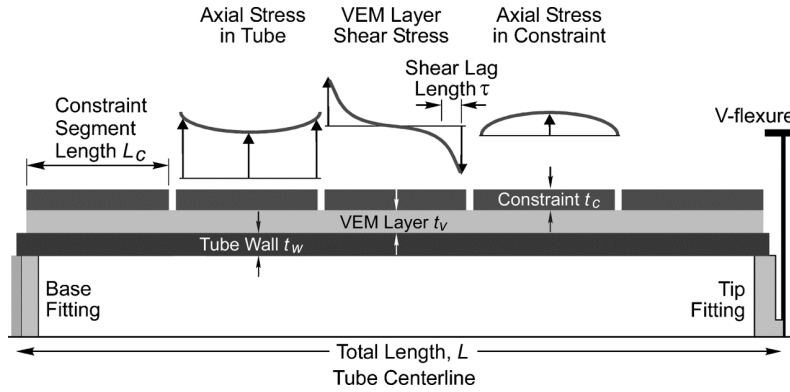


Figure 2.15: *Details of the isolator strut assembly [9]*

shown in Fig. 2.14. The path connecting the spacecraft and the telescope is made of four composite beams of graphite/epoxy with embedded viscoelastic damping layers mounted on V brackets. A detailed view of the strut assembly is presented in Fig. 2.15. The damping properties of the struts are controlled by varying the temperature in the struts through heating elements. With this configuration, a reduction of 40 dB has been experimentally achieved [9].

An efficient, lightweight way of supporting large structures is to use trusses. These structures are typically used in spacecraft to connect the main bus to its instrument, be it an antenna or an Earth observation payload. Due to their stiff, lightweight nature, they present a high Q-factor, resulting in high vibration transmission from satellite bus to payload. To mitigate this effect, researchers in [49] employed collocated piezoelectric actuator and force sensor pairs in a truss system representative of the SPOT 4 HRV (High Resolution Visible) Earth Observation satellite. With this architecture, a reduction of peak accelerations exceeding 25 dB was achieved in the 40 to 160 Hz range.

2.5 Multi-DOF Stages

When disturbance rejection is required in more than one DOF, multi-DOF stages can be used. By combining filtering elements, be it springs, dampers, actuators, or any combination of the above at the interface between two surfaces, it is possible to gain authority over more than one direction. A six-DOF platform was developed by Gough [50] as a tyre testing machine. The concept was evolved by Stewart in [38] into an independently driveable platform to be used as a flight simulator for pilot training exercises. As seen from the examples presented previously in this chapter, the control authority that such platforms provide over the six degrees of freedom

can be exploited for disturbance rejection applications.

The transmissibility of a multi-DOF stage can be extracted in the different directions from its dynamic response. Consider the rigid platform mounted on six active mounts shown in Fig. 2.16 (only four mounts are shown). Each mount consists of a spring in parallel with an actuator.

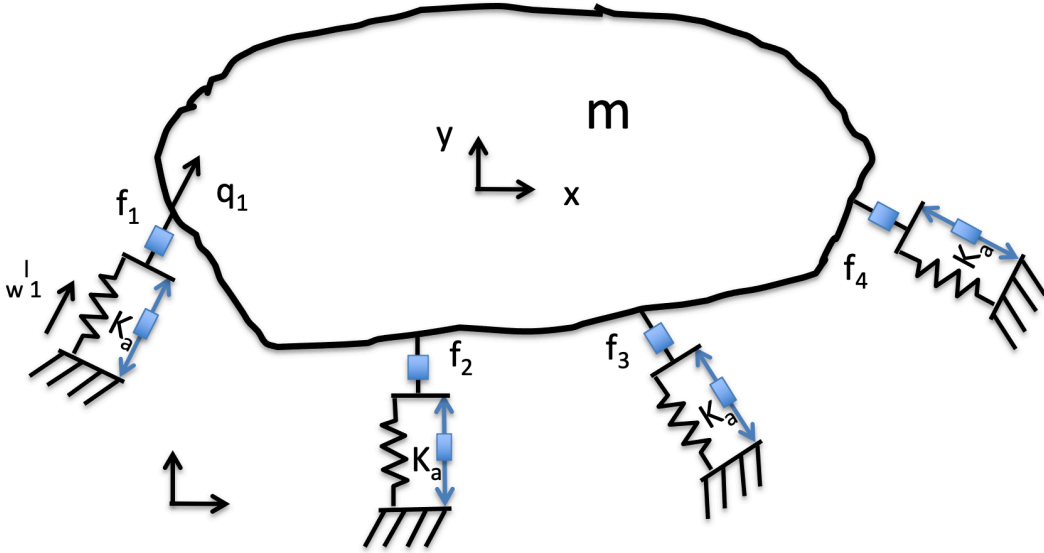


Figure 2.16: A multi-supported platform

The dynamics of the platform are governed by

$$M\ddot{\mathbf{x}} = \mathbf{F} \quad (2.9)$$

where $M = \text{diag}(m, m, m, I_\theta, I_\phi, I_\psi)$ is the mass matrix, $\mathbf{x} = (x, y, z, \theta, \phi, \psi)$ is the vector describing small displacements of the platform, and \mathbf{F} is the vector of resulting forces and torques applied by the mounts on the platform. \mathbf{F} is related to the axial forces in each mount by

$$\mathbf{F} = B\mathbf{f} \quad (2.10)$$

where $\mathbf{f} = (f_1, f_2, \dots, f_6)^T$ is the vector of forces applied by the six mounts and B is the force Jacobian matrix to be calculated. Let also J be the Jacobian matrix relating the elongations velocities of the legs $\dot{\mathbf{q}}$ and the velocity vector $\dot{\mathbf{x}}$ as $\dot{\mathbf{q}} = J\dot{\mathbf{x}}$. According to the virtual work principle, we have

$$\mathbf{F}^T \delta \mathbf{x} = \mathbf{f}^T \delta \mathbf{q} = \mathbf{f}^T J \delta \mathbf{x} \quad (2.11)$$

After identification, we have $\mathbf{F} = J^T \mathbf{f}$. Comparing with (2.10) leads to $B = J^T$.

Assuming that there is no damping in the legs, the force f_i applied by the i^{th} support on the equipment is given by

$$f_i = k_a(-q_i + w_i^l) + u_i \quad (2.12)$$

where k_a is the axial stiffness of each leg, q_i and w_i^l are respectively the displacement of the platform and the ground in the direction of the mount, and u_i is the force applied by the actuator i .

Replacing (2.10) and (2.12) in (2.9) gives

$$M\ddot{\mathbf{x}} + K\mathbf{x} = k_a B \mathbf{w}^l + B \mathbf{u} \quad (2.13)$$

or again

$$M\ddot{\mathbf{x}} + K\mathbf{x} = k_a B E \mathbf{w} + B \mathbf{u} \quad (2.14)$$

where $K = k_a B B^T$ is the stiffness matrix, \mathbf{w} and \mathbf{w}^l are the ground excitation vector and the ground excitation vector in the cartesian frame and in the direction of the mounts, \mathbf{u} is the vector of control forces and E is the excitation matrix projecting \mathbf{w} in the directions of the mounts.

The analytical expression of J is found as follows. First, let us split the velocity vector $\dot{\mathbf{x}}$ into translational and rotational components such as $\dot{\mathbf{x}}^T = (\mathbf{v}^T, \omega^T)$ where $\mathbf{v}^T = (\dot{x}, \dot{y}, \dot{z})$ and $\omega^T = (\dot{\theta}, \dot{\phi}, \dot{\psi})$. Then, the velocity of the fixation point of leg i is

$$\mathbf{v}_i = \mathbf{v} + \omega \times \mathbf{p}_i \quad (2.15)$$

where \mathbf{p}_i is the coordinate of the extremity of mount i in the reference frame fixed on the platform. If $\mathbf{1}_i$ is a unit vector in the direction of mount i , the velocity of the extension of the mount is obtained by projecting \mathbf{v}_i along $\mathbf{1}_i$

$$\dot{q}_i = \mathbf{1}_i^T \mathbf{v}_i = \mathbf{1}_i^T (\mathbf{v} + \omega \times \mathbf{p}_i) \quad (2.16)$$

or

$$\dot{q}_i = \mathbf{1}_i^T \mathbf{v}_i = \mathbf{1}_i^T (\mathbf{v} - \mathbf{p}_i \times \omega) \quad (2.17)$$

Proceeding the same way for each mount, we have finally

$$J = \begin{pmatrix} \dots & \dots \\ \mathbf{1}_i^T & -\mathbf{1}_i^T \tilde{\mathbf{p}}_i \\ \dots & \dots \end{pmatrix} \quad (2.18)$$

where $\tilde{\mathbf{p}}_i$ is the antisymmetric matrix calculated from \mathbf{p}_i to express the cross product. In other words, with the positions where the mounts are attached to the platform and their relative orientations in the Cartesian frame of the platform, it is possible to easily derive the equations governing the dynamics of a multi-supported platform, and the transmissibilities from base to platform in the different directions.

Chapter 3

Whole Spacecraft Vibration Isolator

Contents

3.1 Active vibration isolator	35
3.1.1 Single degree of freedom isolator	37
3.1.2 Flexible payload mounted on three isolators	38
3.1.3 Mounting on flexible supports	43
3.1.4 Summary	44
3.2 Hybrid vibration isolator	44
3.2.1 Isolator architecture	46
3.2.2 Shunt selection	49
3.2.3 Criteria for parameter selection	53
3.2.4 Summary	56

Section 3.1 presents a novel concept of active mount for aerospace payloads. This approach reduces the magnification due to the first structural resonances of the suspension mode and preserves the vibration attenuation at high frequencies. It offers several advantages, including ease of mounting, high damping authority on both suspension resonances and flexible resonances without compromising the isolation and large stability margins of the closed loop system. The research carried out in this Section has been presented in [51]. Section 3.2 includes passive energy dissipation in the isolator in the form of a shunted piezoelectric stack which serves to reduce the power consumption of the system. The research presented in this section has been presented in [52].

3.1 Active vibration isolator

Since the world's first satellite was launched nearly sixty years ago, the technology of launchers and satellites has considerably improved. While in the early days, satellites were mounted on rigid supports, modern and more sensitive satellite equipment and instruments require better isolation from launcher disturbances [53]. To this purpose, passive suspensions have been progressively introduced. Mounting the satellites on passive suspensions produces a filtering of high frequency vibrations [3, 21, 54]. The softer the suspension, the better the isolation.

However, this comes at the expense of large and harmful amplifications of the lower frequency suspension modes [55], and raises concerns about strength and clearance issues because of the larger compliance. This is the first fundamental limitation of passive isolation [17].

The amplification at resonance can be reduced by increasing the damping in the isolator. However, this comes in turn at the expense of a reduction of the isolation at high frequency. This is the second fundamental limitation of passive suspensions.

The only way to bypass the shortcoming above and simultaneously eliminate the resonance response of the suspension mode while avoiding a degradation of the attenuation at high frequencies, is to use active vibration isolation systems. They do not show such amplifications at low frequencies and are capable of an overall damping performance. Considerable efforts on active [24, 56–58] and semi-active vibration isolators [59, 60] have been carried out. However, active isolation does not come without drawbacks. The first one is the concern of stability and robustness of the control system, which in the previous section was addressed by using a collocated pair formed by a sensor and an actuator. The second issue with active strategies is the need for a power supply, which incurs a significant weight penalty for the spacecraft.

The hybrid isolator presented in this chapter combines the high performance of active control with a reduced power consumption thanks to passive control. It is composed of a compliant metallic structure with an integrated sensor and a piezoelectric actuator. An example of this configuration is shown in Fig. 3.1. It consists of an elliptic, metallic structure that plays the role of suspension. Additionally, a piezoelectric stack actuator has been placed inside the structure, along the horizontal axis of the ellipse. The stack is further divided into two parts, respectively used as an actuator and as a force sensor, and both constitute a perfectly collocated pair.

In each mount, the actuator will be driven only by using the signal from the force sensor of the same mount. Both suspension resonances and payload resonances

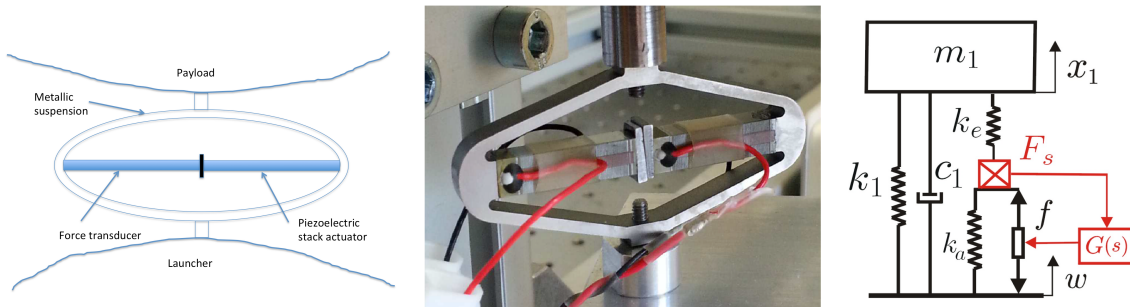


Figure 3.1: From left to right: Concept of active isolator; Picture of an APA 100M from Cedrat-Technologies used for the experiments (one piezoelectric stack is used as a force sensor and the other one is used as an actuator); Simplified model of a one DOF payload mounted on such isolator

are actively damped by applying viscous damping forces obtained by integrating the signal from the force sensors [18]. Such control strategy, known as Integral Force Feedback (IFF) has been extensively discussed in [19, 61, 62]. In the proposed configuration, it can also be noticed that the softening effect inherent to force control is limited by the metallic suspension, which will also continue to work as a passive isolator in case of failure of the piezoelectric stack.

The advantages of this mount are:

1. Modularity: the number and position of mounts will depend on the mass and inertia of the payload and the specific mechanical environment
2. The elliptical shape works as both a suspension spring and as a mechanical amplifier to increase the range of the actuator
3. Each unit is stand-alone comprising both sensor and actuator
4. The control architecture using decentralized feedback loops in each active mount, offers excellent stability margins

Although the full design of the suspension will require a complete study, the objective of this preliminary work is to test experimentally the concept using a commercial isolator. To this purpose three set-ups of increasing complexity have been developed: one DOF payload mounted on one isolator, a flexible payload mounted on three isolators, and the whole structure including the isolators mounted on a flexible base. They are presented in the following subsections.

3.1.1 Single degree of freedom isolator

Figure 3.1 shows a picture of the amplified piezoelectric stack used for the experiments. It is an APA 100M from Cedrat-Technologies, where the piezoelectric actuator has been divided into two parts: one is used as an actuator, and the other one is used as a force sensor. A small mass has been mounted on the actuator to represent a single DOF payload. A simplified sketch of the system is shown in Fig. 3.1 (right). In this model, k_1 represents the stiffness of the metallic suspension when the stack is removed; k_a is the stiffness of the actuator; k_e is the stiffness used to adjust the pole of the isolator; w is the motion imposed by launcher; F_s is the force sensor; f is the actuator; $G(s)$ is the controller; x_1 is the motion of the payload; c_1 is a viscous damper used to match experimental results. The dynamic equation of the system is:

$$m\ddot{x}_1 = \left(-k_1 - \frac{k_e k_a}{k_e + k_a}\right) x_1 + \left(k_1 + \frac{k_e k_a}{k_e + k_a}\right) w - c_1 \dot{x}_1 + c_1 \dot{w} + F + \left(\frac{k_e}{k_e + k_a}\right) f \quad (3.1)$$

The expression of the force measured by the force sensor is

$$F_s = \left(-\frac{k_e k_a}{k_e + k_a}\right) x_1 + \left(\frac{k_e k_a}{k_e + k_a}\right) w + \left(\frac{k_e}{k_e + k_a}\right) f \quad (3.2)$$

The control force is given by

$$f = -F_s G(s) \quad (3.3)$$

where $G(s) = g/s$ and g is the control gain.

Figure 3.2 shows the matrix of transfer functions from input (w, f, F) to output (F_s, x_1) in open loop (blue curves) and closed loop (dashed red curves). The following numerical values have been used for the simulation: $m = 1$ kg; $k_e = 4.8$ MN/m; $k_1 = 960$ kN/m; $k_a = 65$ MN/m; $c_1 = 0$ Ns/m. These values have been chosen to have a matching between the theoretical and the experimental open loop transfer function $\frac{F_s}{f}$.

Firstly, it can be noticed on the transmissibility that the resonance peak is almost critically damped, without compromising the high-frequency passive isolation for frequencies higher than the resonance of the suspension. Secondly, the degradation of the compliance induced by the feedback operation is limited at $1/k_1$ as anticipated. Thirdly, the fraction of the force transmitted to the payload that is measured by the force sensor is reduced not only at the resonance, but also in a broad frequency range at low frequencies.

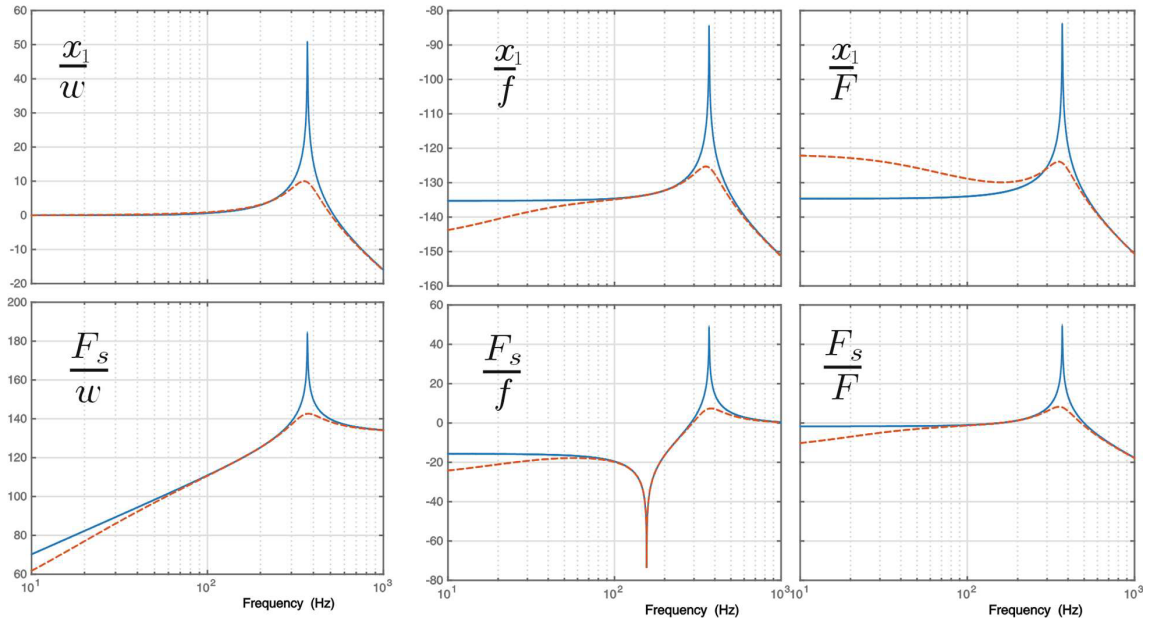


Figure 3.2: Matrix of transfer functions from input (w, f, F) to output (F_s, x_1) in open loop (blue curves) and closed loop (dashed red curves)

The experimental setup shown in Fig.3.3 is aimed at verifying the simulated results. One of the piezoelectric stacks is used as an actuator, to inject white noise in the frequency band from 10 to 500 Hz. The second piezoelectric stack is used as a sensor. Increasing values of the gain are used in the active control loop, and the resulting open loop transfer function is computed. Figure 3.4 compares the theoretical (solid curves) and experimental (dashed curves) closed loop transfer functions between the sensor and the actuator obtained for various values of the control gain. It clearly shows the high efficiency of the isolator and a good match between the model and the experiment. The experimental data are further compared with the model in Fig. 3.5, which shows the trajectory of the closed loop poles in the complex plane. The experimental points have been obtained by fitting the measured closed loop transfer function.

The minor mismatch between the theory and the experiment is attributed to the fit algorithm which has been used to calculate the value of the closed loop poles because highly damped poles are difficult to fit precisely.

3.1.2 Flexible payload mounted on three isolators

The second set-up considered consists of a heavier payload, mounted on a set of three isolators. The payload consists of two masses, connected through three flexible blades with a tunable length. The set-up is shown in Fig. 3.6, along with a simplified

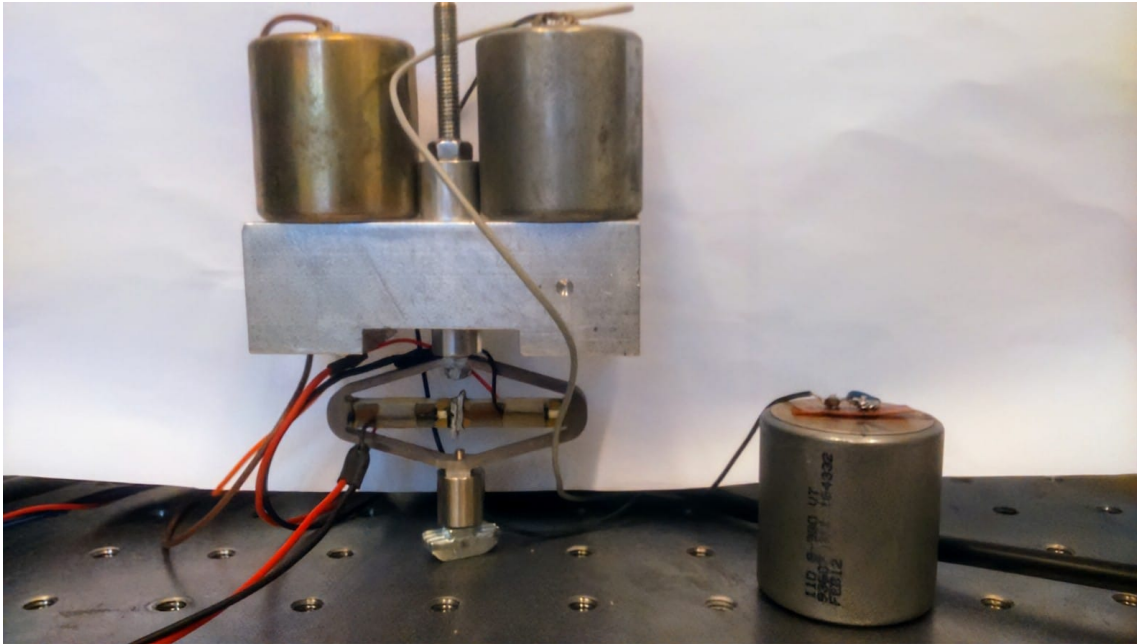


Figure 3.3: *Experimental setup showing the active mount with a dummy mass on top*

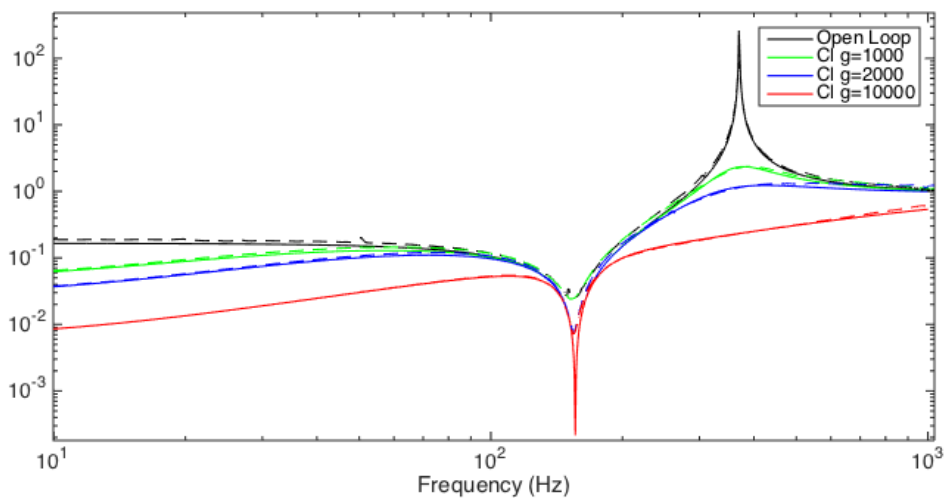


Figure 3.4: *Open loop and closed loop transfer function between the actuator and the force sensor. Comparison between the model (solid curve) and the experiment (dashed curve)*

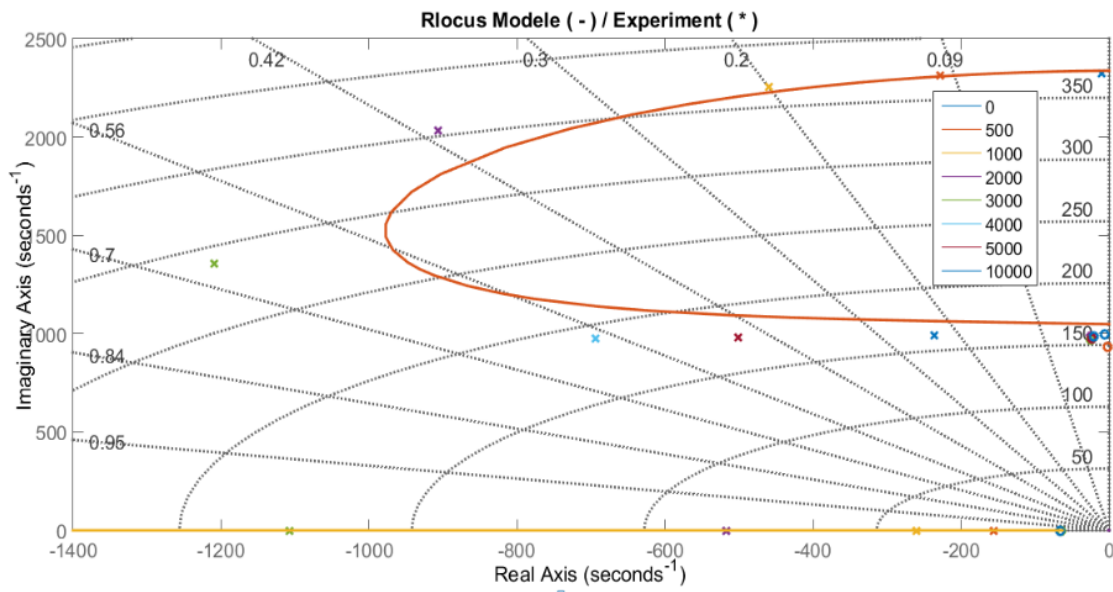


Figure 3.5: Single DOF system. Comparison between the theoretical (solid curve) and the experimental (crosses) root-locus

sketch showing only the vertical DOF of the payload, mounted on one isolator.

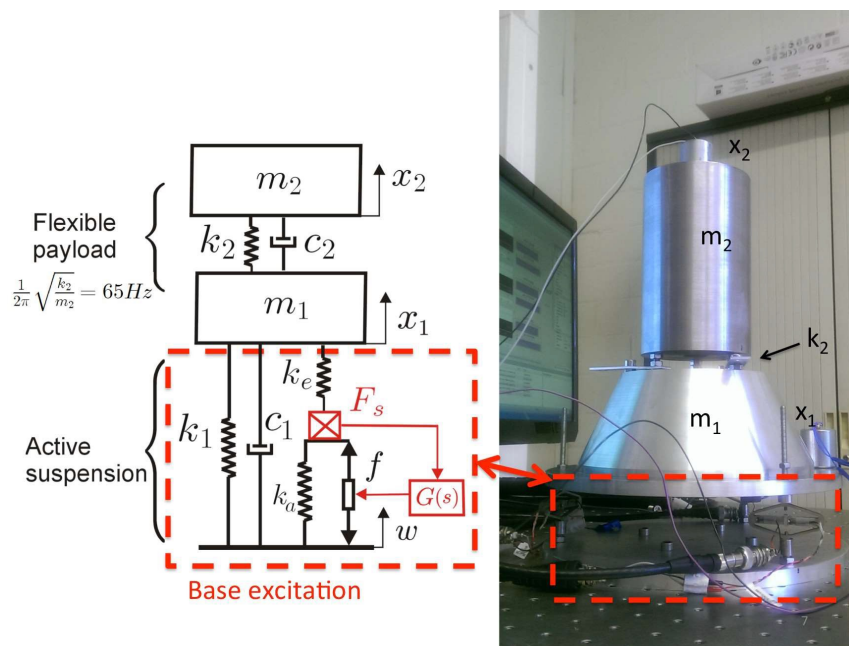


Figure 3.6: Right: Picture of the experimental set-up. It consists of a flexible payload mounted on a set of three isolators. Left: a simplified sketch of the set-up, showing only the vertical direction

The flexible resonance of the payload in the vertical direction has been tuned around 65 Hz. It corresponds roughly to the resonance of m_2 while m_1 is blocked. The first six mode shapes and corresponding resonance frequencies are shown in Fig 3.7.

The set-up has been mounted on a passive optical table. A shaker has been mounted on the tabletop beside the set-up in order to excite it from the base as for the launcher.

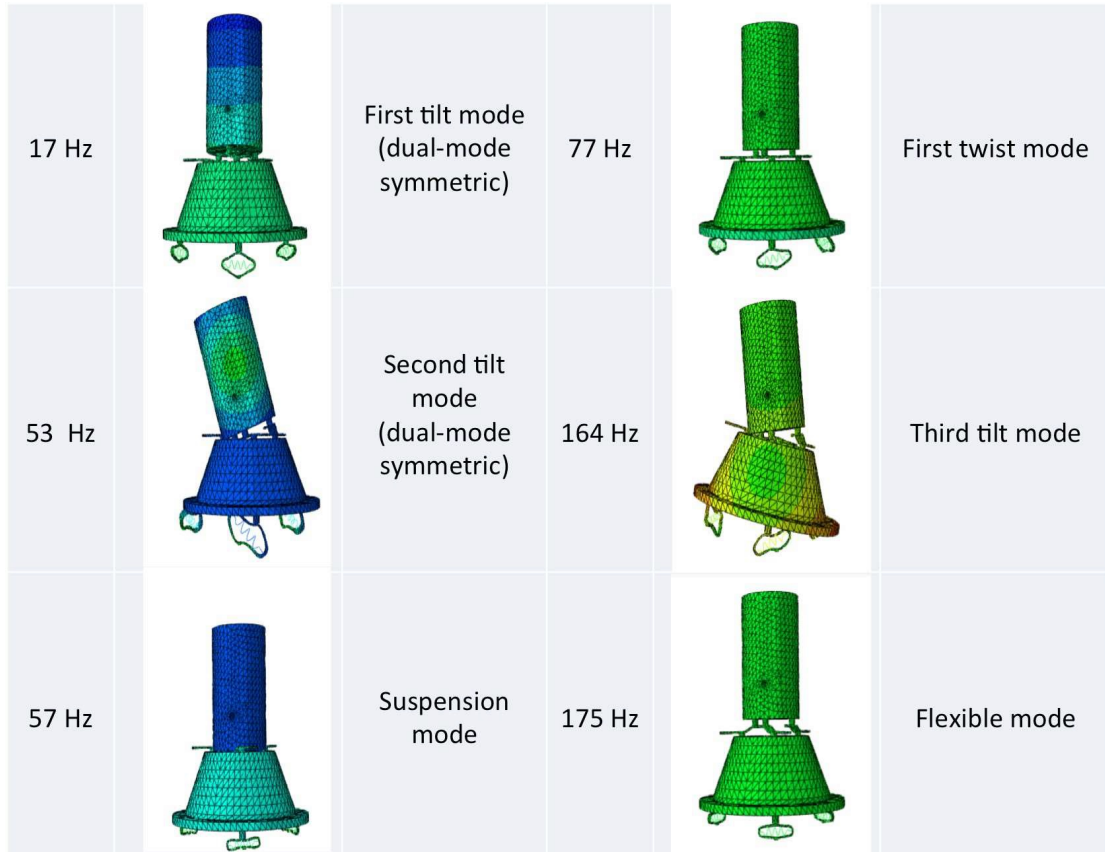


Figure 3.7: Mode shapes and corresponding resonance frequencies of the first 6 modes

Two test campaigns have been conducted: one when the shaker excites the table in the vertical direction, and one when the shaker excites the table in the horizontal direction. For each case, random white noise from a shaker is used as the input disturbance to the system. For both campaigns, decentralized control loops have been used. Typical experimental results are shown respectively in Fig. 3.8 - 3.9. For both figures, the same quantities are shown. Top left: transfer function between the shaker noise and one force sensor; bottom left: integrated (downwards) RMS value of the force measured by one force sensor; top right: transmissibility between the table top w and m_2 ; bottom right: transmissibility between the table top w and m_1 . For both campaigns, one sees that both the suspension modes and the flexible modes of the payload can be critically damped. Furthermore, the fraction of the force transmitted to the payload that is measured by the force sensor is also significantly reduced by up to two orders of magnitudes around the resonances, and the RMS value is reduced by a factor of 5.

Active vibration isolator

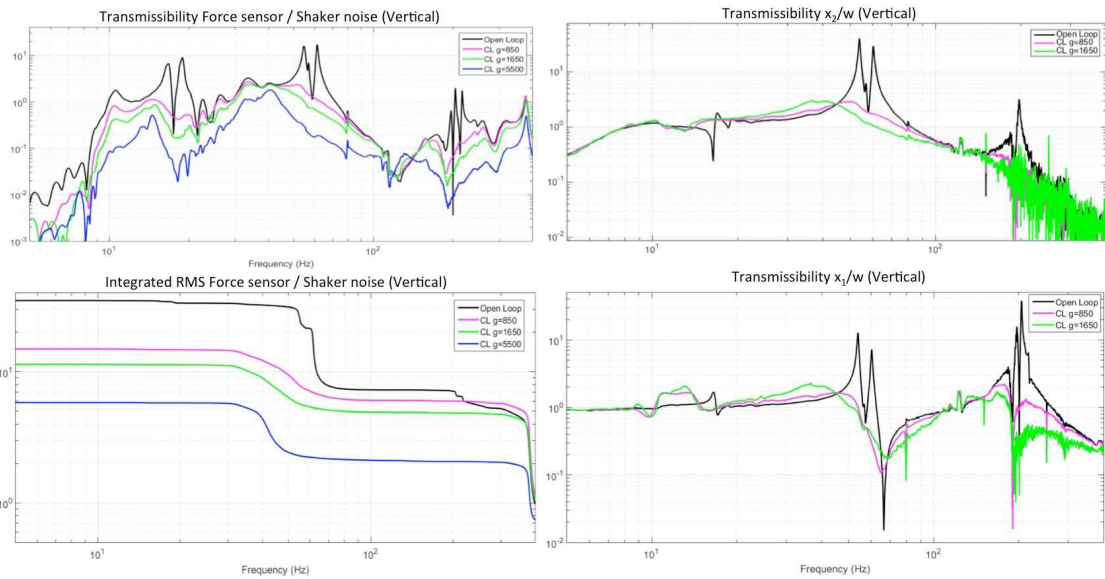


Figure 3.8: Vertical excitation. Top left: transfer function between the shaker noise and one force sensor; bottom left: integrated (downwards) RMS value of the force measured by one force sensor; top right: transmissibility between the table top w and m_2 ; bottom right: transmissibility between the table top w and m_1

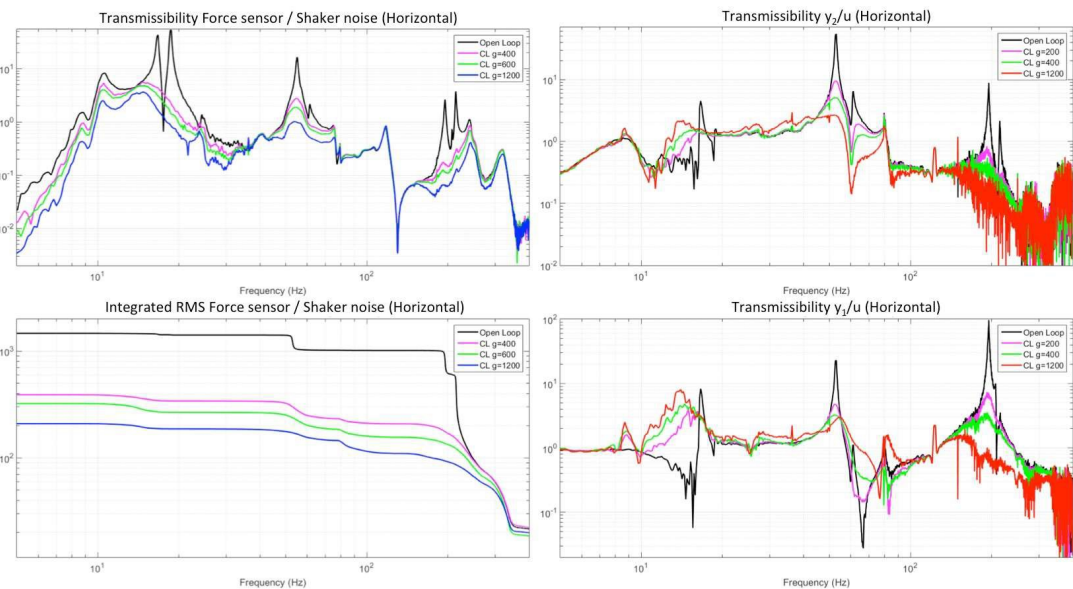


Figure 3.9: Horizontal excitation. Top left: transfer function between the shaker noise and one force sensor; bottom left: integrated (downwards) RMS value of the force measured by one force sensor; top right: transmissibility between the horizontal motion of the table top (u) and horizontal motion of m_2 (y_2); bottom right: transmissibility between the horizontal motion of the table top (u) and horizontal motion of m_1 (y_1)

It has to be noticed that a degradation of the horizontal response is visible when excitation is horizontal. The origin of this behavior has not been investigated in detail. It is likely due to an interaction of the tilt mode with the high frequency filter used in the controller, but could also be caused by a softening effect due to the controller.

3.1.3 Mounting on flexible supports

The third set-up considered in this study is shown in Fig 3.10. It is the same as in the previous section, except that a flexible support has been introduced between the isolator and the tabletop. The flexible support consists of a steel plate (m_0 in Fig. 3.10) mounted on four commercial rubber mounts. The objective of this experiment is to test the robustness of the controller in the presence of flexibilities on both sides of the isolator.

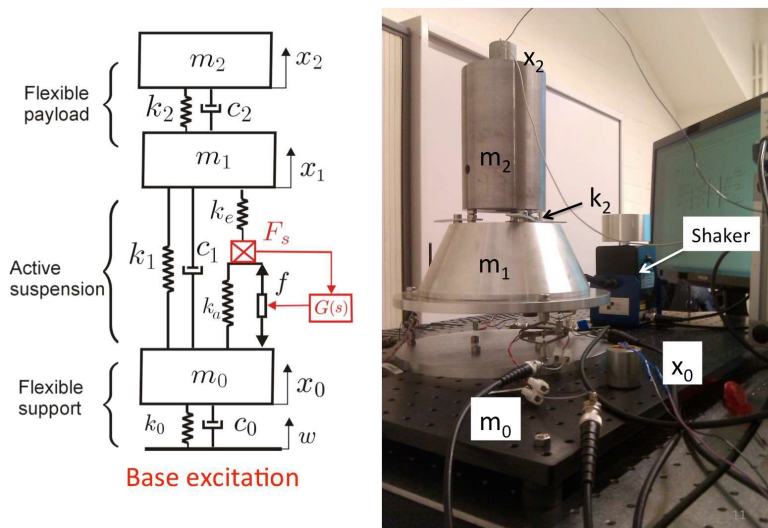


Figure 3.10: Flexible payload mounted on a set of three isolators, including a flexible structure below the isolator: picture and simplified sketch showing only the vertical direction

The same experimental campaign has been conducted: base excitation in both the vertical and horizontal direction with a shaker mounted on the tabletop, as shown in Fig. 3.10. As an illustration, Fig. 3.11 shows the transmissibility between the flexible support and the payload for various values of the control gain, when the structure is excited in the vertical direction. This figure has to be compared with the right part of Fig. 3.8. Although the modal density is larger, one can still clearly identify the first and the second resonances, respectively around 60 Hz and 190 Hz. The authority on these modes remains unchanged, and no stability issue has been encountered.

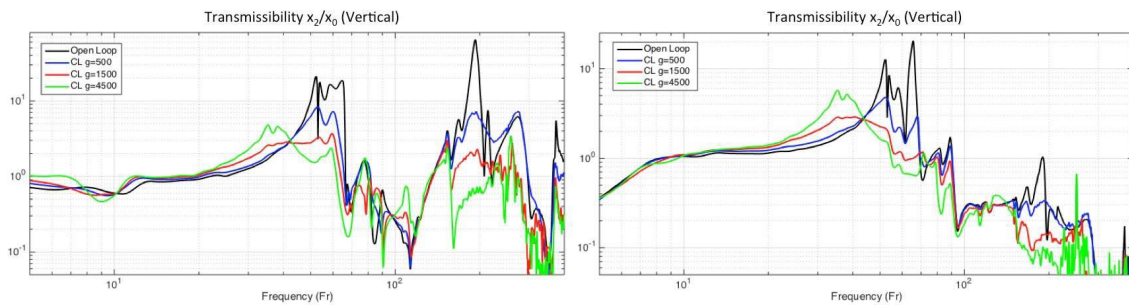


Figure 3.11: *Transmissibilities x_1/x_0 and x_2/x_0 between the flexible support and the payload for various values of the control gain, when the structure is excited in the vertical direction*

Similar results have been obtained for the excitation in the horizontal direction, and the reduction of the force transmission is also similar to those shown in Fig. 3.8-3.9.

3.1.4 Summary

A concept of an active isolator for space payloads exposed to launch vibration has been proposed in this section. The isolator comprises a metallic suspension, and a collocated pair of piezoelectric sensor and actuator. The advantages of this concept are that the number and position can be adjusted easily and that it combines high authority and good robustness. The concept has been validated experimentally using a commercial actuator on three set-ups of increasing complexity, ranging from a single DOF payload to a flexible payload, isolated by three active mounts installed on a flexible structure.

3.2 Hybrid vibration isolator

With the objective of reducing the power consumption, while at the same time maintaining the inherent stiffness of the system to accepted levels, a passive component is added to the active isolation system presented in the Sec. 3.1. The passive isolation is carried out by a shunted piezoelectric stack, which instead of being connected to a power supply is connected to a resistive/inductive load -extracting part of the energy from the system- and thus contributing to the isolation of the system [63, 64]. A schematic of the piezoelectric shunt with the two studied shunts is presented in Fig. 3.12. This section shows that an accurate representation of the model has been achieved through Matlab and that there is potential in combining active and passive isolation strategies which allow for reduced power consumption. Finally, an analysis

is done to optimize the system's parameters.

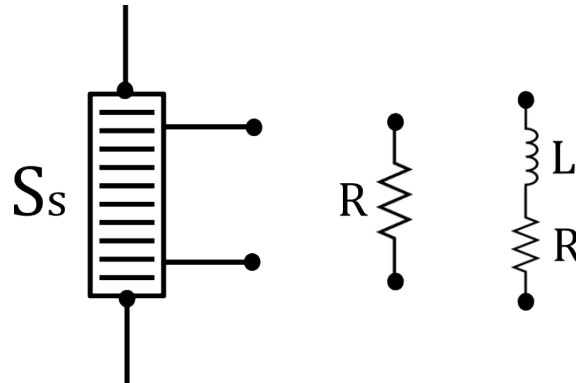


Figure 3.12: Piezoelectric stack with shunt connection (S_s) and the two shunt options studied: Resistive (R) and Resistive-Inductive (RL)

A first attempt to conceive a hybrid isolator was made by shunting the sensor stack presented in Fig's. 3.1 and 3.3 with a resistive load. Injecting white noise in the actuator and progressively increasing the gain of the active control loop allows us to reconstruct the root locus of the system. Results from both analytical and experimental tests are shown in Fig. 3.13. From the root locus, it can be seen that the shunt shifts the root locus of the active control further towards regions with higher damping. Although promising as a first iteration towards developing a hybrid isolator, by shunting the stack used as a sensor, its output was modified in such a way that it was no longer representative of the force transmitted at that location, which in turn reduced the maximum damping achievable through active control.

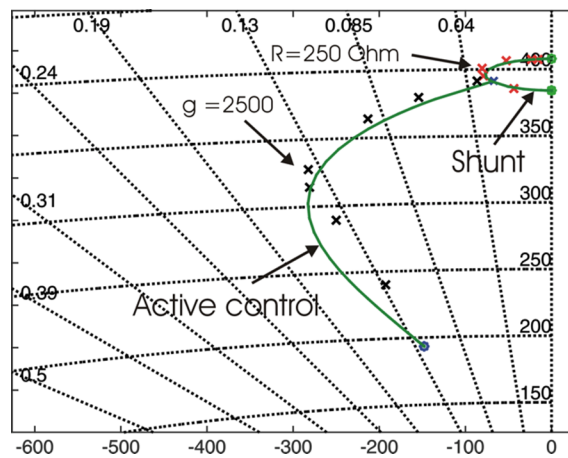


Figure 3.13: Root locus of experimental (crosses) and analytical results (solid line) of the active isolator in 3.1 where the sensor stack is shunted with a resistance

3.2.1 Isolator architecture

The addition of a shunted stack to the system does not only call for the evaluation of the optimal shunt and its parameters but also for a review of the architecture to use in the isolator to hold the third stack.

This raises the need to evaluate how the new stack should be connected in relation to the other stacks, and to the structure. A consideration to carry this out is that, in order to keep the collocated sensor-actuator setup, the corresponding stacks have to be kept in series. Two basic configurations are studied: one setup in series, where all of the stacks are placed in line with each other, and another one where the stacks are connected in parallel, with the shunted stack in parallel to the sensor and actuator stacks, both in series with respect to one another. Fig. 3.14 illustrates a basic representation of the series and parallel configurations.

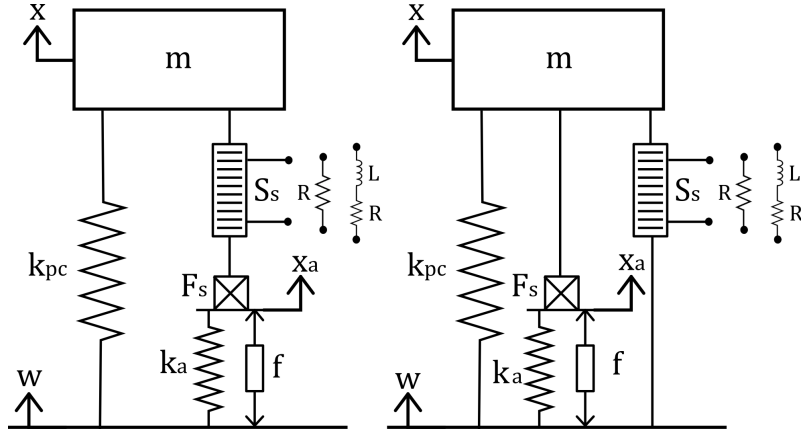


Figure 3.14: Schematic of the series (left) and parallel (right) hybrid isolator configurations. S_s represents the shunted piezoelectric stack

The following nomenclature applies: k_{pc} is the stiffness of the structure, K is the stiffness of the shunted piezoelectric stack, k_a is the stiffness of the active stack, k is the stiffness coefficient of the shunt with short circuited electrodes, x is the motion of the mass m , w is the motion of the base, x_a is the motion of the active stack, S_s represents the shunted stack, f_p is the force of the shunted piezoelectric stack, F_s is the force measured by the sensor stack, f is the force at the actuator stack, V_p is the voltage at the shunted stack, Q_p is the charge flowing through the shunt, C is the capacitance of each piezoelectric stack, n is the number of piezoelectric layers per stack, d_{33} is the piezoelectric modulus of each layer, k_2 is the electromechanical coupling factor, m is the mass of the system, F is the resultant force on the mass. This nomenclature applies to both models. The analytical expressions pertaining to the series and parallel configurations are gathered in Eq. (3.4) and Eq. (3.5) respectively.

$$\begin{cases} V_p = \frac{K}{C(1-k^2)} \left(\frac{Q_p}{K} - nd_{33}(x - x_a) \right) \\ f_p = \frac{K}{C(1-k^2)} (C(x - x_a) - nd_{33}Q_p) \\ m\ddot{x}_1 = -f_p + F - k_{pc}(x - w) \\ F_s = -k_a(x_a - w) + f \\ F_s + f_p = 0 \end{cases} \quad (3.4)$$

$$\begin{cases} V_p = \frac{K}{C(1-k^2)} \left(\frac{Q_p}{K} - nd_{33}(x - w) \right) \\ f_p = \frac{K}{C(1-k^2)} (C(x - w) - nd_{33}Q_p) \\ m\ddot{x}_1 = -f_p + F_s + F - k_{pc}(x - w) \\ F_s = -k_a(x_a - w) + f \end{cases} \quad (3.5)$$

The advantage of using a collocated sensor and actuator controlled in a decentralized manner is that no knowledge of the plant is required. In this case, the control architecture is the same as that presented in the previous section and consists of a simple integrator coupled with a high-pass filter to avoid low frequency saturation.

Since the main goal of the introduction of the shunt is to reduce the power consumption of the system, the two configurations are evaluated with respect to the control effort needed to achieve equal performance levels. The control effort, in this case, is the transfer function between the force measured by the sensor, which is proportional to the power consumed by the system ($f = -F_s H(s)$), and the base input motion F_s/w . Although with this method the actual values of power consumption are not obtained, this transfer function serves as a quantitative comparison of the power consumption of one system with respect to the other. Higher values of this transfer function represent a higher power draw by the active system.

The optimal value of the resistance is that for which the highest level of damping is obtained, which corresponds to the left-most point in the root locus of the system corresponding to the first mode (green curve) shown in Fig. 3.15. This point is identified graphically and through Eq. 3.6 [61] the value of the resistance is obtained. Where G is the gain, R is the value of the resistance, C is the capacitance of the piezoelectric stack, and z and p are the frequencies of the pole and zero. The gain of both systems is then tuned to provide equal levels of damping. Fig. 3.16 verifies this by showing the same magnitude at the resonance frequency in the transmissibility for the different systems. This is done to be able to evaluate the control effort

Hybrid vibration isolator

requirements of each system for equal levels of performance.

$$G = \frac{1}{RC} = \frac{z - p}{2p} \quad (3.6)$$

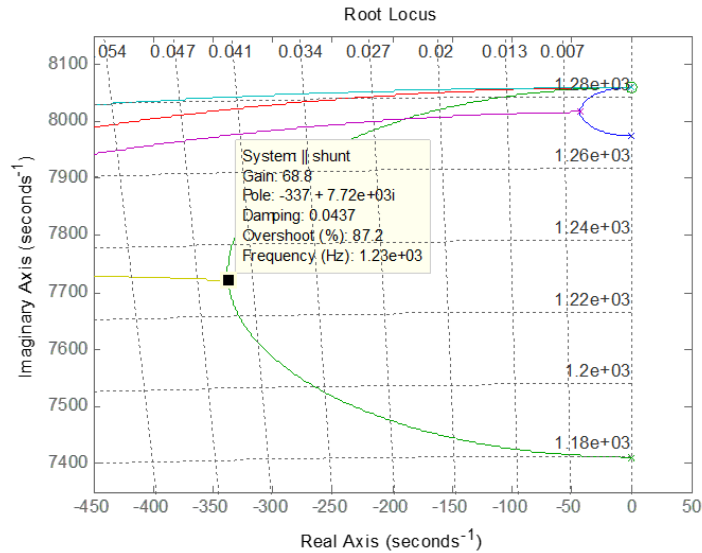


Figure 3.15: Root locus showing the correlation between resistance and damping, where the location of the pole connecting the yellow and green loops is a function of the value of the resistance in the shunt

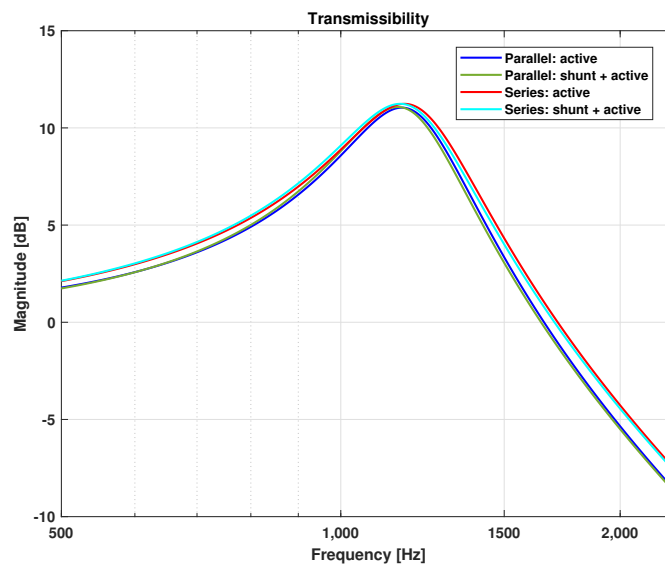


Figure 3.16: Transmissibility between the two sides of the isolators shown in Fig. 3.14, where the control gain and shunt parameters have been tuned for equal behavior and performance

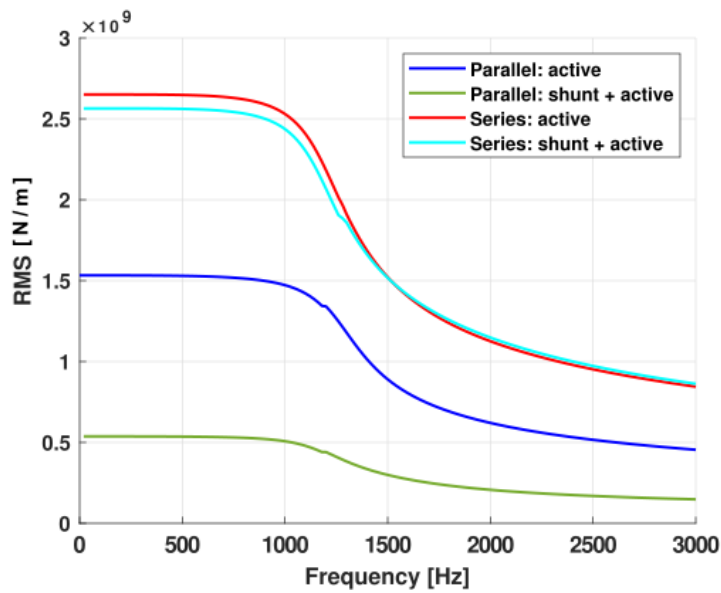


Figure 3.17: Control effort required to drive the actuator with the different strategies, to achieve the performance levels seen in Fig. 3.16

In Fig. 3.17 a decrease in control effort can be seen when the shunt is added to both configurations, with respect to when no shunt is included, but both the control effort and the effect of including the shunt are better for the parallel setup. Using the parallel setup, the addition of the shunted stack provides a further reduction of the control effort of 60% with respect to the series setup. For equal performance, the parallel configuration requires less power because the force is directly applied to the mass, without being filtered by the passive component.

It is therefore concluded that further work will be carried out with the parallel configuration.

3.2.2 Shunt selection

Maintaining the parallel configuration, the focus is now shifted towards determining the optimal shunt type. As demonstrated in [65], shunting a piezoelectric stack with a resistance is the equivalent of adding a viscoelastic element to the system. If an inductance is added in series to the resistance, a resonant circuit is created. This circuit has been proven to work as a dynamic vibration absorber (DVA) when correctly tuned [65]. Both behaviors are of interest for this application and are evaluated in this section.

In order to assess the performance of the two shunt typologies, simulations are

Hybrid vibration isolator

initially run on a 1 DOF system (identical to the parallel system in Fig. 3.14).

As can be observed in Fig. 3.18 the strategy with the inductive shunt emulates the effects of a DVA as predicted, validating the model. Furthermore, while there is an overall improvement in the response of both strategies while carrying out exclusively passive damping, there is a notable increase in damping when the active system is engaged. The gain of each of the three active systems is manually tuned to have the same magnitude of the transmissibility (presented in Fig. 3.18) for the three active strategies, to evaluate their control effort.

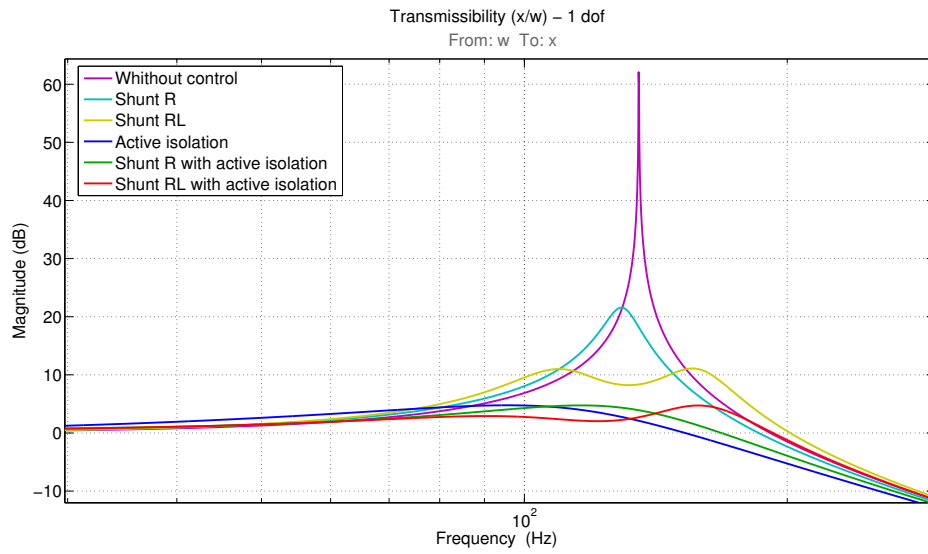


Figure 3.18: *Transmissibility of the 1-DOF model for the different strategies*

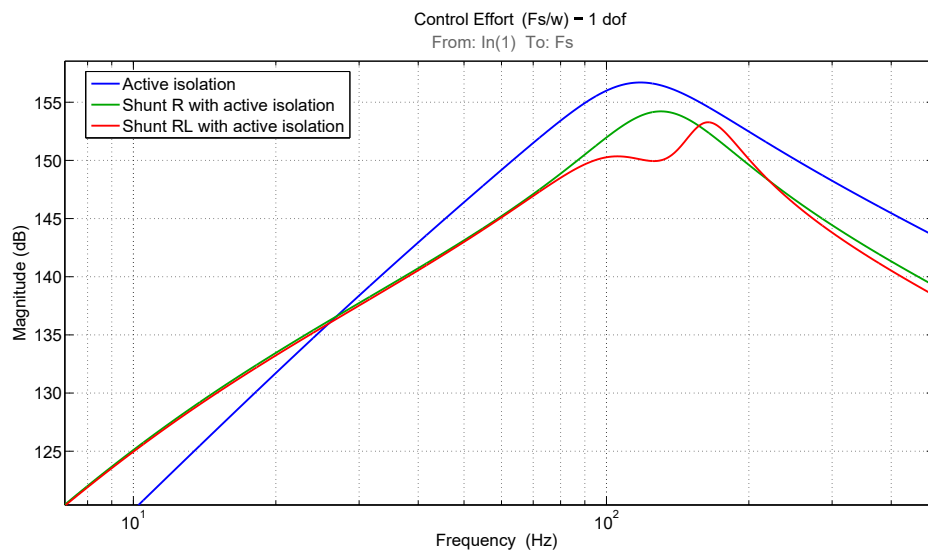


Figure 3.19: *Control effort required to drive the actuator with the different strategies to achieve the performances shown in Fig. 3.18*

Regarding the control effort shown in Fig. 3.19, all three curves follow an expected trend, with the peak of control effort at the resonance frequency, as it is there where most force is demanded from the actuator. At the resonance, the passive elements of the shunt dissipate energy from the system, providing damping and reducing the power requirements of the active part of the isolator. Up to the resonance frequency of the system both hybrid strategies are identical, and therefore showcase very similar behaviour. At the resonance frequency of the system, the inductive shunt shows a further improvement demonstrating the difference between inserting a viscoelastic material (the resistive shunt) or a DVA (the inductive shunt).

To further evaluate these results, the same tests were carried out on a 2-DOF system shown in Fig. 3.20 to evaluate the broadband potential of each configuration. The governing equations for the 2-DOF are gathered in Eq. 3.7. Where k_2 and c_2 represent the stiffness and damping connecting the masses m_1 and m_2 , and x_2 is the motion of the mass m_2 .

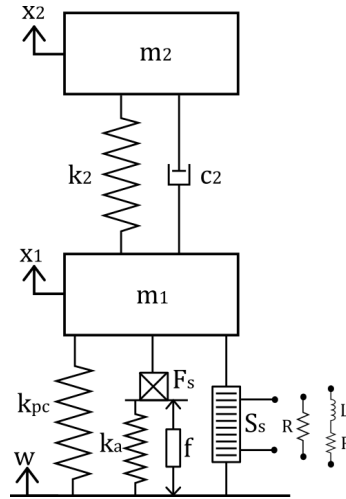


Figure 3.20: Schematic of the 2-DOF model in the parallel configuration

$$\begin{cases} m_2 \ddot{x}_2 = -k_2(x_2 - x_1) - c_2(\dot{x}_2 - \dot{x}_1) \\ m_1 \ddot{x}_1 = k_2(x_2 - x_1) + c_2(\dot{x}_2 - \dot{x}_1) - k_{pc}(x_1 - w) - f_p + F_s + F \\ V_p = \frac{K}{C(1 - k^2)} \left(\frac{Q_p}{K} - nd_{33}(x_1 - w) \right) \\ f_p = \frac{K}{C(1 - k^2)} (C(x_1 - w) - Q_p nd_{33}) \\ F_s = -k_a(x_1 - w) + f \end{cases} \quad (3.7)$$

In Fig. 3.21 it can be observed that for the first mode, the best strategy in

terms of performance is the combination of active control with the inductive shunt. However, for the second mode, this strategy underperforms when compared both to the resistive shunt and to the standalone active control, and the hybrid strategy with the resistive shunt shows the best results. This can be easily understood by recalling the analogy of the inductive shunt to a DVA, which, while very effective at damping disturbances in a narrow frequency band, is unable to achieve broadband isolation. The results related to the control effort are shown in Fig. 3.22. It can be seen that the control effort drawn in the first mode is similar to that of the 1-DOF system, with the inductive shunt as the most efficient solution. In the second mode, the inductive shunt surpasses the resistive shunt at the peak and quickly falls to lower levels. However, as can be seen in Fig. 3.21, the performance of the inductive shunt is below that of the resistive shunt, resulting in a lower efficiency for this mode. The control effort required to achieve the target performance for each strategy is related to the performance of the passive strategies. The farther away in terms of magnitude that a passive strategy is from the target, the higher the control effort required by the active system is needed in order to reach the target. This is confirmed when observing how for the second mode, contrary to the behaviour in the first mode, the resistive shunt strategy shows lower control effort than the inductive shunt strategy.

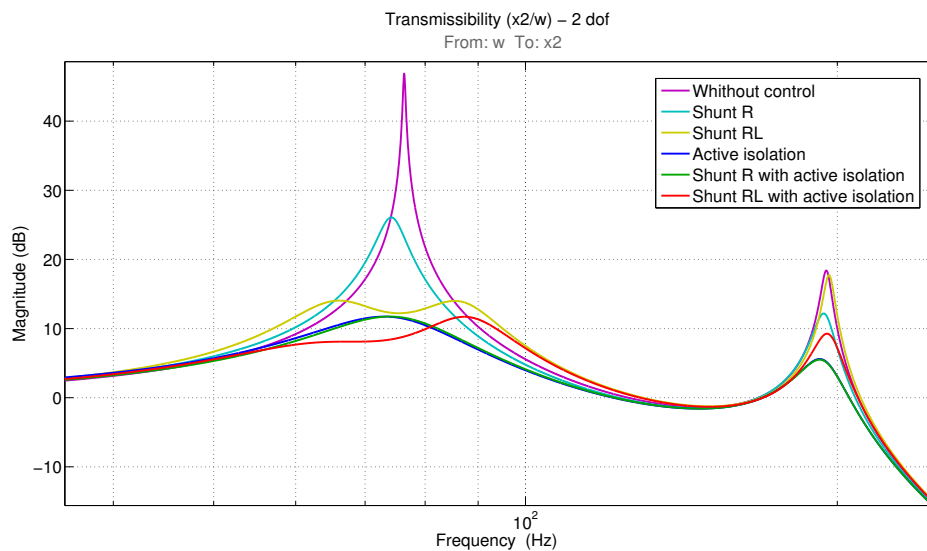


Figure 3.21: *Transmissibility of the 2-DOF model for the different strategies*

Considering the results shown in this section, it can be concluded that the control effort, and thus the power consumption of the active system can be reduced by the introduction of a shunted piezoelectric stack, while at the same time improving its performance. In cases where the interest is to reduce the magnification at a defined frequency, an inductive shunt has been proven to be the most efficient solution once

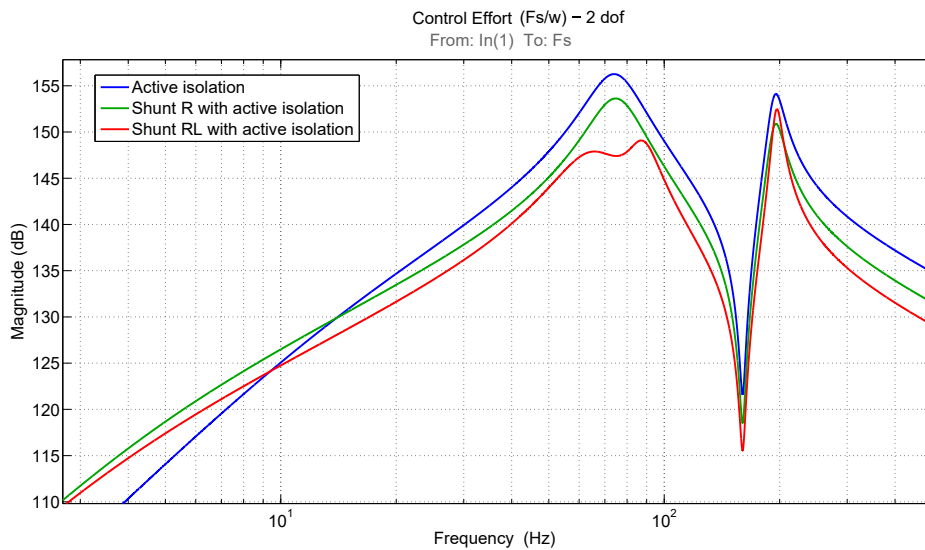


Figure 3.22: Control effort required to drive the actuator with the different strategies to achieve the performances shown in Fig. 3.21

tuned to target a small frequency range. However, when the objective is to obtain broadband isolation, a resistive shunt proves to be better suited.

3.2.3 Criteria for parameter selection

This subsection details the development of a methodology that facilitates the optimal choice of the different parameters of the isolator. While keeping the overall stiffness of the isolator constant at a value of 10^8 N/m, the values corresponding to the stiffness of the active and passive subsystems are varied according to Eq. 3.8, with the goal of understanding the effect that these parameters have both on the control effort and the performance of the isolator. Where k_a is the stiffness of the active stack, K is the stiffness of the shunted stack, and k^2 is the electromechanical coupling factor. The tests are carried out with the 2-DOF model, where a standalone active isolator is compared to a hybrid isolator equipped with a purely resistive shunt.

$$\frac{K}{1 - k^2} + k_a = 10^8 \quad (3.8)$$

The first study is dedicated to finding the relationship between the stiffness ratio of the active and passive components, and the control effort required to drive the system. The gain of both systems is manually tuned so that the magnitude of the resonance of the first mode is equal. The root mean square (RMS) of the control effort transfer function is computed for each value of the ratio k_a/K . The results are shown in Fig. 3.23. At the left-hand side, close to the origin, most of the stiffness is

assigned to the passive isolator. Consequently, the control effort required is very low. As the values of the x-axis increase, so does the stiffness of the active component, while that of the passive component decreases. As a result of this, the control effort increases, and as the stiffness of the passive subsystem approaches zero, the power draw of the hybrid system resembles that of a purely active system.

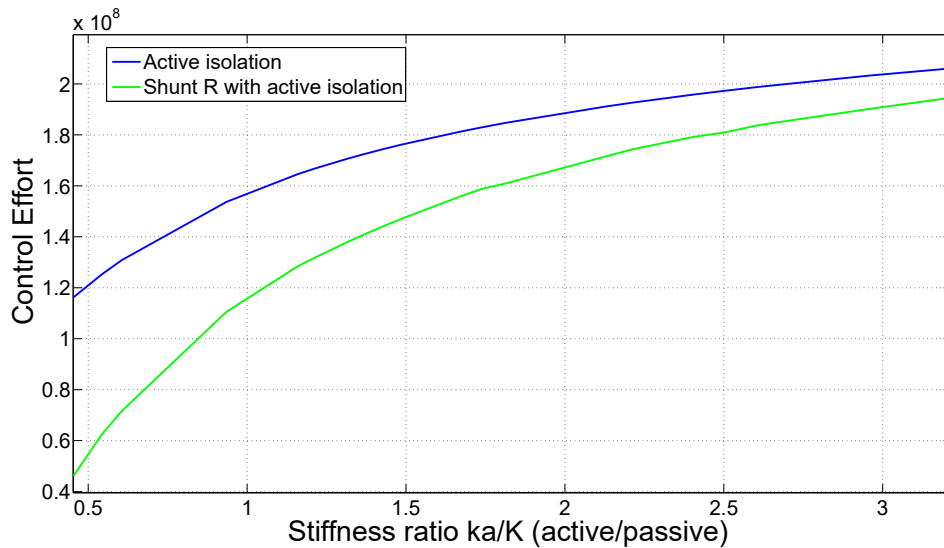


Figure 3.23: Relationship between stiffness ratio and control effort (F_s/w in N/m) for equal transmissibility performance

The following step investigates the correlation between damping and control effort with respect to the stiffness ratio. For optimal performance, the maximum damping for each of the two modes is computed and plotted against the RMS of the control effort required. By doing this iteratively while modifying the stiffness ratio, Fig. 3.24-3.25 are obtained for the first and second modes respectively. From these figures, knowing the damping that is required for a certain application, a specific stiffness ratio can be selected for the design of the isolator, while retrieving the control effort that will be required to drive the isolator. As expected from the results of the previous section, the control effort required for the standalone active system is always higher than that of the hybrid system.

The final simulation shows the correlation between the damping of the first and second modes for a given stiffness ratio while providing information on the control effort required. To obtain it, a specific stiffness ratio is selected, the value of the gain is changed until the maximum achievable damping is reached. The maximum damping of both modes is computed as well as the RMS of the control effort required to achieve it. In Fig. 3.26 the same trend as in the previous figures can be observed, where the hybrid strategy shows higher efficiency levels than the standalone active

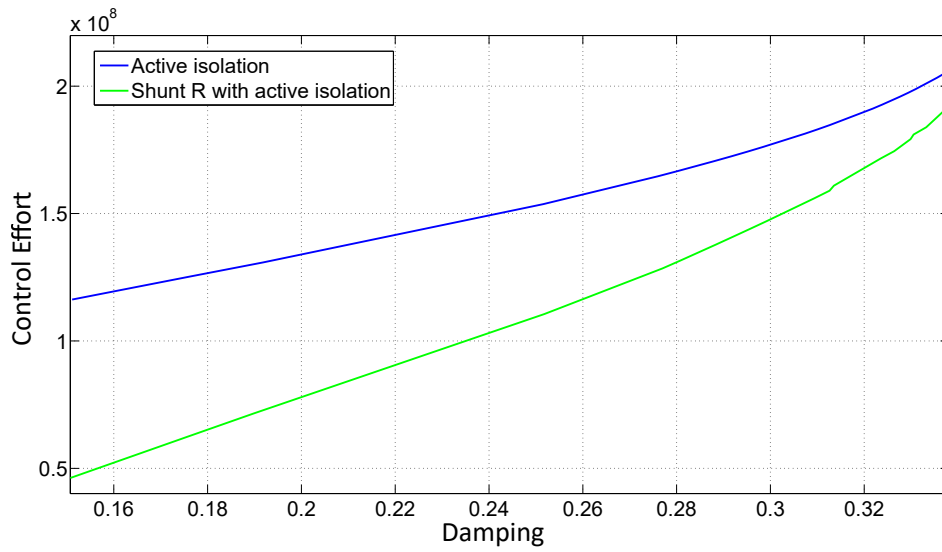


Figure 3.24: Relationship between damping and control effort (F_s/w in N/m) for varying the stiffness ratios. First mode

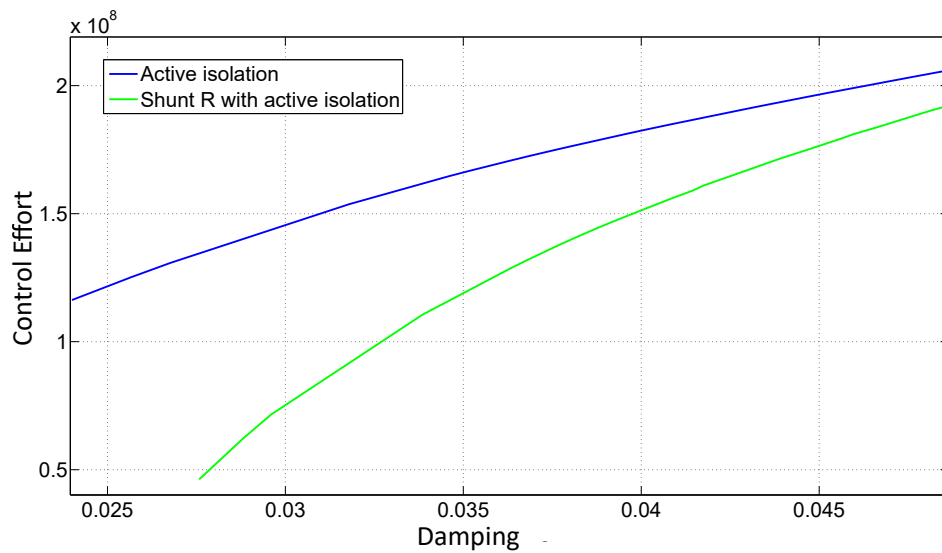


Figure 3.25: Relationship between damping and control effort (F_s/w in N/m) for varying the stiffness ratios. Second mode

strategy due to a lower control effort requirement and a higher performance. From this algorithm, one can target a certain level of damping and obtain the control effort that will result. Inversely, it is possible to set a maximum level for the control effort and then obtain the damping that will result from this.

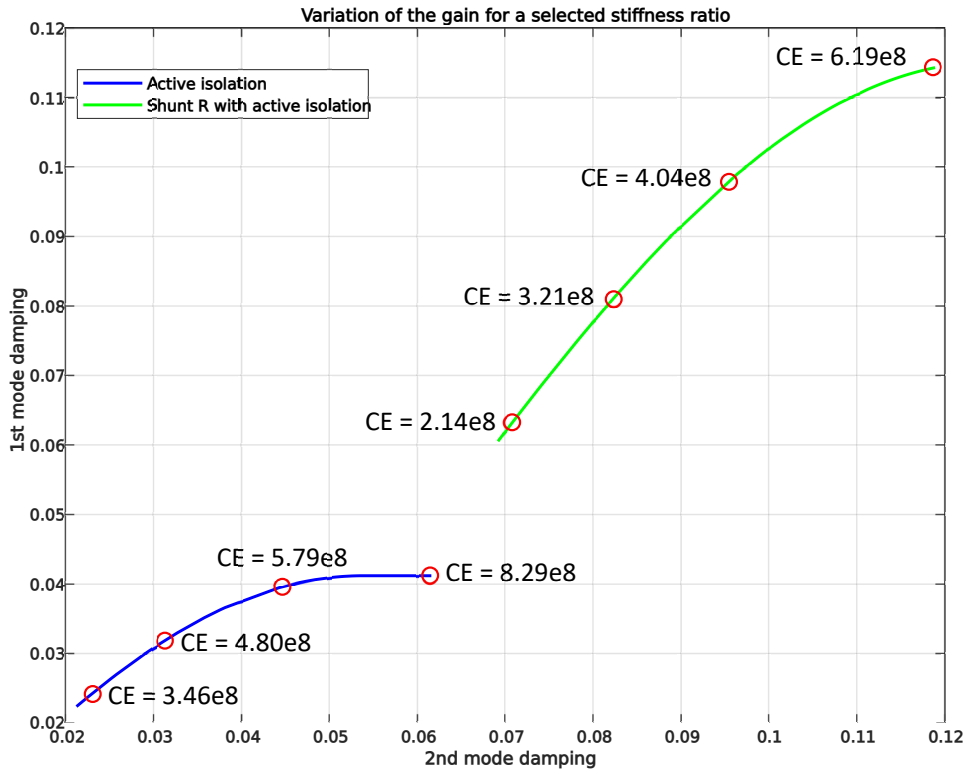


Figure 3.26: Damping of the first mode as a function of the second mode, for different control effort ($CE = F_s/w$ in N/m)

3.2.4 Summary

This section presented the groundwork for the development of a hybrid isolator to be used in space applications. An initial approach to introducing a shunting mechanism into the system has been made, where the piezoelectric stack used as a sensor is connected in series with a resistance, and although the resulting output from the sensor is not representative of the force at its location, it shows the potential of the shunting mechanism.

To successfully include a shunt into the active isolator, a third piezoelectric stack is needed, exclusively dedicated to performing passive isolation. After studying the possible architectures to include the third stack into the system, it has been

demonstrated that the best approach is to place the collocated sensor and actuator stacks (both in series with respect to one another) in parallel to the shunted stack.

Once the structure of the isolator is set, the focus is shifted towards developing algorithms to optimize its performance, which are shown in Section 3.2.3 of this chapter.

Active isolation raises concerns related to the power consumption of the system. From the studies presented in this chapter, it can be concluded that a hybrid isolator composed of the previous active system, combined with a shunted piezoelectric stack, is able to reduce the power consumption of the system, reducing the weight penalty of having an active strategy. Furthermore, by adding a shunted stack, the passive performance of the system is improved while increasing the passive stiffness of the system. This can be regarded as incorporating a fail-safe mode into the isolating system in case there is a failure of the active components, where the decrease in performance is limited, and minimum stiffness levels are guaranteed.

The isolator architecture presented has potential applications both for payload comfort and micro-vibration isolation. The advantages of using such a system include the ability to achieve broadband isolation, and a reduction of the power consumption when compared to purely active systems achieving equal performance and small volume.

A potential drawback of this system is its limited stroke due to the nature of the piezoelectric stacks, which even when mechanically amplified is very limited. In order to accommodate for the large displacements seen during launch, when using piezoelectric actuators, a redesign of the stacks and their amplification structure is needed.

Chapter 4

Active Isolator for micro-vibrations

Contents

4.1	Motivation	59
4.2	Isolator Design	60
4.2.1	Brief description of the isolator	60
4.2.2	Struts	61
4.2.3	Supporting springs	63
4.2.4	Active control	70
4.3	Isolator Performance	76
4.3.1	Single DOF Experimental Characterization	76
4.3.2	Multi-DOF Experimental Characterization	80
4.3.3	Supplementary Tests	92
4.4	Payload Comfort Operating Mode	98
4.5	Conclusions	102

Whether it is a space-borne communication system requiring high pointing accuracy to be able to transmit data, a telescope needing to remain steady during the exposure time of its detectors to avoid blurring and jitter, or the need to avoid disturbing on-board sensors for the correct operation of instruments, sensitive payloads aboard satellites require a quiet environment in order to operate correctly. Current satellites often carry a set of equipment required for their correct operation like reaction wheels, cryocoolers, and positioning mechanisms which introduce mechanical disturbances into a satellite upon becoming operational which can become a source of disturbance [12, 26, 66–68].

This chapter summarizes the development and testing of a multi-DOF active isolator platform for micro-vibrations and is organized as follows:

- Section 4.1 justifies the need for such isolating platforms
- Section 4.2 describes the requirements specified to the platform and the design choices driven by them
- Section 4.3 shows the results from the experimental validation carried out with both a dummy and a real payload, along with the assessment of the performances achieved
- Section 4.4 Presents the simulations on the effect of subjecting the isolator to a typical launch mechanical environment
- Section 4.5 sums up the results and discusses potential future developments for the platform concept

4.1 Motivation

Reaction wheels in particular have been targeted with the isolator described in this chapter due to their widespread use, their continuous operation on a flying spacecraft, and the broadband nature of the disturbances they inject [27, 28].

Both passive [9, 34, 35, 37, 43] and active [69–72] concepts for micro-vibration isolators have been described in literature. While typically tackling the reduction in the transmitted vibrations up to 50 Hz with success, they suffer from degraded performance at higher frequency, which is mainly due to their complex mechanical design, with local deformation modes introducing spurious resonances into the system. On the passive side, reaction wheels are commonly integrated into the satellite using a set of elastomer-based elements. This has the advantage of reducing amplifications at resonances. However, as seen in Section 2.2.1 this same damping can also be detrimental to the mechanical isolation achievable at high frequencies.

The objective in the development of the active platform presented in this chapter is to isolate the satellite from reaction wheel-borne micro-vibrations in a wide frequency range. The active platform presents a high isolation factor due to its low resonance frequency and absence of local deformation modes until 500 Hz, reaching 65 dB of reduction in the transmitted forces at 300 Hz. Active control is used to damp the main suspension modes, reducing the amplification at their corresponding frequencies.

4.2 Isolator Design

Reaction wheels inject micro-vibrations in six degrees of freedom. These disturbances are characterized by being broadband and of moderate magnitude, but sufficient to disturb the scientific observations. These disturbances originate from unbalances in the rotor assembly, irregularities in the bearing system (geometric imperfections in the ball bearings and side effects of insufficient or inadequate lubrication being the main contributors), and from the topology of the rotor-stator assembly in brushless DC motors, causing a torque ripple when being driven [73–75].

On the other hand, an extensively applied approach to manage disturbances in six DOF is the Stewart-Gough platform [38, 41, 42, 47]. These platforms consist of two plates interconnected by six struts. Through independent actuation of the struts, it is possible to have authority over all six degrees of freedom.

The performance of a given isolation system is dependent on the characteristics of the roll-off of the transmissibility after the system's resonance. The main factors affecting this roll-off are: its starting point, given by the resonance frequency of the system, its slope, dependent on the damping of the system where lower damping results in a steeper slope, and the appearance of spurious resonances rising from local deformation modes in the transmission path of the disturbances. To maximize the isolation performance of a system it is therefore important for it to have a low resonance frequency, low damping, and no spurious resonances in the frequency band of interest for the isolation. However, a low value of damping required to preserve the high-frequency isolation results in a high amplification of the disturbances occurring at the resonance frequency of the isolator. To tackle this issue, active control, in the form of relative velocity feedback, is applied at frequencies around the suspension resonance.

4.2.1 Brief description of the isolator

The isolator consists of two plates, one interfacing the reaction wheel (source plate) and another one interfacing the satellite (base plate). These two plates are connected by six struts in a Stewart platform configuration. To avoid the rise of spurious resonances coming from complex structures like joints and guiding mechanisms in the struts, frameless voice coil actuators are installed in each strut. By removing this mechanical connection, the struts no longer support the mass of the payload. It is therefore necessary to include a series of structural supports between the two plates of the isolator. To do this, a set of six springs, distributed symmetrically in pairs around the platform has been designed. The resonance frequency of the suspended

system has been targeted at 5 Hz since it is an early starting point for the isolation, but not low enough to interfere with the guidance navigation and control systems of the spacecraft. The isolator is depicted in Fig. 4.1.

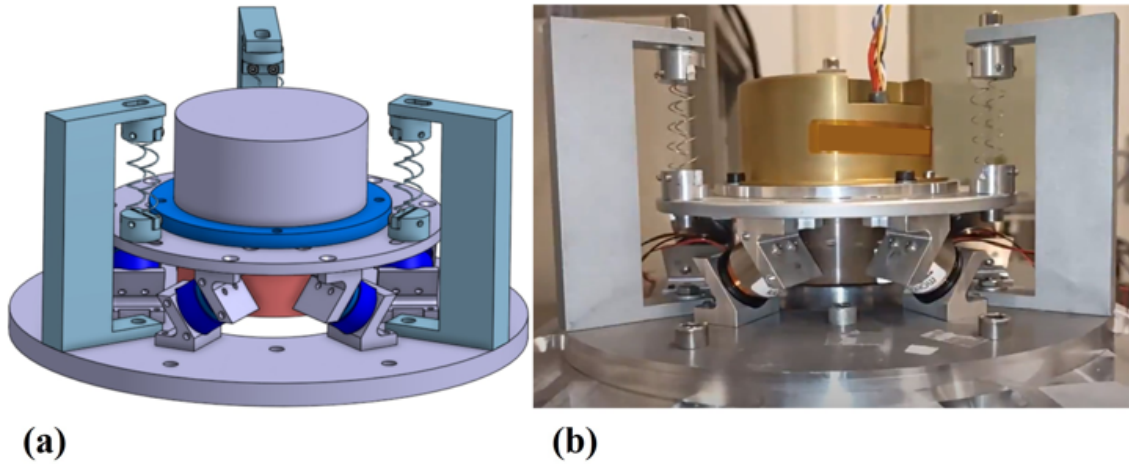


Figure 4.1: (a) 3D model of the isolator with the actuators highlighted in dark blue; (b) isolator with reaction wheel in operating conditions

For this prototype, aluminum has been selected as the main material, since it allows to meet the above requirements, presents easy machinability, and has a strong aerospace heritage. Practical implementations in the further development of this system could benefit from investigating the use of carbon fiber reinforced polymer as the main structural material in order to make it more mass efficient.

4.2.2 Struts

There are two key aspects to the design of the struts: the first one is the disposition of each strut with respect to the payload and base plates, and the second one is the mechanical connections in the struts.

For this application, a cubic configuration of the struts is selected. This layout presents several advantages when performing active control which have been covered in literature, among which are: uniformity of control capability in all directions and minimum cross-coupling among actuators [76]. To obtain a cubic configuration, two parallel planes are sliced from a cube as shown in Fig. 4.2 each one representing one plate of the platform, where the lines marked by L form the struts.

As discussed in Section 2.5 the kinematic relationship J between the motion in the direction of each strut q and the motion of the center of mass of the top plate X is

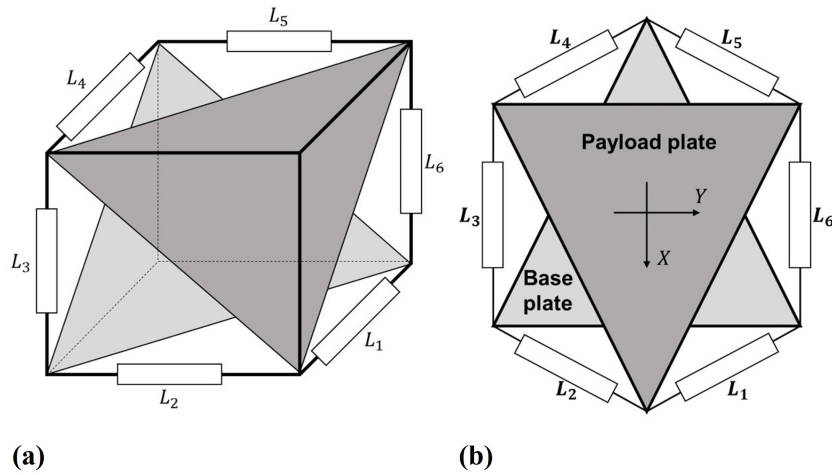


Figure 4.2: Schematic views of the cubic configuration of a Stewart platform. (a) Isometric view; (b) top view

$$q = JX \tag{4.1}$$

In the specific case of a cubic configuration, J takes the form

$$J = \begin{bmatrix} 1 & 1 & 1 & 0 & -L\sqrt{2} & L \\ \frac{1}{\sqrt{6}} & \frac{1}{\sqrt{2}} & \frac{1}{\sqrt{6}} & 0 & \frac{3}{L} & \frac{\sqrt{3}}{L} \\ 1 & -1 & 1 & 0 & -L\sqrt{2} & -L \\ \frac{1}{\sqrt{6}} & \frac{1}{\sqrt{2}} & \frac{1}{\sqrt{6}} & 0 & \frac{3}{L} & \frac{\sqrt{3}}{L} \\ -2 & 0 & 1 & L & \frac{L}{L} & \frac{L}{L} \\ \frac{1}{\sqrt{6}} & 0 & \frac{1}{\sqrt{6}} & \frac{\sqrt{6}}{L} & \frac{\sqrt{6}}{L} & \frac{\sqrt{3}}{L} \\ 1 & 1 & 1 & \frac{1}{L} & \frac{1}{L} & -L \\ \frac{1}{\sqrt{6}} & \frac{1}{\sqrt{2}} & \frac{1}{\sqrt{6}} & \frac{\sqrt{6}}{L} & \frac{\sqrt{6}}{L} & \frac{\sqrt{3}}{L} \\ 1 & -1 & 1 & -\frac{1}{L}\sqrt{6} & \frac{1}{L} & \frac{1}{L} \\ \frac{1}{\sqrt{6}} & \frac{1}{\sqrt{2}} & \frac{1}{\sqrt{6}} & \frac{1}{L}\sqrt{6} & \frac{1}{L} & \frac{\sqrt{3}}{L} \\ -2 & 0 & 1 & -L & \frac{L}{L} & -L \\ \frac{1}{\sqrt{6}} & 0 & \frac{1}{\sqrt{6}} & \frac{1}{\sqrt{6}} & \frac{1}{\sqrt{6}} & \frac{\sqrt{3}}{L} \end{bmatrix} \tag{4.2}$$

Figure 4.3 shows example diagrams of a guided voice coil actuator with a flexure and a frameless voice coil. In guided actuators, the guiding flexure mechanically links the stationary and moving sections of the actuator, becoming part of the transmission path of disturbances. These flexures are typically made of thin, slotted metal plates which ensure a co-linear displacement between the magnet and the coil. Made to be compliant, the stiffness in these flexures is low, and therefore present local deformation modes at low frequency that give rise to secondary resonances in the transmission path, degrading the isolation. For this reason, frameless voice coil actuators have been chosen, eliminating any mechanical connection in the actuators and facilitating the design of a clean transmission path for the disturbances. The

selected voice coils also present a larger clearance than is typical for their size to accommodate the relative motion of the platform in all six degrees of freedom.

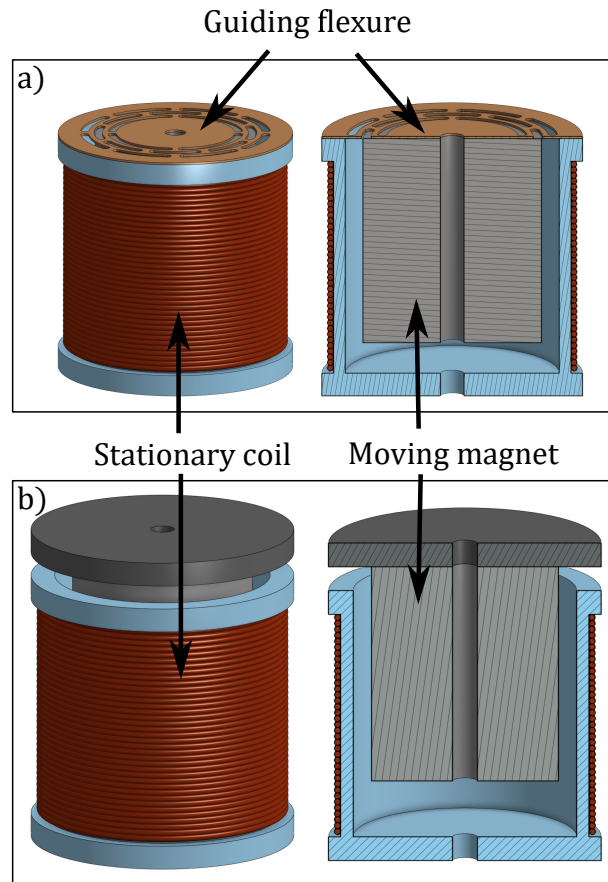


Figure 4.3: Full view and cross-section of example models of a) a guided voice coil actuator, where the flexure ensures the co-linear motion between the magnet and the coil; b) a frameless voice coil actuator without a guiding system as implemented in the concept described in this article.

The actuator supports have been designed to be able to accommodate the voice coils, while having space for sensors to be placed co-axially on the opposite face for monitoring purposes. The same support has been designed for all actuators to ensure the platform’s symmetry. A depiction of the actuator supports is found in Fig. 4.4.

4.2.3 Supporting springs

The lack of a mechanical connection in the struts raises the need to include additional supports in the platform. To this end, three sets of springs are symmetrically distributed around the platform as shown in Fig. 4.5.

The spring’s characteristics, material, number of turns, spring wire diameter, and spring diameter have been specifically chosen for two purposes. The first one

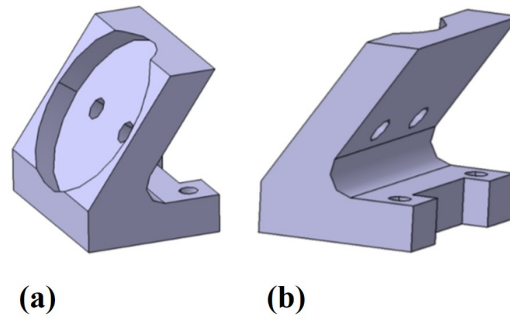


Figure 4.4: CAD view of actuator support. (a) Front view; (b) rear view

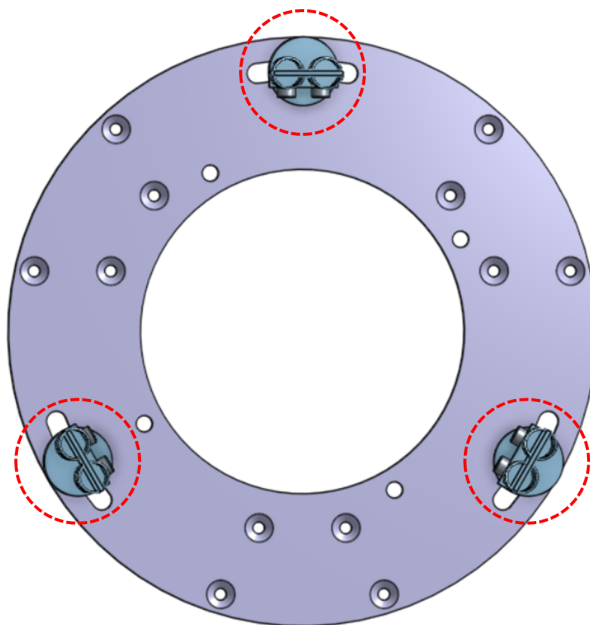


Figure 4.5: CAD view of source plate indicating the spring locations.

is to provide the required stiffness of 160 N/m in each spring to, together with the suspended mass, result in an overall suspension resonance of 5 Hz. The second one is to not present local deformation modes (internal resonances in the spring where the coils deform independently) below 500 Hz. In order to converge towards a design fulfilling the requirements, the spring's stiffness can be approximated by treating it as a cylindrical rod and calculating its stiffness and first resonance frequency. This results in Eq's (4.3,4.4) [77]. Where k is the spring stiffness and f_{res} is the spring's first resonance frequency, G is the material's shear modulus, ρ is the density of the material, d is the spring wire diameter, D is the spring diameter and N_a is the number of turns in the spring.

$$k = \frac{Gd^4}{8D^3N_a} \quad (4.3)$$

$$f_{res} = \frac{d}{2\pi D^2 N_a} \sqrt{\frac{G}{2\rho}} \quad (4.4)$$

The values chosen for the above variables in order to fulfill the stiffness and internal resonance conditions are presented in Table 4.1. The dynamic behaviour of a spring working in the linear regime is the same, independent of if it is working in tension or in compression. Mounting the springs in tension instead of in compression avoids buckling, and carries the added benefit of not having the design of the springs constrained by the available space between the two plates.

Table 4.1: *Parameters chosen for the design of the springs in spring steel EN-10270-3 Type 302.*

Material Properties	
Shear modulus (G), GPa	73
Density (ρ), kg/m ³	7920
Geometric Properties	
Spring diameter (D), mm	7.2
Number of turns (N_a)	4
Spring wire diameter (d)	0.4

In order to mount the springs in tension, an aluminum bracket has been designed with no local modes under 500 Hz onto which the spring clamps can be attached. A finite element of the bracket was created and run in *Abaqus* (Fig. 4.6). The finite element analysis shows that the first mode of the bracket is at 1395 Hz. The spring clamps are made such that the spacing between the bracket and the clamp can be modified, enabling fine-tuning of the vertical, static position of the platform. The horizontal position of the springs can be adjusted by changing their mounting

Isolator Design

position on the slots located in the source plate, as seen in Fig. 4.5. This is interesting to be able to adapt the isolation platform to payloads with different COM and to compensate for inaccuracies in the manufacturing and assembly of the different parts.

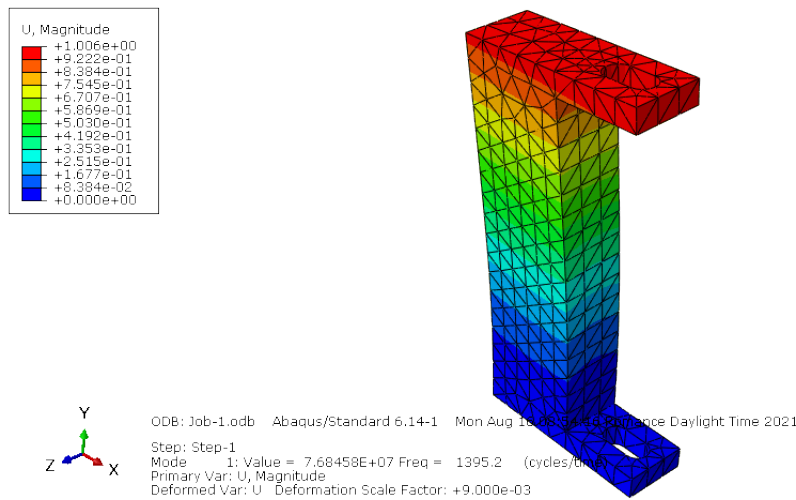


Figure 4.6: FEA of the brackets suspending the top plate showing the first local deformation mode at 1395 Hz.

The on-ground testing configuration consists of two springs per spring clamp per bracket, symmetrically spaced around the platform. This is the configuration that has been tested and will be showcased in this document. However, once the payload enters a zero-g environment, the weight of the platform will no longer be affecting the springs and the static position of the source plate will change. This has been accounted for and can be mitigated by switching one of the springs in each pair from connecting the source plate to the brackets, to connecting the source plate to the base plate, as shown in Fig. 4.7d. This way, the tension forces in the springs are compensated, and the source plate remains in its optimal position.

The performance of each spring pair has been individually evaluated before mounting on the platform. Each spring has been tested as an assembly consisting of two springs in parallel held by one spring clamp at each end. Two different setups have been used.

The goal of the first setup is to verify the stiffness of the three spring assemblies, represented by k_1 , k_2 and k_3 . The setup consists of a static force sensor attached to one end of each spring assembly and a translation stage attached to the other. Starting from the spring's natural length of 19 mm, a set deformation is introduced in each spring assembly (steps of 1 mm were used). The corresponding force is measured and logged by the force sensor directly connected to a PC, allowing for an accurate calculation of the stiffness of the spring assembly throughout the range of

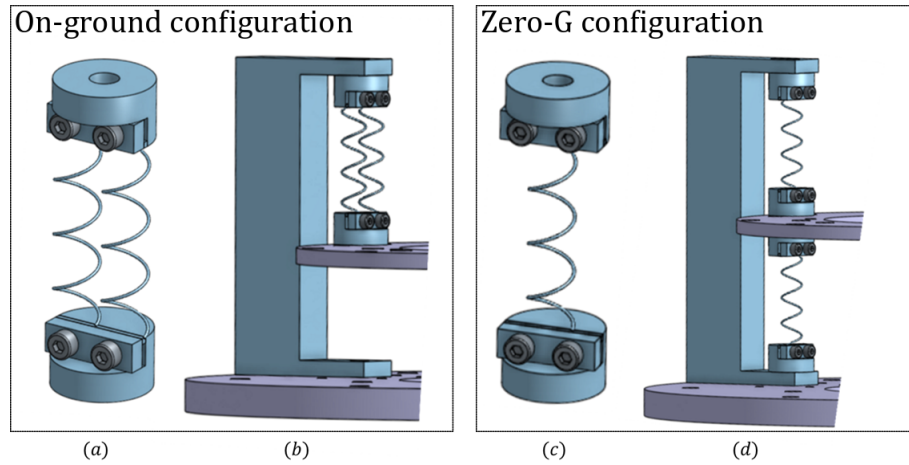


Figure 4.7: CAD view of different suspension system configurations. (a-b) On-ground clamp system and mounting configuration; (c-d) zero-g clamp system and mounting configuration

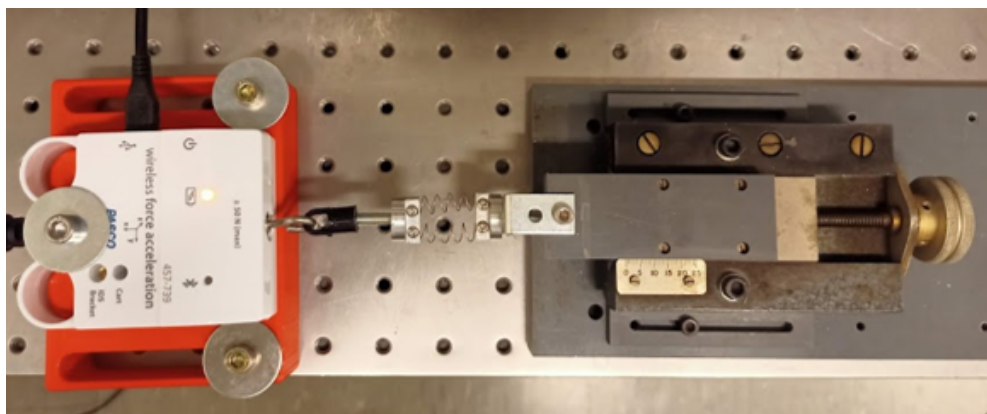


Figure 4.8: Test setup to evaluate the spring's stiffness. Left to right: clamped static force sensor, spring assembly, horizontal translation stage.

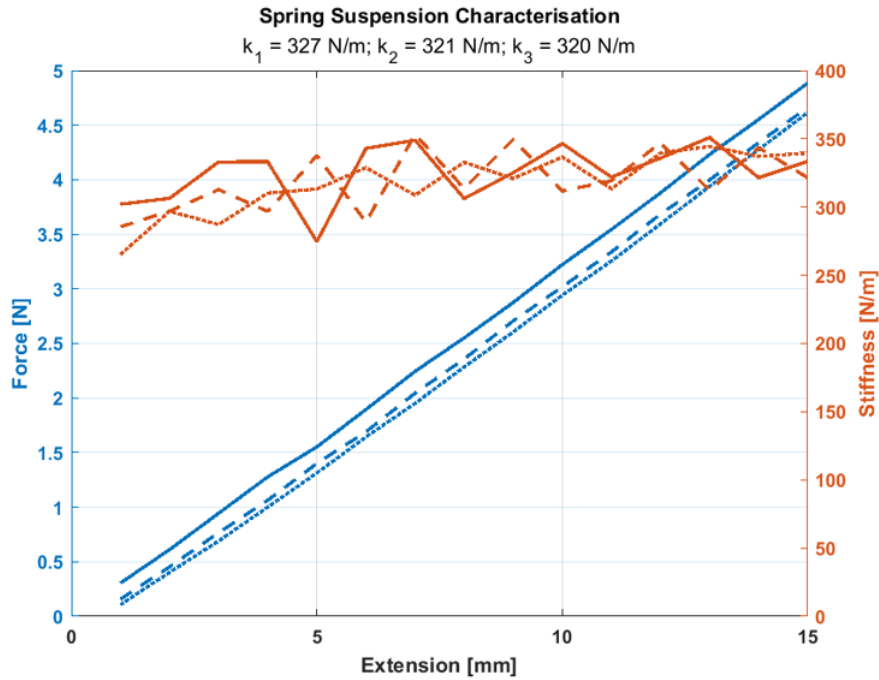


Figure 4.9: Force (blue) and stiffness (red) of each spring assembly consisting of two springs in parallel as a function of the induced extension. The average stiffness for each spring assembly can be found in the subtitle. The natural length of the springs is 19 mm

deformation of its constituting springs. Fig. 4.8 shows a picture of this setup.

Fig. 4.9 shows that the behavior of the springs is linear in the tested regime, and the stiffness of each spring assembly is very close, with a maximum difference of 7 N/m found between k_1 and k_3 . These results correspond well with the simulations done during the design phase of each individual spring, where a stiffness of 160 N/m per spring was targeted, resulting in 320 N/m for each assembly of two springs in parallel.

The goal of the second setup was to check for local deformation modes in each spring assembly at undesirable frequencies. Force sensors are connected to each end of the spring assembly, where one is fixed and the other one is attached to an electrodynamic shaker (The Modal Shop K2004E01). This arrangement allows the introduction of a broadband disturbance in the system, exciting any resonances present in the frequency range of interest that will appear in the transfer function between the measurements of the two force sensors. Fig. 4.10 shows a picture of this setup.

The results obtained from the setup in Fig. 4.10 are shown in Fig. 4.11. A resonance can be seen at low frequency corresponding to the moving mass of the shaker, followed by a -40 dB/dec roll-off, with the resonances of the test setup

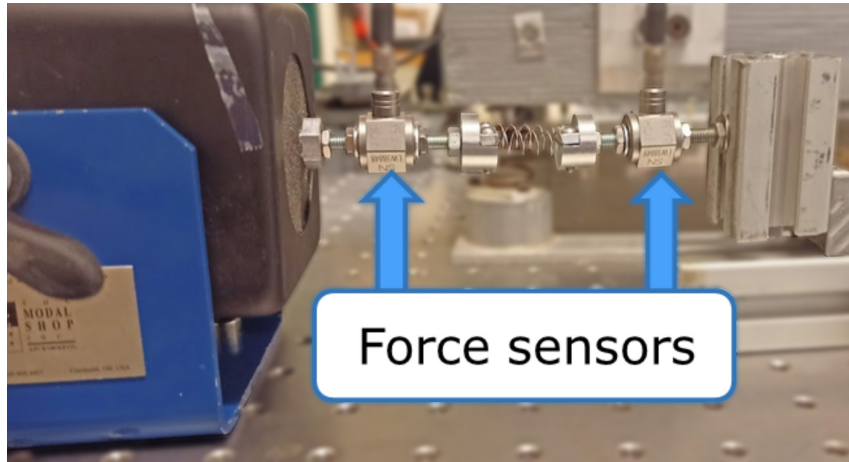


Figure 4.10: Test setup to evaluate the dynamics of each spring assembly. From left to right: electrodynamic shaker, piezoelectric force sensor, spring assembly, piezoelectric force sensor, blocked end.

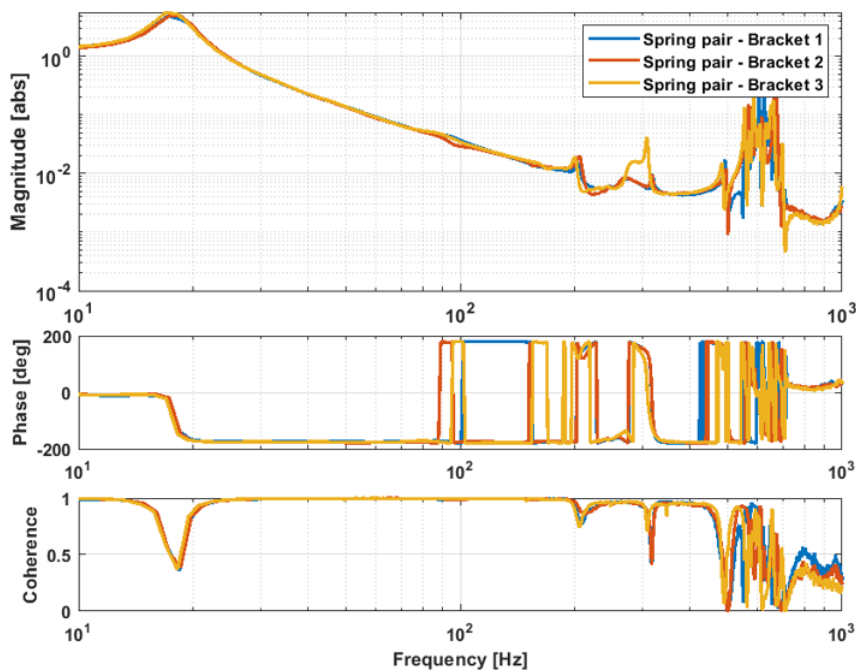


Figure 4.11: Force transmissibility, phase, and coherence for each spring assembly pair. A resonance can be seen at low frequency corresponding to the moving mass of the shaker, followed by a -40 dB/dec roll-off, with resonances of the test setup appearing at 200 Hz and 315 Hz. The local deformation modes of the springs can be seen between 500 - 700 Hz.

appearing at 200 and 315 Hz. The behavior of each spring pair is identical except for the spring assembly "Spring pair - Bracket 3" in the frequency band of 280 - 300 Hz, where a minor difference in mounting has been identified as the cause. The resonances shown at 200 and 315 Hz originate in the shaker, whereas the resonances shown in the frequency range of 500 - 700 Hz are a combination of the internal resonances of the springs and the resonances of the setup.

4.2.4 Active control

To avoid the magnification of disturbances at the resonance frequencies of the isolator, active control is used. The relative velocity between the source and base plates in the axis of each actuator is used as an input for the controller. The voltage drop V_m across the terminals of a voice coil actuator is related to the current i moving through it, and the relative velocity v between the actuator's stationary and moving sections [78] through the following equation:

$$V_m = Ri + L\frac{di}{dt} + T_{em}v \quad (4.5)$$

where T_{em} is the electromechanical coupling coefficient, and R and L are the coil's resistance and inductance. This equation can be rearranged to show how to obtain the relative velocity from the actuator's properties and the measured voltage drop and current:

$$v = \frac{V_m - Ri - L\frac{di}{dt}}{T_{em}} \quad (4.6)$$

Computing the relative velocity from Eq. (4.6) enables using the voice coils as both actuators and sensors. There are several advantages of using the actuators in self-sensing mode. Each sensor-actuator pair is collocated, ensuring stability through alternating poles and zeros in the open loop transfer function [79] and is observed in the experimental transfer function in Fig. 4.15. The phase shift caused by each pole is compensated by the following zero, avoiding phase cumulations and locking the phase between -180° and 180° , thus ensuring the stability of the system. The overall weight, complexity, power draw, and possible failure points of the system are reduced by removing additional sensors [80]. A transmission path for disturbances between the source plate and the base plate is removed by eliminating the cable that would be connected to any sensor placed on the source plate.

The test setup in Fig. 4.12 was built to verify the performance and accuracy of

the self-sensing technique. A beam is clamped at one end, with its other end left free. A voice coil is attached to the free end of the beam to estimate the velocity of the beam tip. This voice coil is the same model as the ones included in the isolation platform. A Polytec laser vibrometer is pointed at the opposite face of the beam at the location of the center point of the voice coil. This sensor is used as a reference to evaluate the estimated velocity signal from the self-sensing voice coil.

Table 4.2: *Numeric values from the actuator’s datasheet [10] used to estimate the self-sensed velocity according to Eq. 4.6 for the voice coil shown in Fig. 4.12*

Parameter	Resistance (R), Ω	Inductance (L), mH	EM Coupling Coeff. (T_{em}), V/(m/s)
Value	4.9	0.5	1.6

The voice coil is used to excite the beam while the current through its coil and the voltage across its terminals are monitored. The actuator is driven in current mode with a current injector developed in-house, which is capable of injecting a set current independent of the back-emf of the actuator. A circuit diagram of the current injector is included in Appendix B. The injected current is sampled from the current injector’s monitoring output. The voltage across the terminals of the voice coil is directly measured with a DSpace MicrolabBox system. This allows us to reconstruct the relative velocity between the stationary and moving parts. The values for R , L , and T_{em} used can be found in Table 4.2 and are extracted from the supplier’s data-sheet [10]. The resistance and inductance of the whole electrical path from the measurement point to the voice coil have been verified through an impedance-meter [81] to account for deviations from the set values but were found to be insignificant. The response of both sensors is recorded. Figure 4.13 shows the measurement of the velocity from both sensors as a function of time. The self-sensed velocity matches the reference but presents some high frequency artifacts in its signal. A first-order Butterworth low-pass filter has been applied to the signal from the voice coil to remove the high frequency noise.

Fig. 4.14 shows a block diagram of the control architecture applied to the isolator. The measured voltage and current signals are connected to a DSpace MicrolabBox system where the controller is implemented, and the resulting signal is sent to a current injector feeding the actuators. This system can be implemented on an analogue circuit to reduce its size and weight for its in-flight implementation. Figure 4.14

The open loop transfer function for one of the sensor-actuator pairs (all of them

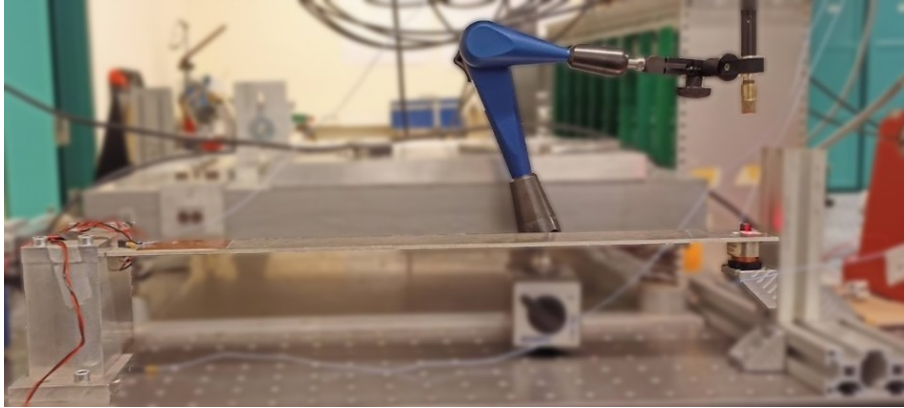


Figure 4.12: *Picture of the setup used to validate the self-sensing technique. A beam clamped at one end is fitted with a voice coil at its free end with a laser vibrometer recording the velocity at the same location. The voice coil serves both as an actuator and as a sensor*

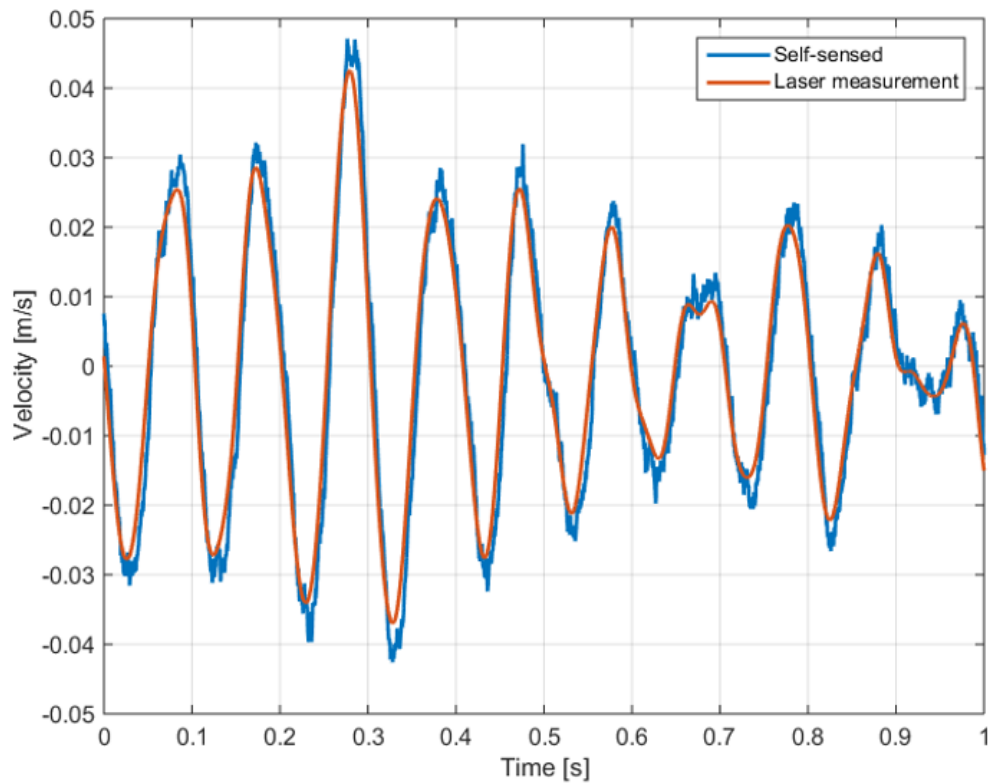


Figure 4.13: *Velocity of the free end of the beam shown in Fig. 4.12 showing a good match between the reference velocity and the self-sensed velocity*

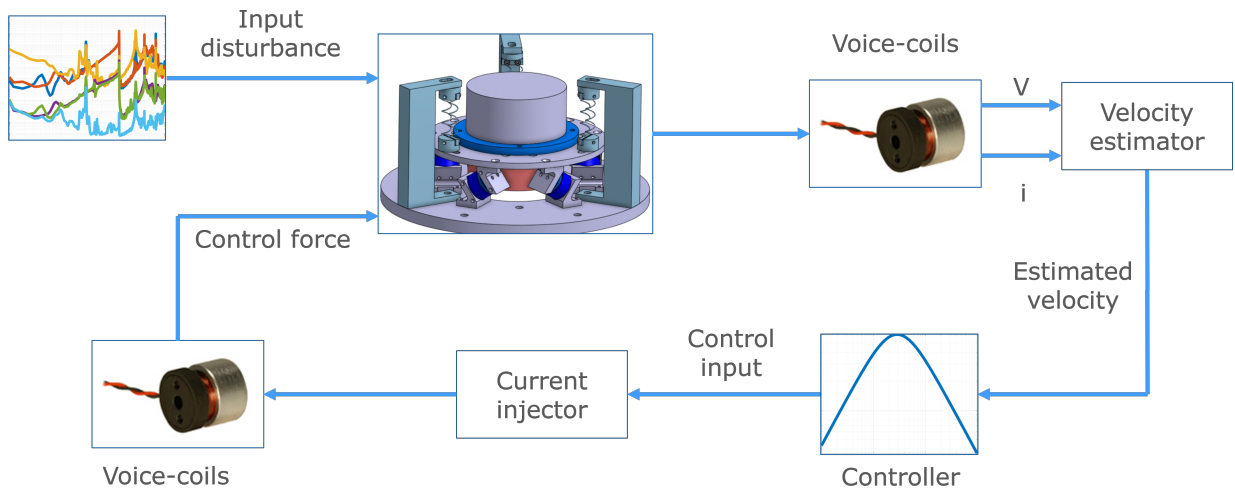


Figure 4.14: Block diagram representation of the active control loop. Note that decentralized control is used, with each voice-coil actuator working independently

are equivalent) can be seen in Fig. 4.15. This curve has been obtained by injecting Gaussian white noise in one voice coil while measuring the relative velocity of the excited voice coil through self-sensing.

The *fitfrd* function from *MATLAB* is used to obtain the model curve. The quality of fit is quantified in terms of mean squared error (MSE), which ranked extremely low compared to the range of fitted values. The mathematical model of the open loop transfer function allows to design a controller, by checking its stability through the loop gain. A negative derivative feedback (NDF) [82] controller is considered for damping the targeted mode of the system. NDF is a band-pass filter, that cuts off the control action far from the natural frequencies associated with the controlled modes, reducing the spillover effect. As a bandpass filter, it can effectively control the lower and higher frequency disturbances. An approach for an optimal design of NDF controller to implement on collocated systems is used [83]. The fitted model is considered and a mode of this system is targeted to damp. The maximum damping method is used to determine the suitable candidates for the controller's constants in order to be dependent based on the closed loop damping parameter. Then, the H_2 method is utilized to select the optimal values among the identified candidates by minimizing the cost function while guaranteeing stability [84]. To this end, as explained in [83], the closed-loop magnitude is selected as the norm to minimize. The results show that NDF can easily damp a targeted mode impactfully. The designed controller is presented in Eq. (4.7), with the corresponding bode plot in Fig. 4.16. Where g is the selected gain. The loop gain for this controller, obtained by multiplying the open loop transfer function and the controller, along with the

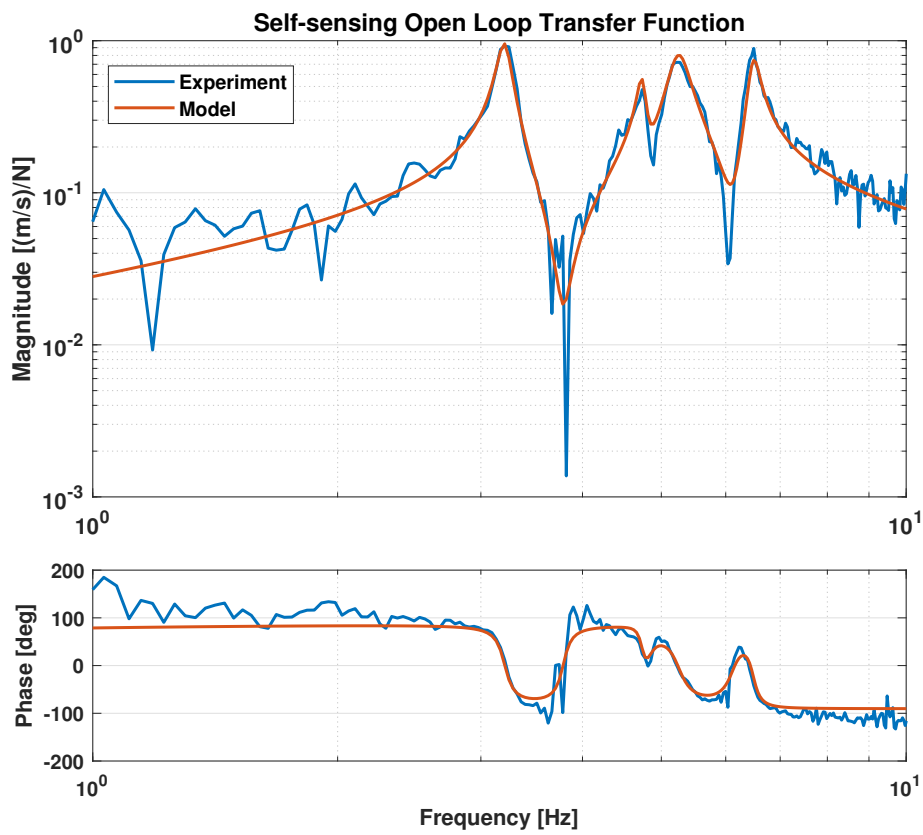


Figure 4.15: Open loop transfer function between the self-sensed velocity and the force injected in one actuator showcasing alternating poles and zeroes

corresponding stability limits are presented in Fig. 4.17.

$$H(s) = g \frac{s}{s + (2\pi * 2.4)} \frac{1}{s + (2\pi * 3.4)} \quad (4.7)$$

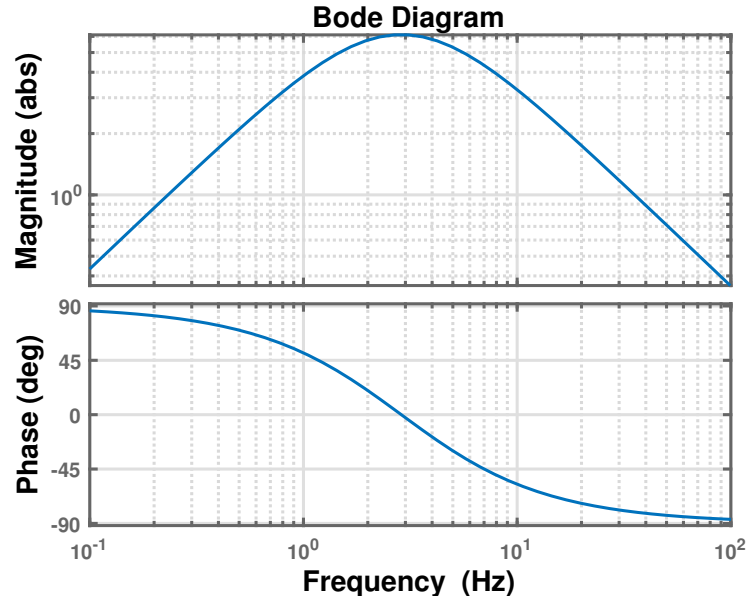


Figure 4.16: Bode plot of the controller used in decentralized loops at each voice-coil actuator

The experimental results obtained with this controller are presented in Section 4.3.1.

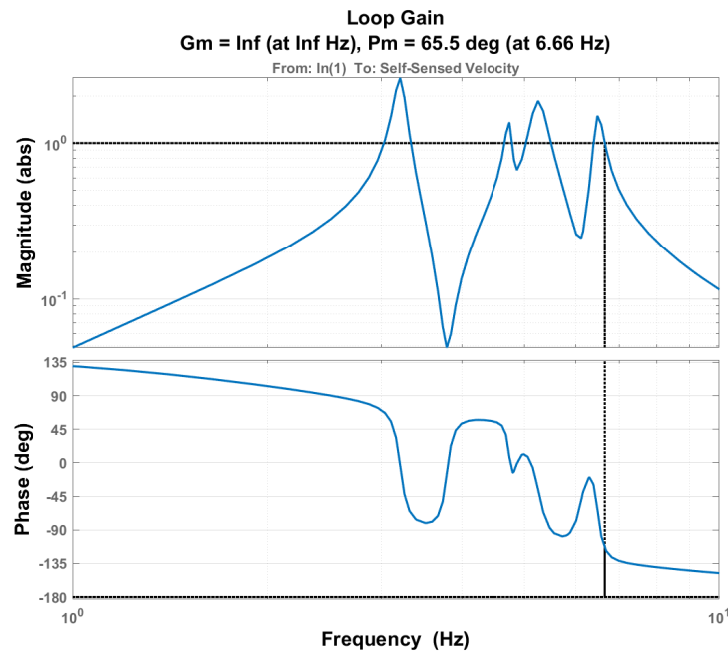


Figure 4.17: Loop gain and stability margins of the system obtained by multiplying the open loop transfer function by the controller

4.3 Isolator Performance

The isolation platform was tested in the axial degree of freedom at the BEAMS laboratory at ULB, which allowed for tuning of the active control parameters. The setup was then moved to the Mechanisms Laboratory at the ESTEC site of the European Space Agency for testing with a test model of a reaction wheel that provided a disturbance in all six degrees of freedom simultaneously.

4.3.1 Single DOF Experimental Characterization

The isolation performance in the axial direction was characterized in terms of the motion transmissibility between the base and source plates. For this purpose, the platform was mounted on an electrodynamic shaker (labeled 1 in Fig. 4.18), and subjected to a broadband base vibration excitation, as illustrated in Fig. 4.18. A dummy representative of the mass and inertia of the test reaction wheel that will be used later was mounted on the top plate (labeled 2 in Fig. 4.18). A bias current was applied to the voice coils to precisely locate the suspended platform at its optimal position where the clearance between the coils and the magnets is maximized.

Two miniature accelerometers [85] were placed at the center of both the source (labeled 3 in Fig. 4.18) and base plates in order to compute the motion transmissibility of the system. Although the performance metric of interest is the force transmissibility,

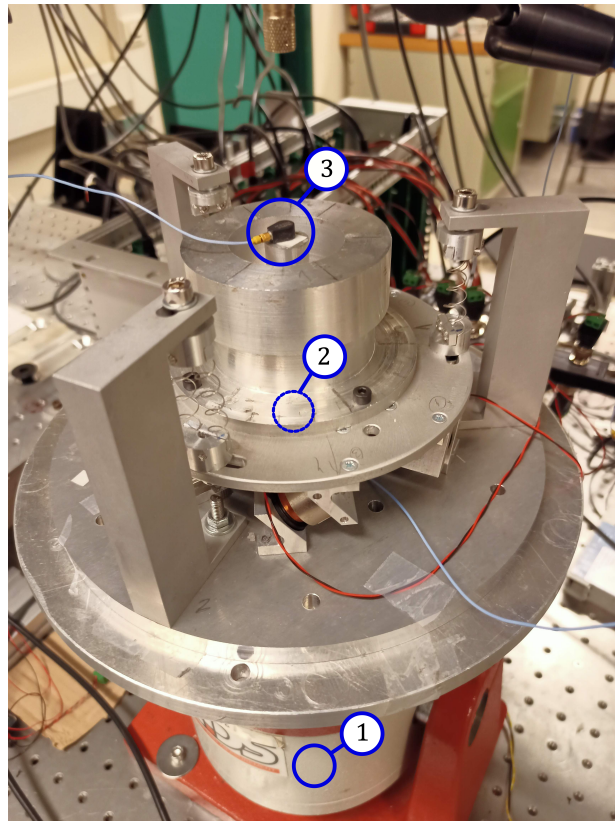


Figure 4.18: *Experimental setup at ULB to verify the platform's passive and active isolation performance. The platform is mounted through an adapter plate on an electrodynamic shaker (1). Two accelerometers are co-axially placed along the center axis of the platform to compute the transmissibility, (2) at the base of the isolator (hidden in the picture) to record the input motion, and (3) on top of the RW dummy to record the output motion.*

Isolator Performance

it can be shown that in systems without active control and in systems with relative velocity control, the motion transmissibility and the force transmissibility of a system are equivalent; analytical proof of this is included in the Appendix. A. The resulting transmissibility can be found in Fig. 4.19.

A reduction of 60 dB in the transmitted motion (equivalent to the force) can be observed at 100 Hz for the active and passive cases. Switching the active control on produces the expected results of successfully damping the resonance, albeit with some loss of isolation in the roll-off region. This degradation of the isolation is due to the increased damping in the system introduced by the active control. The drop in coherence below 5 Hz is due to the limited capability of the shaker to introduce excitations at such a low frequency. In the frequency band of 150 - 300 Hz, due to the high isolation factor of the platform, the disturbances reaching the accelerometer placed on the source plate are smaller than its resolution, leading to the sensor outputting noise. The resulting values seen in this frequency range cannot be regarded as reliable, and further investigation is necessary. However, this drop in coherence implies a performance of the isolation at these frequencies higher than the -60 dB seen at 100 Hz in a scenario of purely axial excitation.

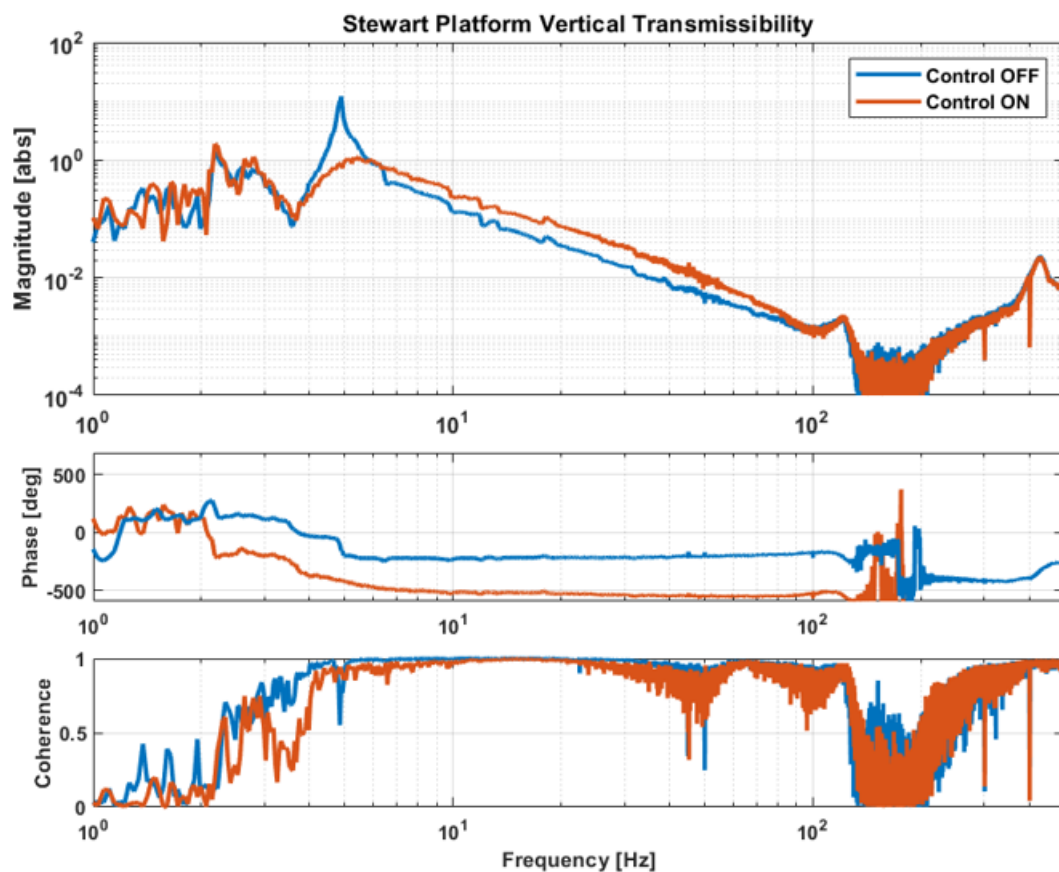


Figure 4.19: *Experimental transmissibility of the isolator in axial direction. The response of the passive system is shown in blue, attaining 60 dB of isolation at 100 Hz, while the response of the active system is shown in red and puts in evidence the damping of the suspension mode*

4.3.2 Multi-DOF Experimental Characterization

After the initial performance verification at ULB, the isolator is moved to the Mechanisms Laboratory at the ESTEC site of the European Space Agency. This allowed installing a functional test model of a reaction wheel on the isolator, which generated disturbances in the six degrees of freedom simultaneously which is representative of the isolating suspension's true operating conditions except for the presence of gravity.

A picture of the test setup is shown in Fig. 4.20. The reaction wheel is mounted on the isolator which is in turn bolted to a dynamometer, attached to the top of an optical table. The dynamometer used is a Kistler 9255A, which consists of two plates interfaced by four tri-axial piezoelectric force sensors at its corners. The outputs of these sensors and the knowledge of the distances between them allow us to reconstruct the disturbing forces and moments generated by the tested sample.

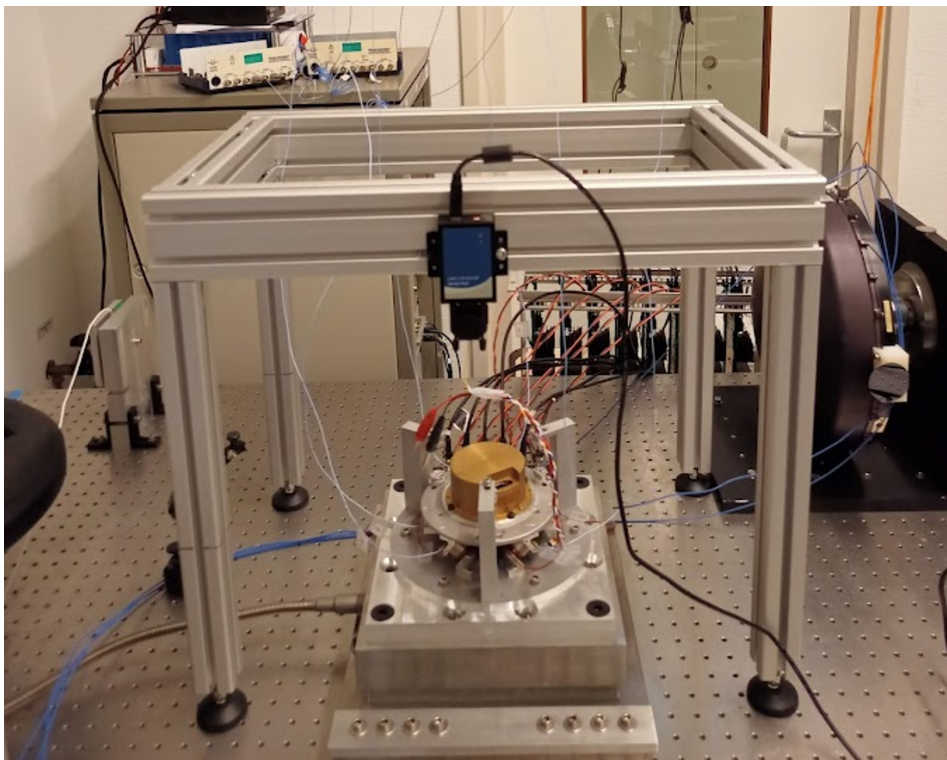


Figure 4.20: *Isolator performance characterization setup showing the cable routing solution. The isolator and reaction wheel are mounted on a dynamometric Kistler table which is bolted on an optical table supported by pneumatic isolators*

Setup characterization

In order to ascertain whether the disturbances measured by the dynamometer are indeed those injected by the reaction wheel, a baseline measurement of the background

noise is performed before running the wheel. During this test, no excitation is purposely injected into the system, giving a readout of the environmental background noise on site. The results are shown in Fig. 4.21. Since the dynamometer is composed of 4 identical sensors, the measurements performed can be used to carry out a huddle test. This type of test is useful to assess the sensitivity of a set of sensors, provided that more than one is available. The sensors are used to simultaneously record a signal, in this case the background noise. The measured signals are then compared allowing us to extract the coherent and incoherent parts of the signal. From the coherent part of the signal, the magnitude (in this case of background noise) can be assessed. The incoherent part of the signals gives us an idea of the noise floor of each individual sensor [86]. The results in the X direction are presented in Fig. 4.22.

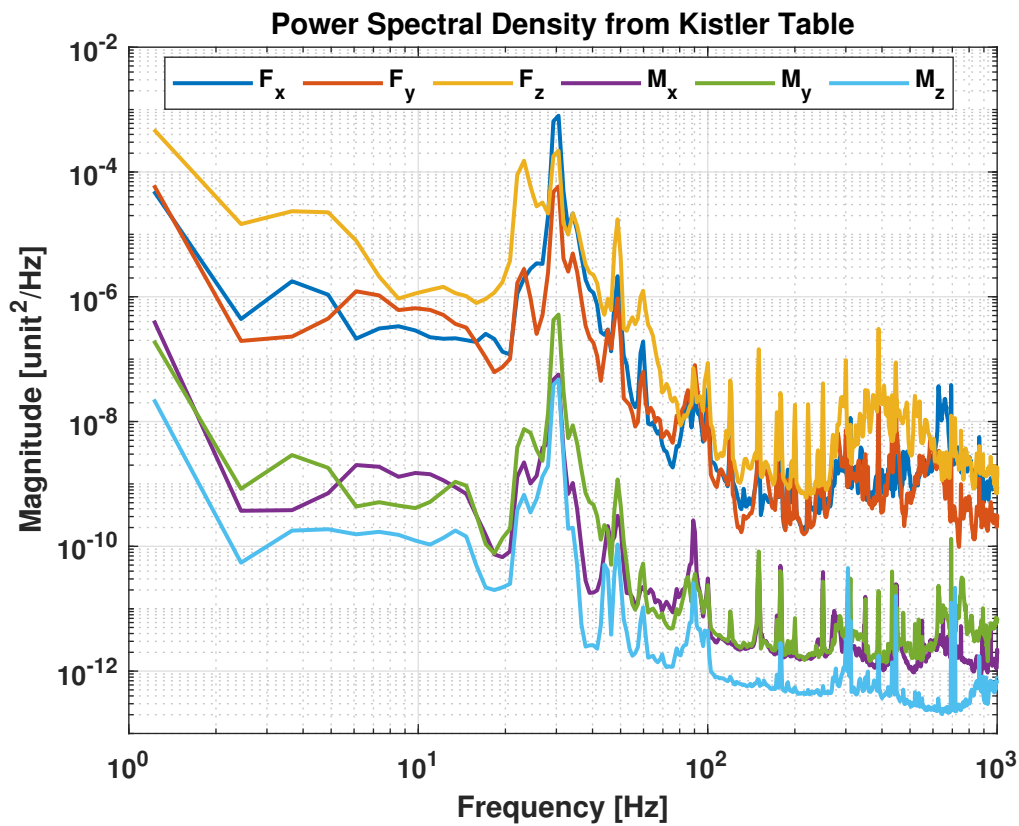


Figure 4.21: Force and torque PSD of the background noise in the experimental room. [unit] corresponds to N for the forces and Nm for the torques. The peaks observed between 20 - 50 Hz correspond to environmental noise and are present in all the measurements

Inspecting the plots in Fig. 4.21 and Fig. 4.22 together, it can be observed that there is a magnification at 5 Hz corresponding to the suspension resonance of the optical table on which the dynamometer is mounted, and disturbances between 20 and 50 Hz which have been linked to sources outside of the experimental room. The sharp peak at 30 Hz for example has been linked to electronics in an adjacent server

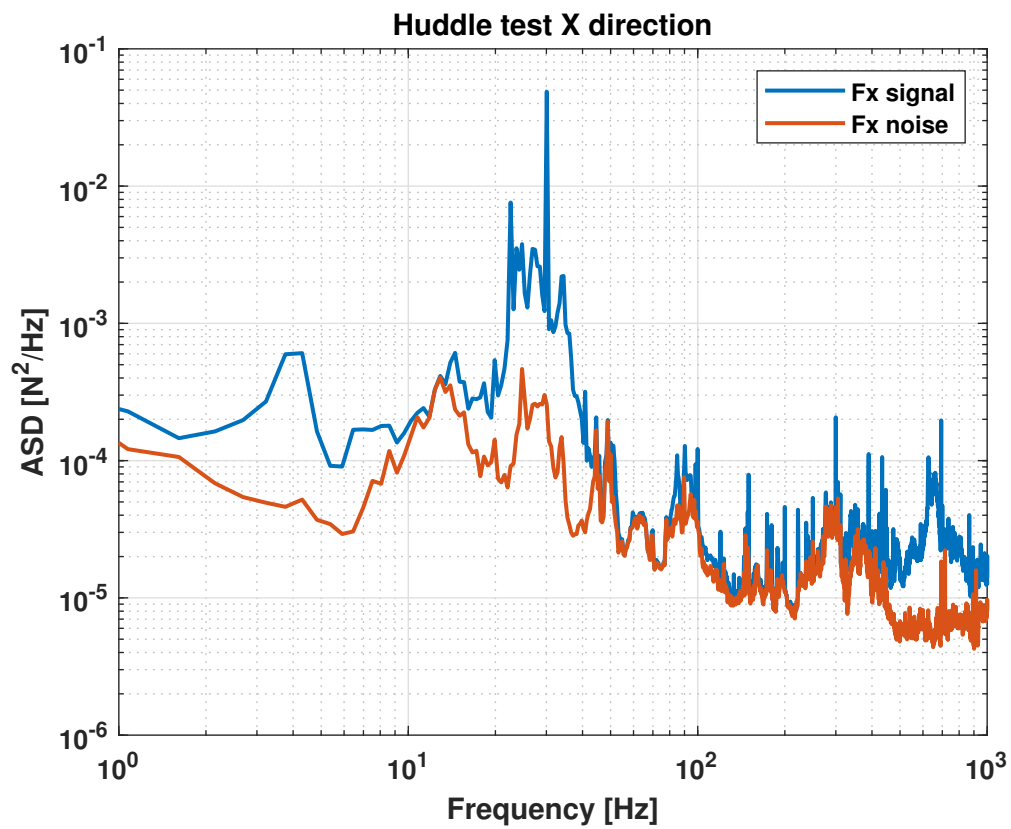


Figure 4.22: *Huddle test results in the X direction, showing the coherent portion of the signal in blue indicating measured quantities, and the incoherent portion of the signal in red giving an indication of the level of the resolution of the sensors*

room.

Another test that is interesting to perform is one that will enable the computation of the transmissibility of the Kistler table. This is done by mounting a shaker with an embedded force sensor (Siemens QSources Miniature Shaker [87]) and injecting Gaussian white noise from 50 - 5000 Hz. The signals from the shaker's embedded sensor and from the sensors in the Kistler table are recorded. This is done in the X, Y, and Z directions. The transmissibility is computed from the recorded signals. The results of these tests are shown in Fig. 4.23, where resonances in the vertical direction appear at 400 Hz, and in the X and Y directions at 560 and 680 Hz respectively. The resonance in the X direction is observable in the huddle test presented in Fig. 4.22. The impact of these resonances on the results is further discussed at the end of Section 4.3.2.

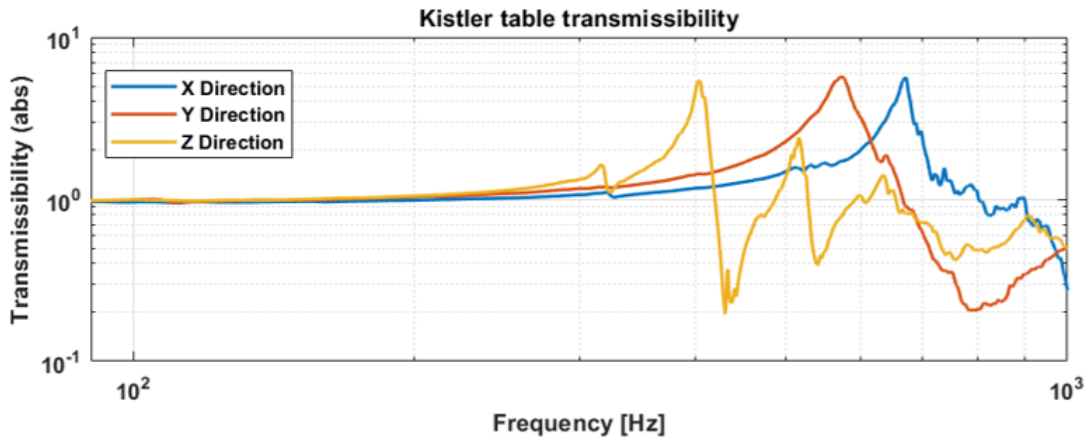


Figure 4.23: Force transmissibility of the Kistler table, showing that they have no impact until 300 Hz on the recorded measurements

Reaction wheel cable impact

The dynamometer is placed on an optical table and the reaction wheel, is attached through an interface plate to the dynamometer. The cables used to command the reaction wheel are carefully routed to avoid impacting the dynamics of the isolator, preventing them from becoming a transmission path of disturbances from the reaction wheel to the dynamometer. The cable routing can be seen in Fig. 4.20. To ensure that the cable bundle has a negligible effect, a series of tests have been carried out.

For the first set of tests, an accelerometer [85] is placed at the center on top of the reaction wheel to measure the vertical motion of the platform. All of the voice coils are excited simultaneously, resulting in a purely vertical excitation of the isolator.

Isolator Performance

The transfer function between the force injected and the measured motion of the platform is shown in Fig. 4.24. It can be observed that except for frequencies below 2 Hz, where the accelerometer is not sensitive enough to measure the motion of the platform, the behavior of the platform is identical with, and without the cable.

In order to further test this hypothesis, one single voice coil is excited, injecting disturbances in multiple directions at the same time. To improve the measurement at low frequency, an opposing voice coil in self-sensing mode is used to measure the motion of the platform. The results are shown in Fig. 4.25. Although there are some minor differences between the curves at 7 Hz, the behavior of the platform is deemed similar enough to proceed with the current cable arrangement.

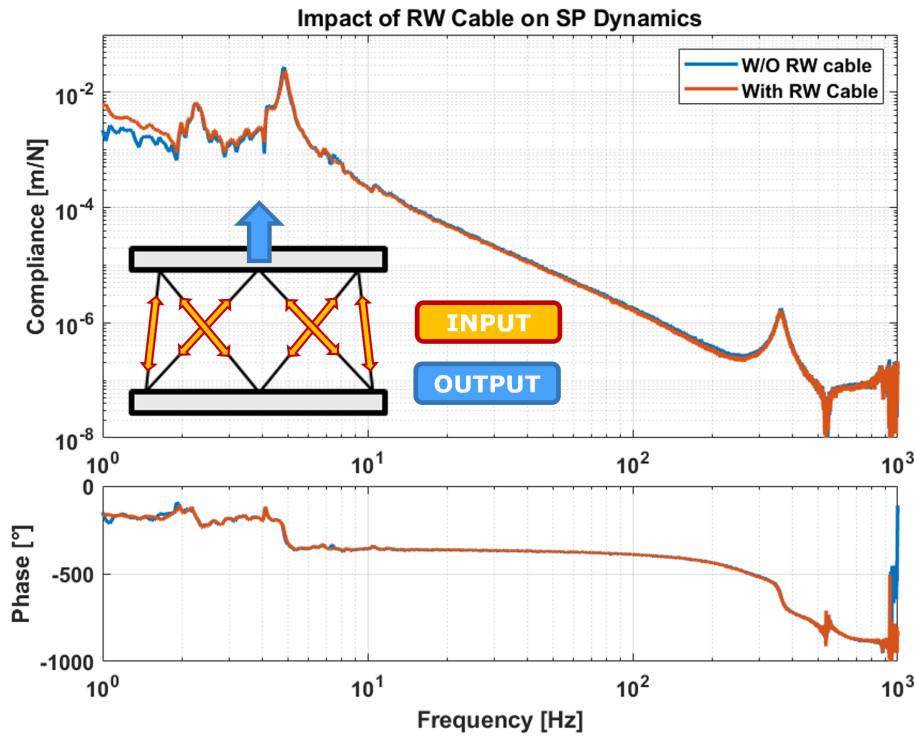


Figure 4.24: Assessment of RW cable impact on the isolator’s dynamics. An equal excitation is injected in every voice coil resulting in a purely vertical excitation which is recorded by an accelerometer on top of the reaction wheel

The final test carried out to evaluate the impact of the cables is to compute the open loop transfer function between the self-sensed velocity, and the force injected in each voice coil. This serves the purpose of assessing the impact of the cable on the control loop and allows for a comparison of the current plant to the plant computed at ULB. The results were identical for the six actuators, for clarity only one of them is shown in Fig. 4.26. Although not completely identical, the results are close enough not to raise the need to modify the controller. It is therefore decided to move forward

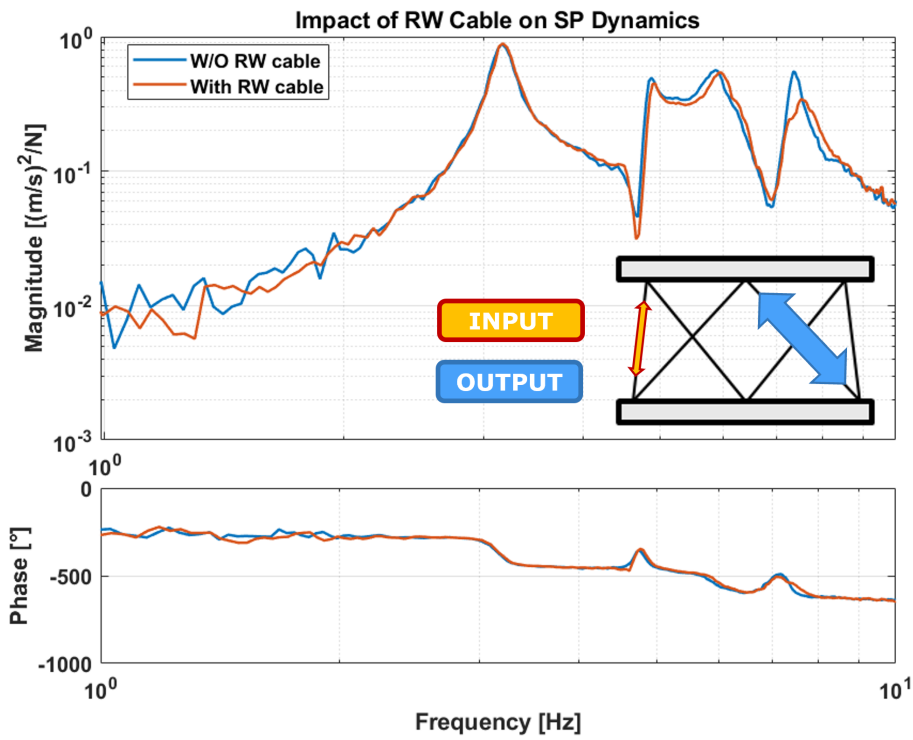


Figure 4.25: Assessment of RW cable impact on the isolator’s dynamics. Multi-directional excitation is created by injecting current in one voice coil and recording the motion with a second coil in self-sensing mode. The vertical axis shows the transfer function between the injected force and the measured relative velocity. The low impact of the reaction wheel cable is observed

with the current cable arrangement and with the active control strategy previously developed.

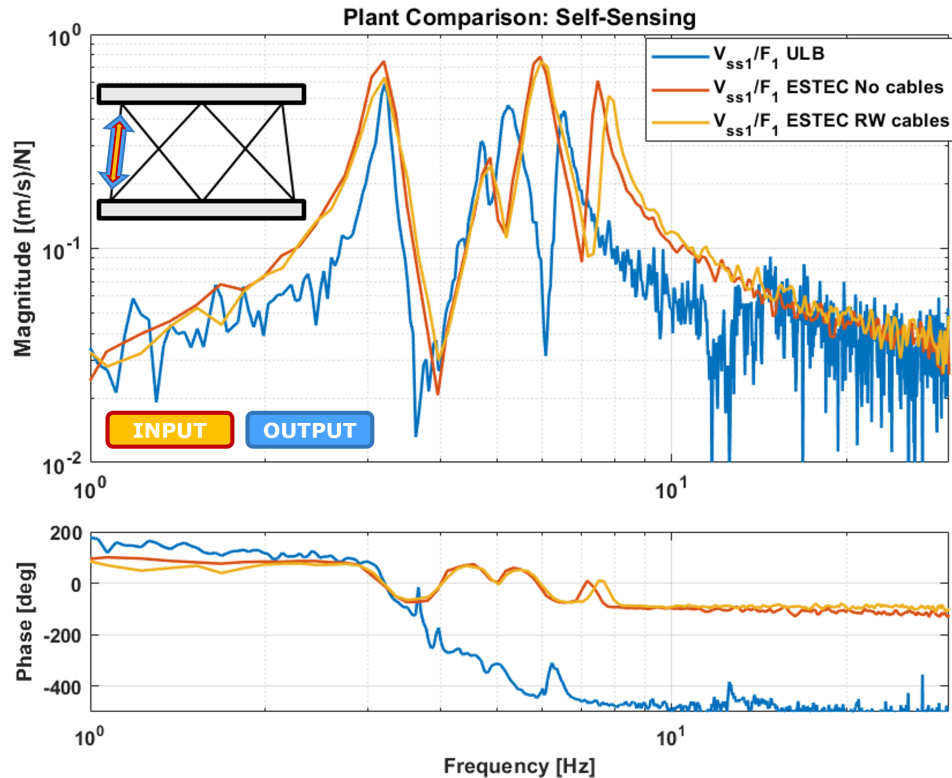


Figure 4.26: *Plant identification showcasing a comparison between the results obtained at ULB (blue) and at ESTEC with (yellow) and without the RW cable (red). Although there are differences in the frequency of two of the poles and zeroes, they are insignificant towards the performance of the active control*

Performance assessment

The assessment of the performance of the isolator platform is carried out by computing the ratio between the force measured by the dynamometer while the reaction wheel is directly hard-mounted on it without the isolator, and the force measured by the dynamometer when the isolator is installed. Fig. 4.30a shows the hard-mounted configuration; with the reaction wheel mounted directly on the dynamometer through an adapter plate. Fig. 4.30b shows the reaction wheel mounted on the isolator, which is interfaced to the dynamometer through its own adapter plate. The measured forces and moments for the corresponding configurations are shown in Fig. 4.27 for the hard-mounted case, and in Fig. 4.28 and Fig. 4.29 for the reaction wheel mounted on the isolator, with and without active control.

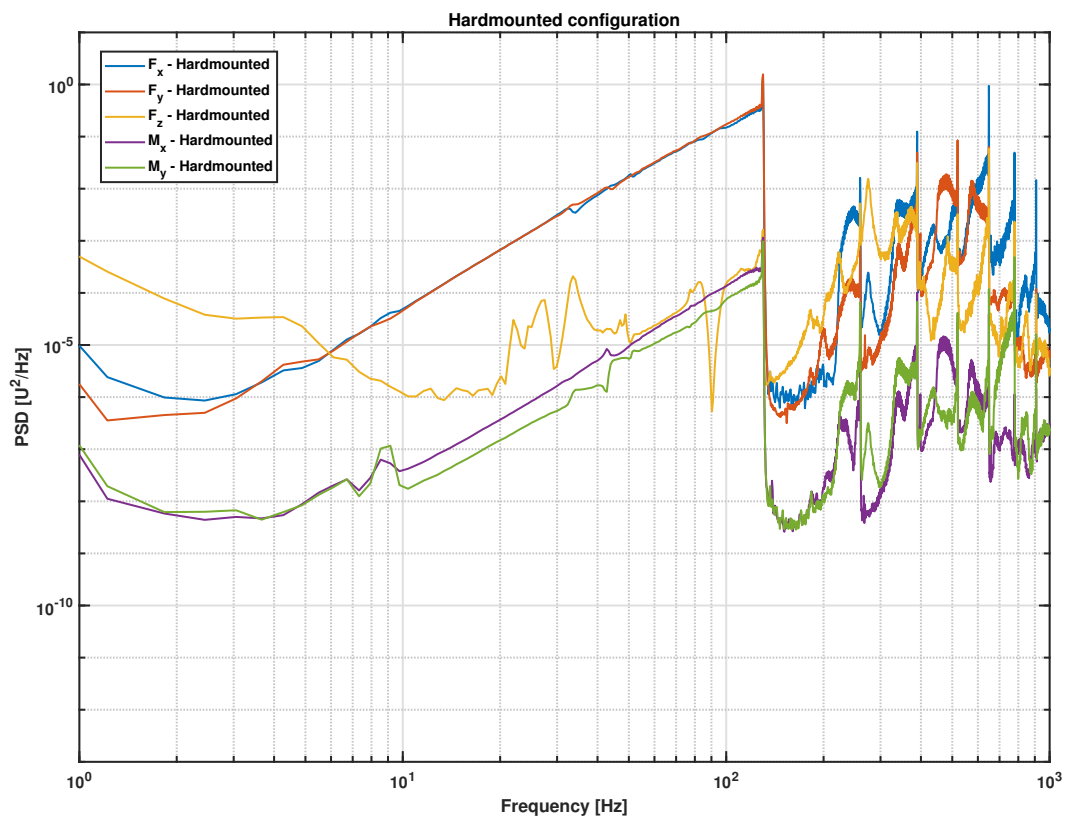


Figure 4.27: Power spectral density of Forces ($U = N$) and Moments ($U = Nm$) measured in the hard-mounted configuration. The effect of the unbalance on the measured signals can be seen in the slope from low frequency up to 130 Hz

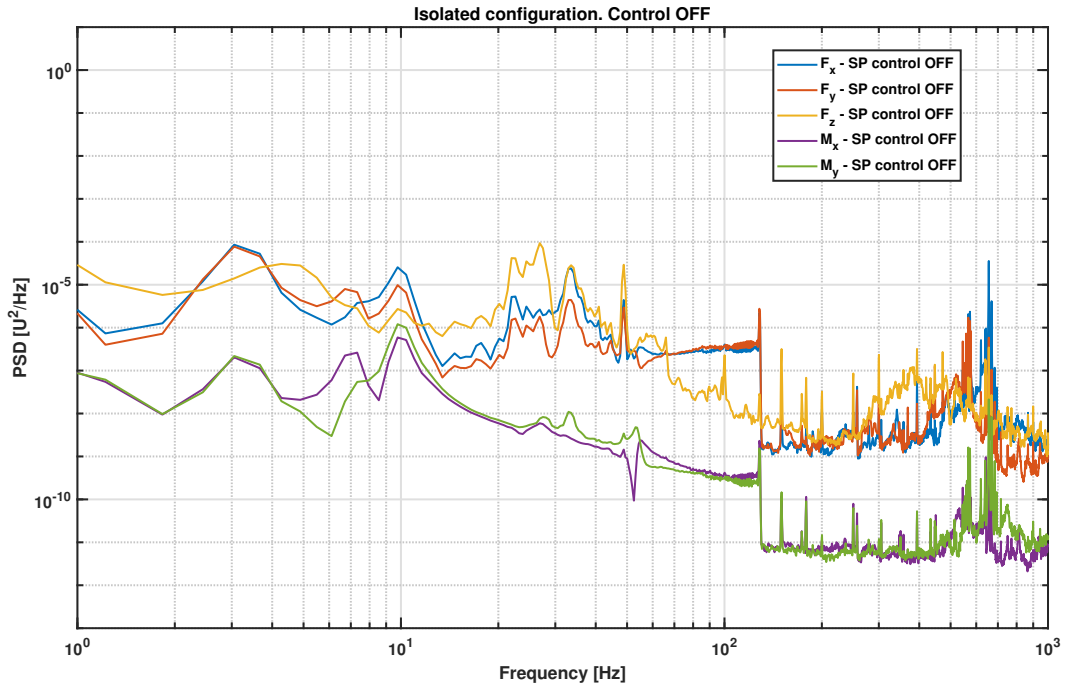


Figure 4.28: Power spectral density of Forces ($U = N$) and Moments ($U = Nm$) with the reaction wheel mounted on the isolator. Control off. The effect of the unbalance is compensated by the roll-off of the isolator

In order to achieve broadband excitation from the reaction wheel, in each test, the rotor was spun up to its maximum speed of 7800 rpm, then power was removed, and the forces and moments were recorded while it coasted down to a stop, taking an average of 300 seconds. The Power Spectral Densities of the forces were computed for both cases. The force and moment transmissibilities of the isolation platform were computed through Eq. 4.8, as proposed in [88]. This is justified, since a good repeatability of the measured disturbances was observed throughout different tests, for both with and without the presence of the isolator platform. As an example, Fig. 4.31 presents the results for the disturbance forces measured in the X direction in three different tests, for the case of the reaction wheel hard-mounted on the dynamometer.

$$|T_{Force}| = \frac{\sqrt{PSD_{isolated}}}{\sqrt{PSD_{hardmounted}}} \quad (4.8)$$

The disturbing forces and moments measured in a particular test in all six degrees of freedom are plotted in Fig. 4.27. The unbalance of the flywheel is responsible for the main disturbance up to 130 Hz, which is manifested by the main harmonic disturbance component. It is observed that the forces and moments in the X and

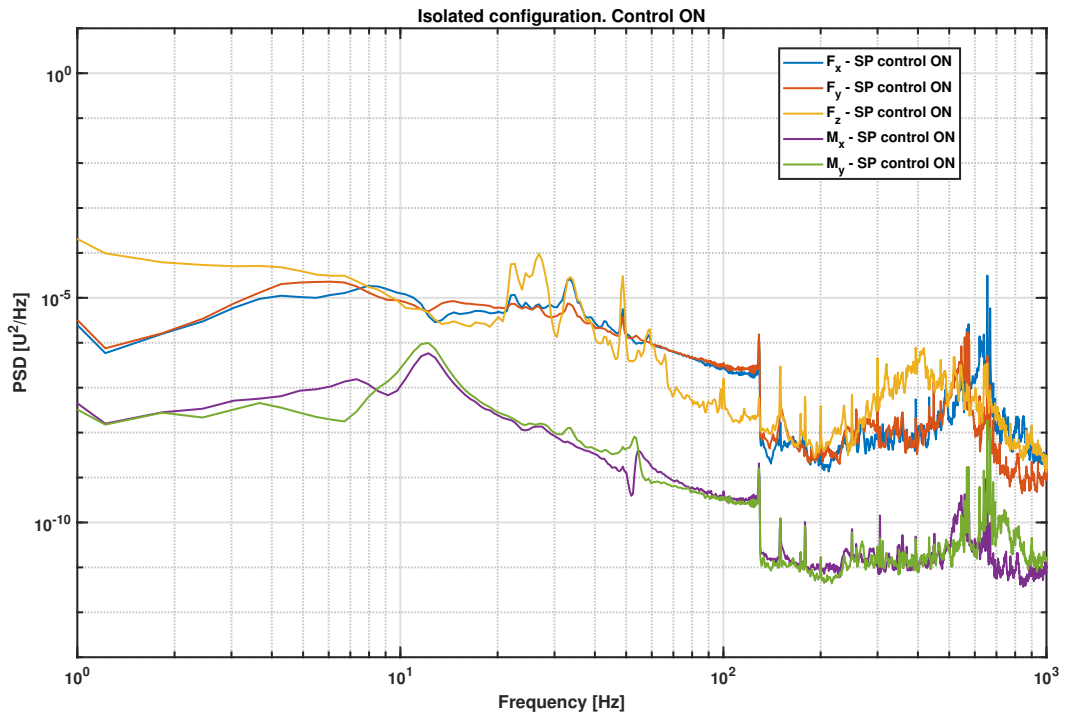
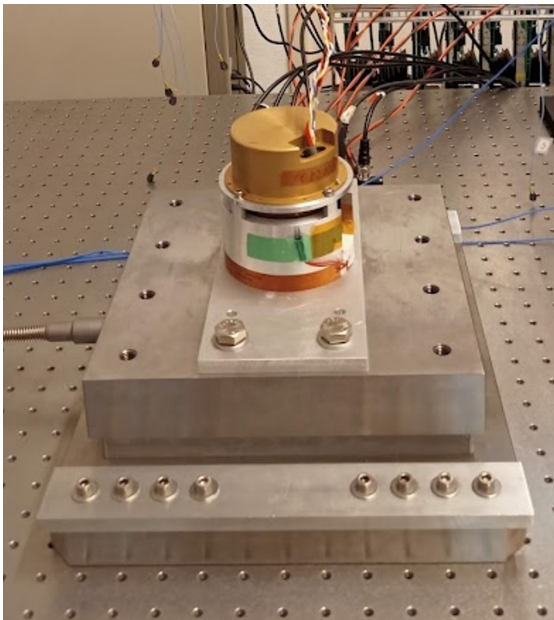
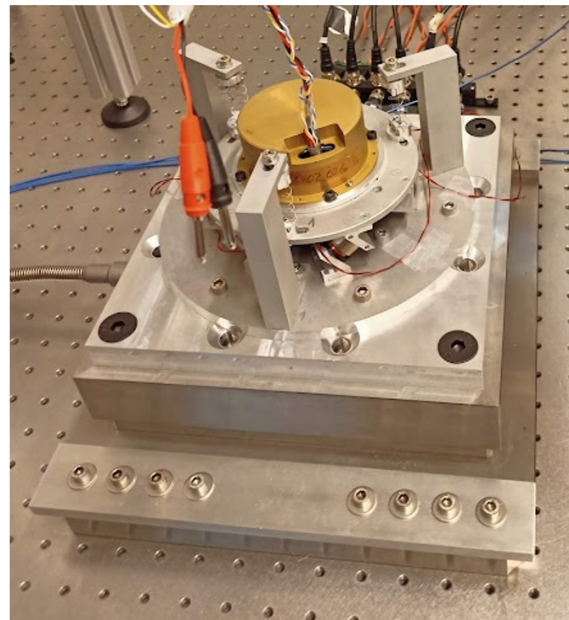


Figure 4.29: Power spectral density of Forces ($U = N$) and Moments ($U = Nm$) with the reaction wheel mounted on the isolator. Control on. Damping of the low frequency resonances can be observed.



(a)



(b)

Figure 4.30: Test configurations to compute the force transmissibility of the isolator. (a) Hard-mounted configuration used as reference; (b) Isolated configuration used for measuring disturbances with isolation platform.

Isolator Performance

Y directions are closely matched due to the circular symmetry of the system. The lower magnitude of the disturbances corresponding to the force along the Z direction is due to the lack of effect of the unbalance in this degree of freedom as the wheel rotates around it.

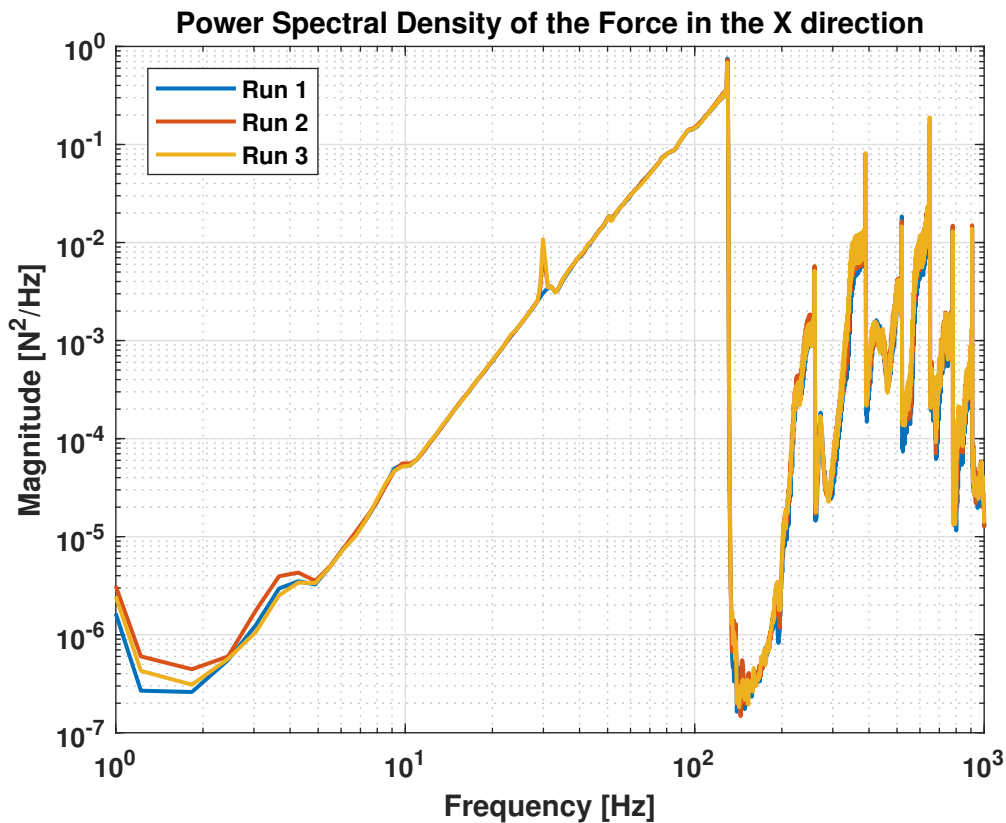


Figure 4.31: Force PSD in the X direction for independent passive coast downs from 7800 rpm, illustrating the repeatability of the disturbances created during a passive coast down of the reaction wheel

The isolation platform was then introduced between the reaction wheel and the dynamometer, with the passive coast down being re-run. The disturbances measured are illustrated in Fig. 4.28 for the case of active control turned OFF, and in Fig. 4.29 for the active control turned ON. In both cases, the disturbances measured above the suspension mode around 5 Hz are significantly lower than when the wheel is hard-mounted without the isolation platform. Furthermore, the active control manages to damp the resonances of the suspension without negatively affecting the isolation at high frequency in a significant way.

Figure 4.32a) superimposes the disturbing forces measured along the X direction for different configurations, including the wheel hard-mounted on the dynamometer, the wheel mounted on the isolation platform with the active control ON and OFF,

and a static wheel used as a reference for background noise. The background noise dominates the measurements made with the isolation platform between 20 Hz and 50 Hz and at multiple limited frequency bands above 130 Hz.

The direct application of Eq.(4.8) to the Fx disturbance measurements from Fig. 4.32a) is illustrated in Fig. 4.32b). It is worth noting that at 130 Hz, an attenuation of -60 dB is achieved while damping the suspension resonance at low frequency when using active control. By introducing damping into the system, the roll-off is degraded, resulting in the effect seen between the main resonance and 130 Hz. However, this effect is negligible if one considers the envelopes of the peaks between control ON and OFF, in this frequency band. Above 130 Hz, the isolation obtained is degraded, due to the background noise being higher in magnitude than the filtered disturbances coming from the reaction wheel. Another phenomenon affecting the transmissibility is that the peaks of the disturbance with and without the isolation platform are very narrow and occur at slightly shifted frequencies, by which the direct application of Eq.(4.8) does not correctly give a measure of the real isolation because it does not capture the reduction of the peaks. For these reasons the transmissibilities shown after 130 Hz are computed from the ratio of the envelopes of the PSD. A dashed line has been included in Fig. 4.32b) to indicate the frequency above which enveloping is applied.

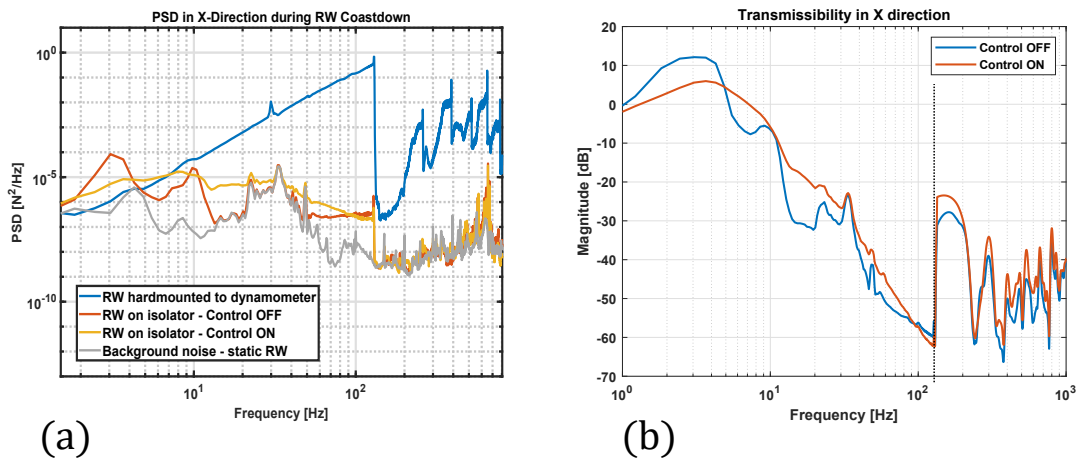


Figure 4.32: (a) Power spectral density of the force in the X-direction. The background noise dominates the signal between 20 - 50 Hz and after 130 Hz; (b) corresponding transmissibility with and without control, showcasing an increase at 130 Hz due to the abrupt decrease of the magnitude of the input excitations, which when isolated is limited by the resolution of the sensors. This results in an inaccurate representation of the transmissibility above 130 Hz

Figure 4.33 shows the reconstructed transmissibilities for the forces in X, Y, and Z and moments around the X and Y axes. The isolator reaches 60 dB of reduction

in the transmitted forces and moments at 130 Hz in the X and Y directions, while successfully damping the main resonance of the isolator, most notably reducing the amplifications in the X and Y directions by 7 and 5 dB respectively. In the Z direction, with active control ON, the performance is degraded when compared to when the active control is OFF. This behavior is caused by the low magnitude of the excitation exerted by the wheel in this direction. The active control enables this isolator to take advantage of a low suspension frequency (5 Hz), without exhibiting harmful amplifications at the resonance, creating an early starting point for the steep roll-off of the transmissibility towards higher frequencies. Band-limiting the active control with the NDF controller ensures that damping is only applied at frequencies around the suspension resonance, reducing the overall damping introduced into the system, and therefore mitigating the deterioration of the roll-off due to the added damping. The transmission path for disturbances has been kept free of secondary resonances, ensuring that the magnitude of the transmissibility keeps decreasing as the frequency increases.

In order to overcome the limited amplitude of disturbance achieved with the functional model of the reaction wheel operating in passive coast down, supplementary tests were carried out to better characterize the isolation platform. As described next, a mini-shaker was used to excite the system above the high noise floor of the test facility occurring at higher frequencies, and the profile of excitation of the reaction wheel model was improved to highlight the benefits of active control in reducing the amplification of the suspension mode down to negligible levels.

4.3.3 Supplementary Tests

Additional tests were performed to improve the characterization of the platform shown in Subsection 4.3.2 in the axial direction both at low and high frequency. At high frequency, Fig. 4.32 a) shows that the background noise surpasses the magnitude of the excitation injected by the reaction wheel, hampering the characterization of the force transmissibility when using the reaction wheel as an excitation source. It is therefore of interest to use a different excitation source to characterize the performance of the isolator above 130 Hz. At low frequency, the interest is to assess the performance of the active control in the axial direction. The difficulty in exciting the suspension mode of the platform with the passive coast down of the reaction wheel, was overcome by applying a stepped spin-up of the reaction wheel.

To improve the characterization at high frequency in the Z direction, the setup shown in Fig. 4.34 is used. A Siemens Qsources miniature shaker has been glued

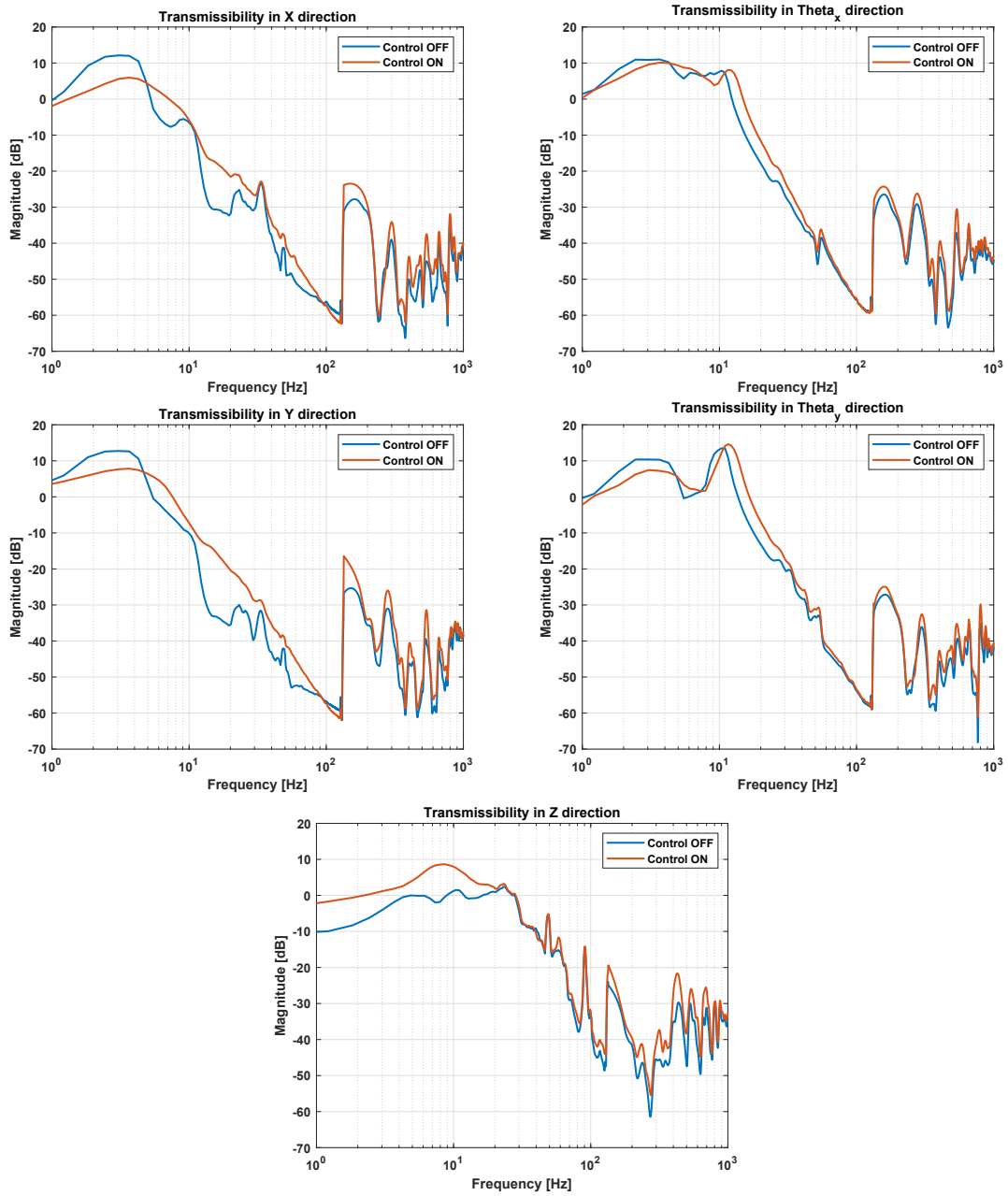


Figure 4.33: *Transmissibility comparison, control off and control on for each direction (X, Y, Z, θ_x , θ_y). Isolation of -60 dB at 130 Hz, limited by background noise >130 Hz.*

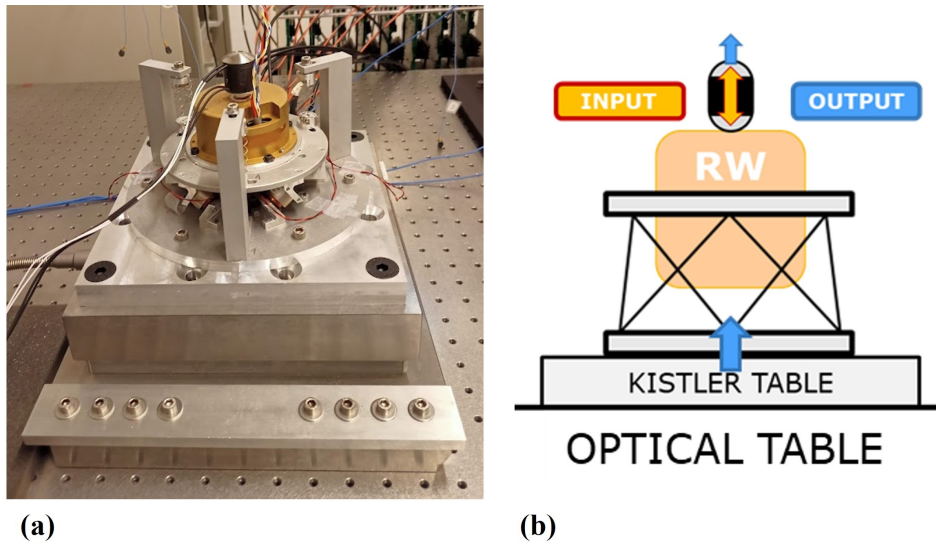


Figure 4.34: (a) Picture of the experimental setup with shaker vertically mounted on the reaction wheel; (b) corresponding diagram

at the center on top of the reaction wheel housing. This shaker has the advantage of having an embedded force sensor enabling the possibility of directly computing the force transmissibility of the isolator. The test is carried out by injecting white noise into the system, band-passed from 90 to 900 Hz. This frequency band has been chosen to create an overlap with the computed transmissibility below 130 Hz while ensuring that the frequency band of interest (130 - 500 Hz) is correctly excited.

As can be observed in Fig. 4.35, the force measured by the dynamometer is above the background noise threshold in the frequency region where the excitation is applied. The resulting transmissibility between the signals from the shaker's embedded sensor and the dynamometer is shown in Fig. 4.36. The frequency axis is zoomed on the bandwidth at which the excitation was applied for clarity. A minimum of -65 dB is reached in the transmissibility at 270 Hz, before climbing to -30 dB. The reason for this increase is found in the dynamics of the test setup, which upon testing, has been shown to present several resonances in the vertical direction between 400 and 1000 Hz.

The final tests carried out have the objective of investigating the apparent lack of performance of the active control shown in the Z direction while performing the reaction wheel tests (Fig. 4.33). Due to the nature of a passive coast down, no constant speed is maintained for an extended period of time, resulting in a lack of consistent excitation at a given frequency, which is exacerbated at low wheel speeds where the reaction wheel coasts to a stop. In order to tackle this issue, a stepped spin-up of the wheel is carried out. The speed is swept from 100 to 7800 rpm in

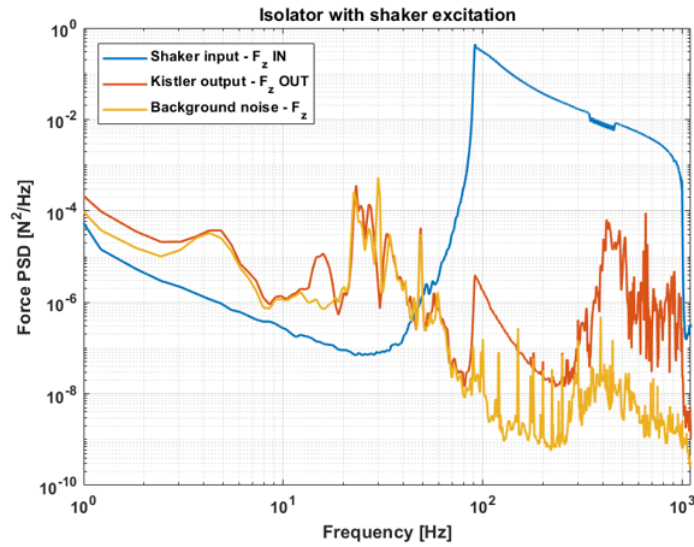


Figure 4.35: Power spectral density of the forces in the vertical direction measured at the shaker and at the dynamometer, with the background noise measurement to check the effectiveness of the input excitation

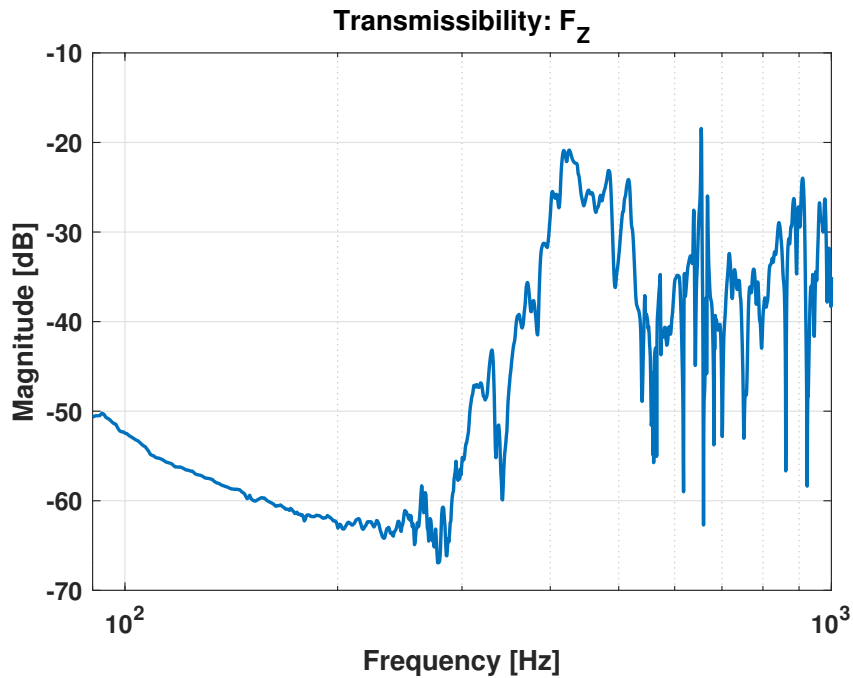


Figure 4.36: Zoomed in (90 - 1000 Hz) force transmissibility in the vertical direction showing a reduction in the transmissibility of 65 dB at 270 Hz, and an increase towards 400 Hz due to the resonance of the Kistler table in the vertical direction

Isolator Performance

increments of 100 rpm at intervals of 60 seconds. While the whole wheel speed range was analyzed for the sake of completeness, the relevant speeds to analyze the low frequency behavior are from 100 to 600 rpm. These tests have been carried out with the reaction wheel mounted on the isolator, with and without active control. For reference, contour plots corresponding to the stepped spin-ups are shown in Fig. 4.37. A drop in magnitude throughout the whole frequency range can be observed in these plots, with a spike at 5 Hz (observed when the wheel spins at 300 rpm) for the case of the isolated wheel with the active control off due to the undamped suspension resonance of the isolator.

Shown in Fig. 4.38 are the waterfall plots for the power spectral density of the force in the Z direction as a function of the wheel speed and the frequency. When the isolator is used in passive mode, without active control, a peak of $1.3\text{e-}3 \text{ N}^2/\text{Hz}$ can be seen at the suspension resonance of the system, at 5 Hz when the reaction wheel is spinning at 300 rpm, which is consistent with the excitation from the wheel's unbalance. This peak is reduced to $1.0\text{e-}4 \text{ N}^2/\text{Hz}$ once the active control is turned on, proving that the active control does indeed contribute to the reduction of the amplification at resonance in the Z direction. The reduction in the magnitude of the PSD corresponds to a reduction of 5 dB in the transmissibility, which is in line with what has been observed in the X and Y directions during the coast down tests.

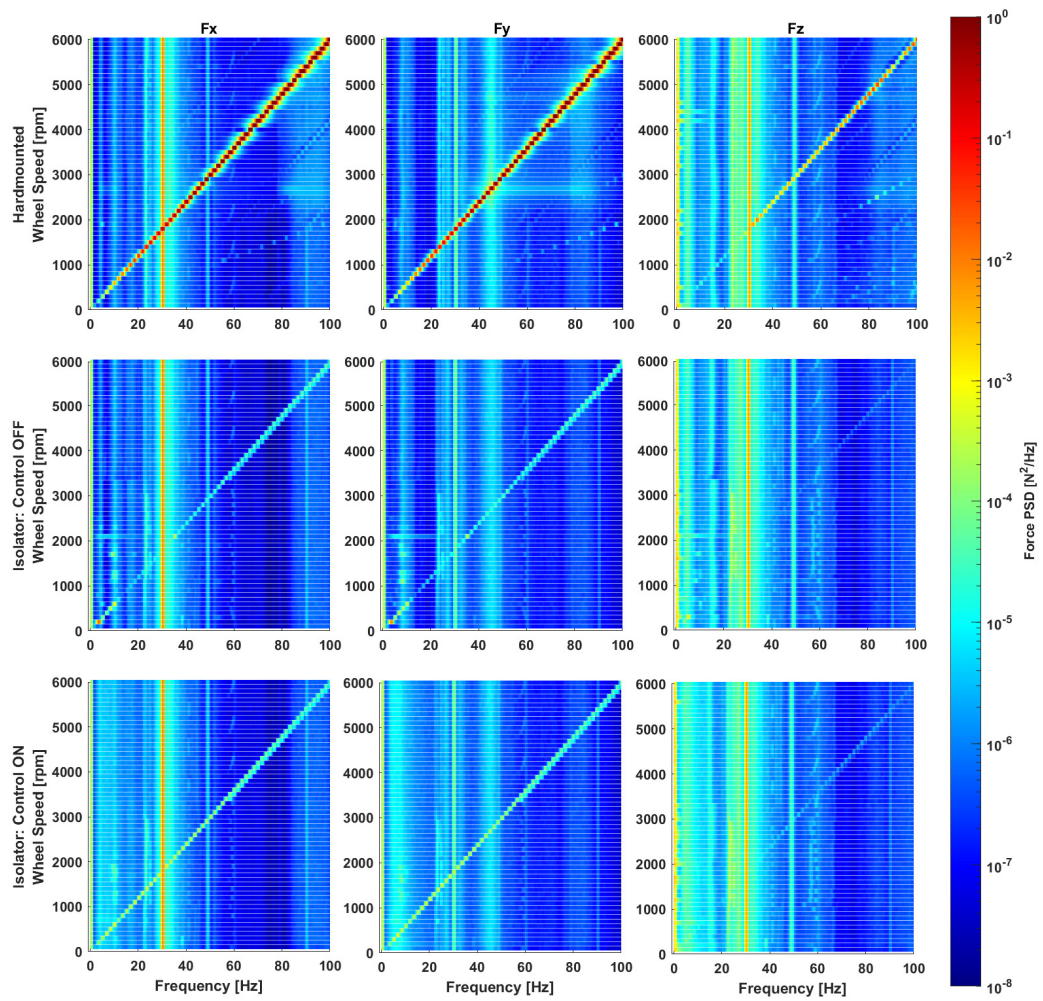


Figure 4.37: Contour plots of the Force PSD as a function of wheel speed and frequency. Columns = output directions, rows = setup configuration.

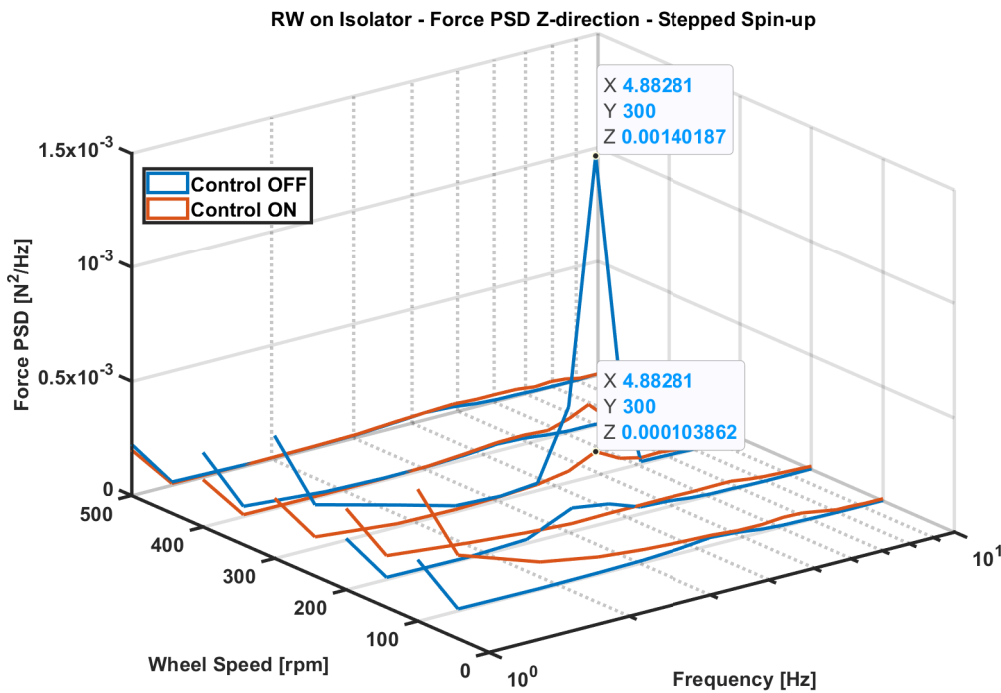


Figure 4.38: Waterfall plot of the force in the Z direction during a stepped spin-up with increments of +100 rpm at 60 s intervals showing the effectiveness of the active control in the vertical (Z) direction. Control off (blue), control on (red).

4.4 Payload Comfort Operating Mode

Having an isolating platform at the interface between the isolator and the spacecraft creates the possibility to not only use it to protect the spacecraft from the disturbances generated by the reaction wheel, but also to protect the reaction wheel during launch further reducing the magnitude of the micro-vibrations generated by the reaction wheel. The isolating platform becomes a dual-purpose system, with the capability of mitigating the launch excitations and reducing the introduction of micro-vibrations into the spacecraft. This new mode of operation of the reaction wheel is referred to as *payload comfort operating mode*.

In order to validate the payload comfort operating mode, a single DOF system analogous to that presented in Section 2.2.1 is modeled with the dynamic behavior of the isolating platform, with the mass representing the suspended portion of the isolator with a reaction wheel. This system has as inputs ground motion and actuator force, and as outputs has the relative motion between the mass and the ground, the absolute motion of the mass, and the actuator force. Knowing the previously mentioned quantities allows us to input different types of disturbances to simulate a launch environment, while performing active control and computing the stroke of

the platform and the force requirement of the actuators.

The controller in Eq.(4.9) has been developed to reduce the magnitude of the excitations reaching the reaction wheel, as well as limiting the stroke of the platform to keep the payload from colliding against the base. This is done by adding stiffness and damping through the voice coils by taking the self-sensed velocity as an input.

$$H(s) = g \frac{(s + 0.9663)(s + 14.95)}{s(s + 4397)} \quad (4.9)$$

A simulation is run with shaped white noise at the input, with its magnitude varying as a function of the frequency. The power spectral densities of the command followed and the recreated signal are shown in Fig. 4.39. Figure 4.40 shows a comparison of the transmissibilities of the controlled and uncontrolled system, where the effects of the active control can be seen, with an increase in the frequency of the system's resonance from 3 to 5 Hz, a reduction of the transmitted disturbances at the resonance by a factor of 10, and a decrease in the isolation factor after the resonance. The combination of these three elements results in a reduction in the overall stroke of the platform seen in Fig. 4.41, while retaining a reduction in the transmitted disturbances higher than a factor 10 after 60 Hz. The stroke of the platform is reduced close to the limit of the current actuators. The goal is to retain a low value for the stroke since the stroke is directly proportional to the distance between the voice coil components. It is desirable to maintain a low value for this distance since there is a loss in force capability of the actuators as the gap between the magnet and the coils increases due to the reduction of density in the magnetic field. Achieving the aforementioned performance, however, comes at the expense of higher force demands from the actuators, as can be seen in Fig. 4.42, with force requirements increasing by a factor of 6 with respect to the current capabilities of the system.

The limits of the current actuators are shown by the horizontal lines in Fig. 4.41 and Fig. 4.42. The actuators must therefore be modified or substituted by different ones in order to achieve these force requirements, but only a limited increase in the clearance between the coil and the magnet in each actuator is needed to accommodate the additional stroke. Furthermore, due to the decoupled nature of the voice coils and the suspension system, modifying the coils while retaining the same magnet does not modify the dynamics of the platform.

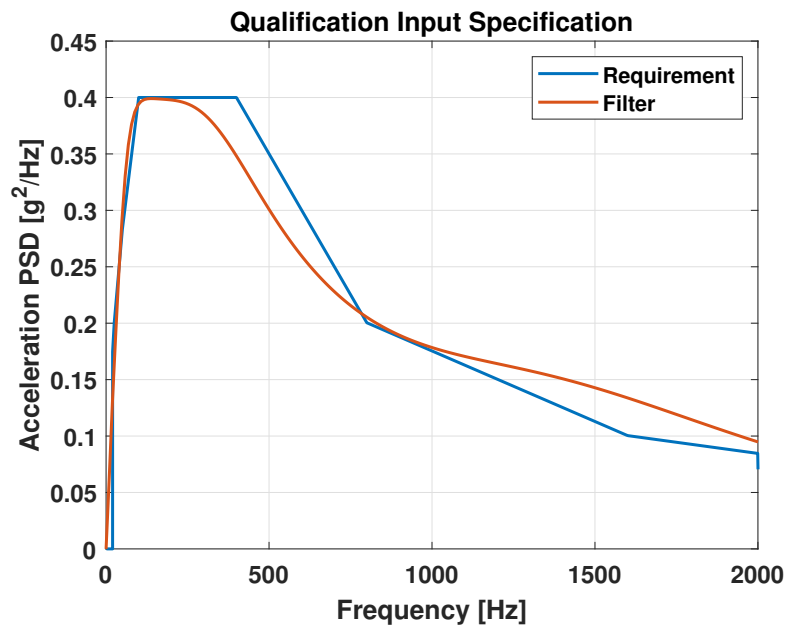


Figure 4.39: Comparison between the qualification requirements and the recreated input signal PSD

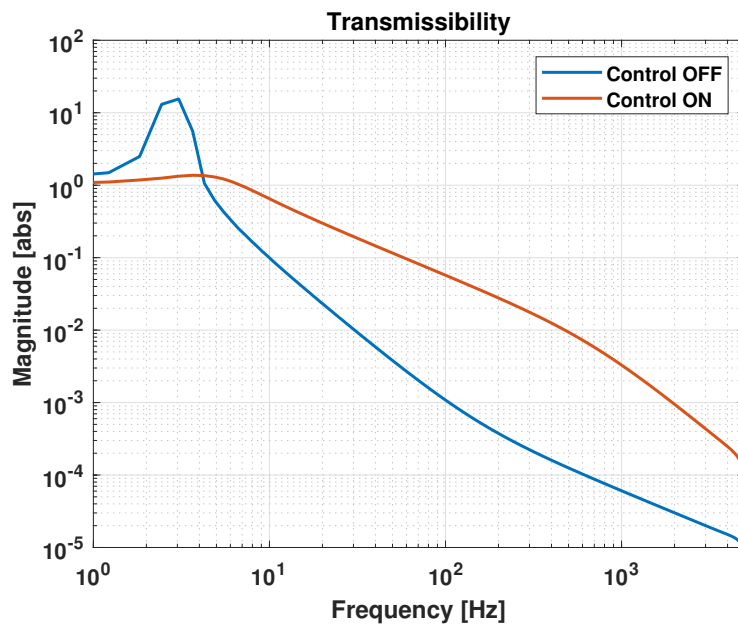


Figure 4.40: Uncontrolled and controlled motion transmissibilities of the isolator

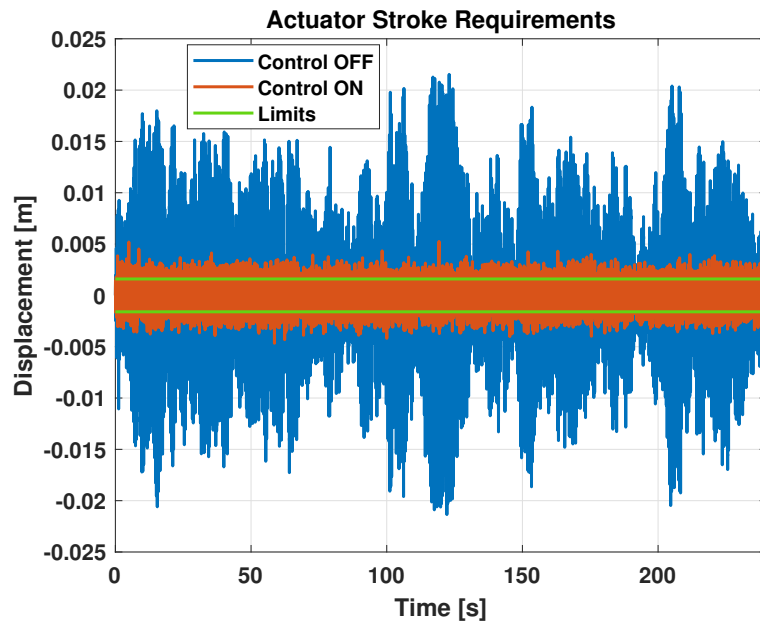


Figure 4.41: *Uncontrolled and controlled stroke of the system when applying the random input shown in Fig. 4.39*

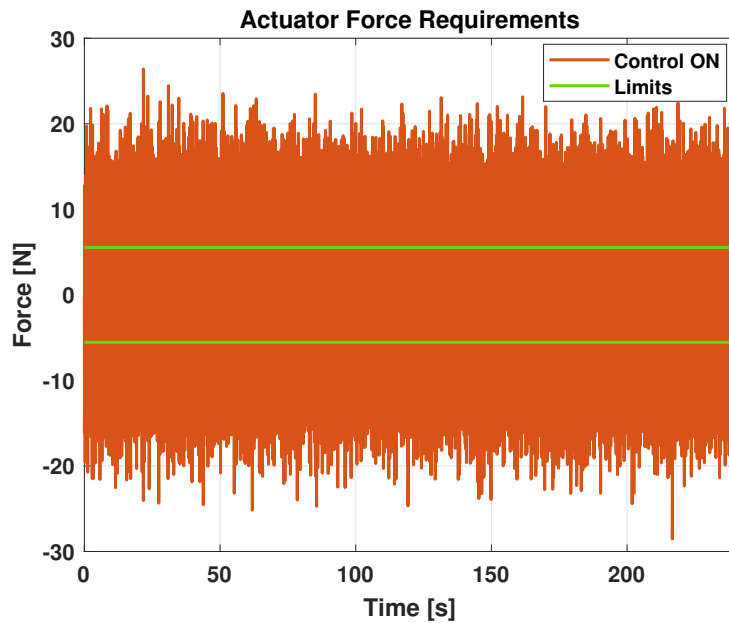


Figure 4.42: *Actuator force required to achieve the performances shown in Fig's 4.40-4.41*

4.5 Conclusions

An innovative concept of an isolation platform for micro-vibrations was successfully developed and tested. The working principle consisted of the introduction of a suspension mode at low frequencies, i.e. around 5 Hz. This enabled achieving high levels of isolation at high frequency thanks to the natural roll-off of such a system, while the amplification of the suspension modes was artificially damped with active control.

The architecture of this isolation system is based on a Stewart platform. The suspension modes are ensured by the integration of soft springs, while the two sides of the platform isostatically interact in six degrees of freedom via voice coil actuators. These voice coils are frameless which helps the mechanical decoupling of the two parts of the platform. They are also self-sensing, in which the monitoring of their voltage and current produces an estimate of the relative velocity of the two sides of the platform thereby enabling the active damping of the suspension modes.

An isolation performance of -65 dB was attained at 200 Hz when the platform was tested with a shaker in the axial direction. A slight degradation is observed when the suspension was tested with the functional model of a reaction wheel simultaneously disturbing the six degrees of freedom. This small degradation of performance does not hinder the attractiveness of the concept and is attributed to the limited amplitude of disturbances at high frequencies of the wheel used as the source, and non-optimal test environment in terms of noise and structural dynamics.

An initial study of the capabilities of this isolator to have an additional function of protecting its payload during launch has been introduced, showing that with modifications to the active elements acceptable performance levels in terms of transmitted disturbances to the payload can be achieved.

Future enhancements of this concept can consist of the implementation and verification of the functionality of the active alleviation of the launch loads, the scalability required for isolating the micro-vibrations generated by larger reaction wheels or their assemblies as well as reducing the natural frequency of the suspension modes and stiffening of the structural elements in order to improve the overall isolation performance.

Conclusions and Perspectives

Conclusions

Throughout the course of this thesis, two active isolation systems for space applications have been developed.

A whole-spacecraft isolation system has been investigated for use at the interface between the launch vehicle and the spacecraft in order to mitigate the loads originating from the launch environment. Current isolation systems employed during launch are typically comprised of a flexible structure placed at the interface between the launch vehicle and the spacecraft. The isolation provided stems from the low resonance frequency at the interface, successfully reducing the magnitude of the transmitted disturbances at frequencies above this resonance. By including viscoelastic material in the structure damping is added to reduce the magnification at the resonance frequency, which in turn reduces the performance of the isolation. The goal of the isolator developed in this thesis is to bypass the natural trade-off between isolation and damping through the use of active control. This isolation system has been demonstrated to successfully damp resonances and provide isolation in a broad bandwidth, while showcasing high robustness and stability in its controller due to the collocated nature of the sensors and actuators.

The second isolator developed within the framework of this thesis is an active isolation platform for reaction wheel-borne micro-vibrations. On one hand, the increase in performance of the scientific equipment onboard spacecraft creates the need for a quieter, more stable environment in which to operate. On the other hand, the reliance on reaction wheels for attitude control of spacecraft creates a noisy environment inside a spacecraft. The mechanical decoupling of these elements is therefore gaining importance. To achieve this goal, an active isolation, multi-DOF platform has been developed. The isolator consisting of six self-sensing, frameless voice coils in a cubic Stewart-Gough platform configuration is to be placed at the

Perspectives and future works

interface between a reaction wheel and a spacecraft, where it has been shown to be able to reduce by a factor of up to 65 dB the transmitted disturbances.

To the best of my knowledge, this performance has not been reported so far.

The working principle of this isolator is to have a low resonance frequency, provided by a set of 6 soft suspension springs. To maximize the isolation capabilities of the platform, the different components have been selected to not present any spurious resonances below 500 Hz. The active control is done by computing the relative velocity between the ends of each voice coil and feeding it back with a controller whose parameters have been selected to obtain an optimal trade-off between damping of the suspension modes and degradation of the isolation.

Perspectives and future works

This thesis has mainly dealt with the development of novel active isolation systems for space applications. Two technological demonstrators have been built and tested. The avenues of research that could be followed towards the improvement of these systems are summarized hereafter.

Whole spacecraft vibration isolation system

While successfully providing isolation, the limiting factor for the system is the maximum deflection it can undergo. With the selected controller, a degradation of the low frequency compliance occurs, which in turn increases the deformation experienced by the isolator. Commercially available amplified piezoelectric stacks were used as sensor-actuator pairs in this system. A possible solution to increase the stroke of the actuator would be to stack several actuators in series. In the case of pursuing this route, the mechanical connections between the actuators should be done in such a way that no local deformation modes are introduced in the frequency band of interest.

Micro-vibration isolation system

This thesis has set the groundwork for the development of a high-performance micro-vibration isolation system. As such, several components were chosen for their readiness in availability and ease of access or manufacturing. This resulted in a

technological demonstrator that succeeded in achieving the desired performance, but with components that have room to be further optimized.

Actuators

The isolator can be adapted to be used not only for micro-vibration isolation but also for the protection of the reaction wheels during launch by modifying the actuators. The commercial actuators used have a clearance of 1.5 mm between the coils and the magnet. These actuators were selected due to their small footprint, and good force-to-clearance ratio. By redesigning the voice coils with larger coils and more powerful magnets, it is possible to further increase both their clearance and output force. This would enable the isolator to not only be used for micro-vibration isolation but also for payload comfort.

Substituting the mono-coil actuators by double coil actuators would introduce an extra layer of safety into the system. This way, if one coil fails, half of the performances are retained. Furthermore, dividing the coil in two would also allow us to specifically design each coil section for a different purpose. Where one coil could be optimized toward providing a more sensitive velocity estimation, and the other coil could target a higher force output.

Alignment mechanism

The combination of the limited operating range of the isolator due to the low clearance of the voice coils, and the slight differences between the springs, resulted in alignment difficulties. A redesign of the alignment mechanism, using micro-metric screws to adjust the radial position of the screws, and interlocking nuts at each end to prevent the spring elements from rotating during tightening would greatly improve the alignment process.

Weight reduction

Aluminum was used for the manufacture of all the structural components of the isolator. However, it would be interesting to produce the structural components in CFRP, due to its reduced weight. Alternatively, a topological optimization of the structure could be carried out, allowing for the elimination of unnecessary material from the design, followed by creating an aluminum monolithic structure for the base and the top platforms.

Scalability

The isolator has been built around the characteristics of the specific reaction wheel made available for testing at the European Space Agency. It is therefore only suitable for reaction wheels of similar dimensions and mass properties. Creating a parametric model of the platform would allow us to study the effect of modifying the payload of the isolator and evaluate the changes needed in order to adapt it to different payloads.

Implementation of non-linear response

As outlined throughout the document, the launch and in-orbit environments present disturbances which differ by at least 3 orders of magnitude. In order to take full advantage of placing an isolator at the interface of a unit inside of a spacecraft, it becomes interesting for the isolator to be able to deal with both environments. This could be done by both passive and active means, opening an interesting future avenue of potential studies regarding the research presented in this thesis. By substituting the current springs used in the isolator presented in Chapter 4 by springs designed to have a non-linear stiffness, the isolator could be able to withstand the launch environment while still remaining effective during the in-orbit, microvibration isolation phase.

A similar approach could be followed with the active components, designing a non-linear controller which reacts by increasing the stiffness when facing high magnitude inputs, and by decreasing the stiffness and increasing the damping when subjected to low magnitude inputs.

DOF dependent stiffness

In the developed platform, conceived as a technological demonstrator, the target was to reach similar stiffness in the 6 DOF of the platform. The resulting 3 and 5 Hz resonance frequencies in the translation and rotation degrees of freedom respectively, are proof that this was successfully achieved. However, when dealing with reaction wheels, it is interesting to retain a higher stiffness in the rotational degree of freedom of the wheel. Having a higher stiffness in this axis of rotation is desirable as it results in a reduced impact of the dynamics of the isolator on the control authority of the AOCS strategies on the satellite. This is also interesting, because the magnitude of the disturbances injected along this degree of freedom is negligible compared to the rest, meaning that the isolation performance of the isolator would not be impacted by such a modification.

Published works

During the course of the thesis, I have participated as main author or contributing author in the works detailed in this section.

Journal Articles

1. Multi-degree-of-freedom active isolation platform for microvibrations [89]
Author list: V. Lafarga, R. Jamshidi, G. Rodrigues, R. Seiler, C. Collette
Journal: Journal of Spacecraft and Rockets
Year: 2024
2. Perfect collocation using self-sensing electromagnetic actuator: Application to vibration control of flexible structures [78]
Author list: M. Verma, V. Lafarga, C. Collette
Journal: Sensors and Actuators A: Physical
Year: 2020
3. Active stabilization of unmanned aerial vehicle imaging platform [90]
Author list: M. Verma, V. Lafarga, M. Baron, C. Collette
Journal: Journal of Vibration and Control
Year: 2020
4. Multi-degree of freedom isolation system with high-frequency roll-off for drone camera stabilization [91]
Author list: M. Verma, V. Lafarga, T. Dehaeze, C. Collette
Journal: IEEE Access
Year:
5. A concept of active mount for space applications [51]
Author list: A. Souleille, T. Lampert, V. Lafarga, S. Hellegouarch, A. Rondineau, G. Rodrigues, C. Collette
Journal: CEAS Space Journal
Year: 2018

Conferences

1. Multi Degree of Freedom Micro-Vibration Isolator with Frameless Actuators [92]
Author list: V. Lafarga, M. Verma, G. Rodrigues, C. Collette
Conference: Aerospace Europe Conference
Year: 2020
2. Hybrid isolator for space applications [52]
Author list: V. Lafarga, V. Gadanho, G. Rodrigues, C. Collette
Conference: ECSSMet
Year: 2018
3. Payload isolation from launcher's disturbances (Poster)
Author list: V. Lafarga, G. Rodrigues, C. Collette
Conference: 25 Years of Belgians in Space SCK-CEN
Year: 2017

References

- [1] *Spacecraft mechanical loads analysis handbook*, ch. 13. ECSS Secretariat, 2013. Cited on pages ix and 3.
- [2] C. D. Johnson and P. S. Wilke, “Whole-spacecraft shock isolation system,” in *Smart Structures and Materials 2002: Damping and Isolation*, vol. 4697, pp. 1–8, SPIE, 2002. Cited on pages ix and 19.
- [3] R. Johal, J. Christensen, and D. Doud, “Orbcomm generation 2 access to leo on the falcon 9 using softride, a case history,” 2012. Cited on pages x, 19, 20, and 35.
- [4] e. a. Camelo, V., “Damping and isolation concepts for large space telescopes,” *AIAA Journal*, 2009. Cited on pages x, 19, 20, and 21.
- [5] e. a. Tang, J., “Design and experimental study of a vcm-based whole-spacecraft vibration isolation system,” *J. Areosp*, vol. 31, 2005. Cited on pages x, 19, and 21.
- [6] M. D. Hasha, “High-performance reaction wheel optimization for fine-pointing space platforms: Minimizing induced vibration effects on jitter performance plus lessons learned from hubble space telescope for current and future spacecraft applications,” in *43rd Aerospace Mechanisms Symposium*, 2016. Cited on pages x, 24, and 25.
- [7] J. F. Wilson and L. P. Davis, “Viscous damped space structure for reduced jitter,” in *Proc. 58th Shock and Vibration Symp*, 1987. Cited on pages x, 24, 25, and 26.
- [8] G. CARTE, G. COURGENAY, F. JOHANSSON, T. DEMERVILLE, A. MRÓZ, M. Kokot, and G. RODRIGUES, “Isolation and damping systems for space applications,” no. 359424516, 2020. Cited on pages x, 24, and 25.
- [9] A. J. Bronowicki, “Vibration isolator for large space telescopes,” *Journal of spacecraft and rockets*, vol. 43, no. 1, pp. 45–53, 2006. Cited on pages x, 9, 26, 28, 29, and 59.
- [10] Moticont, “Linear voice coil motor lvcm-022-013-02 large radial gap - data sheet.” Cited on pages xvii and 71.
- [11] D. Greslou, F. De Lussy, J. Delvit, C. Dechoz, and V. Amberg, “Pleiades-hr innovative techniques for geometric image quality commissioning,” *Int. Arch. Photogramm. Remote Sens. Spat. Inf. Sci*, vol. 39, p. B1, 2012. Cited on page 9.

-
- [12] S. Arnon and N. S. Kopeika, “Laser satellite communication network-vibration effect and possible solutions,” *Proceedings of the IEEE*, vol. 85, no. 10, pp. 1646–1661, 1997. Cited on pages 9 and 58.
- [13] L. Massotti, A. Bulit, I. Daras, B. C. Dominguez, O. Carraz, K. Hall, A. Hélière, G. March, P. Martimort, G. Rodrigues, *et al.*, “Next generation gravity mission design activities within the mass change and geoscience international constellation,” in *Sensors, Systems, and Next-Generation Satellites XXVI*, vol. 12264, pp. 6–17, SPIE, 2022. Cited on page 9.
- [14] T. Agócs, F. Vanin, P. Laberinti, H. Oetjen, D. Serlenga, M. P. Sole, C. Salenc, D. Lamarre, M. Kaspers, G. Rodrigues, *et al.*, “Far-infrared outgoing radiation understanding and monitoring (forum)–system overview and key technology developments of esa’s 9 th earth explorer,” in *IGARSS 2022-2022 IEEE International Geoscience and Remote Sensing Symposium*, pp. 7186–7189, IEEE, 2022. Cited on page 9.
- [15] O. Lux, C. Lemmerz, F. Weiler, T. Kanitz, D. Wernham, G. Rodrigues, A. Hyslop, O. Lecrenier, P. McGoldrick, F. Fabre, *et al.*, “Aladin laser frequency stability and its impact on the aeolus wind error,” *Atmospheric Measurement Techniques*, vol. 14, no. 9, pp. 6305–6333, 2021. Cited on page 9.
- [16] Z. Georgiev and L. Kunchev, “Study of the vibrational behaviour of the components of a car suspension,” in *MATEC Web of Conferences*, vol. 234, p. 02005, EDP Sciences, 2018. Cited on page 13.
- [17] C. Collette, S. Janssens, and K. Artoos, “Review of active vibration isolation strategies,” *Recent patents on Mechanical engineering*, vol. 4, no. 3, pp. 212–219, 2011. Cited on pages 16 and 35.
- [18] A. Preumont, J.-P. Dufour, and C. Malekian, “Active damping by a local force feedback with piezoelectric actuators,” *Journal of guidance, control, and dynamics*, vol. 15, no. 2, pp. 390–395, 1992. Cited on pages 17 and 36.
- [19] S. Chesné, A. Milhomem, and C. Collette, “Enhanced damping of flexible structures using force feedback,” *Journal of Guidance, Control, and Dynamics*, vol. 39, no. 7, pp. 1654–1658, 2016. Cited on pages 17 and 36.
- [20] C. Collette and S. Chesne, “Robust hybrid mass damper,” *Journal of sound and vibration*, vol. 375, pp. 19–27, 2016. Cited on page 18.
- [21] J. White, E. Fowler, and K. Noble, “Softride® shock and vibration isolation systems,” in *2nd workshop on spacecraft shock environment and verification, ESA-ESTEC, Noordwijk, The Netherlands*. Cited on pages 18 and 35.

REFERENCES

- [22] W. P. Johnson, C. D., “Protecting satellites from the dynamics of the launch environment,” 2003. Cited on page 18.
- [23] e. a. Liu, L., “Octo-strut vibration isolation platform and its application to whole spacecraft vibration isolation,” *Journal of Sound and Vibration*, vol. 289, pp. 726–744, 2006. Cited on page 21.
- [24] G. R. Thomas, C. M. Fadick, and B. J. Fram, “Launch vehicle payload adapter design with vibration isolation features,” in *Smart Structures and Materials 2005: Damping and Isolation*, vol. 5760, pp. 35–45, International Society for Optics and Photonics, 2005. Cited on pages 21 and 35.
- [25] e. a. Li, H., “Experiments on active precision isolation with a smart conical adapter,” *Journal of Sound and Vibration*, vol. 374, pp. 17–28, 2016. Cited on page 21.
- [26] F. Steier, T. Runte, A. Monsky, T. Klock, and G. Laduree, “Managing the microvibration impact on satellite performances,” *Acta Astronautica*, vol. 162, pp. 461–468, 2019. Cited on pages 22 and 58.
- [27] L. Lin, Y. Li, W. Li, R. Zheng, W. Yanpeng, and W. Xiaoyan, “Recent advances in precision measurement & pointing control of spacecraft,” *Chinese Journal of Aeronautics*, vol. 34, no. 10, pp. 191–209, 2021. Cited on pages 22 and 59.
- [28] M. Vitelli, B. Specht, and F. Boquet, “A process to verify the microvibration and pointing stability requirements for the bepicolombo mission,” in *International Workshop on Instrumentation for planetary missions*, vol. 1683, p. 1023, 2012. Cited on pages 22 and 59.
- [29] C. Dennehy and O. S. Alvarez-Salazar, “Spacecraft micro-vibration: a survey of problems, experiences, potential solutions, and some lessons learned,” tech. rep., 2018. Cited on page 22.
- [30] H. Kinter, D. Just, and B. Mullet, “Meteosat third generation navigation approach,” in *Proc. 22nd Int. Symp. Space Flight Dyn*, 2011. Cited on page 23.
- [31] A. Wolf and N. Dennehy, “Applications of microthrusters on astrophysics missions with demanding jitter requirements,” *Bulletin of the American Astronomical Society*, vol. 51, no. 7, p. 168, 2019. Cited on page 23.
- [32] S. Heindel, F. Liebold, and L. Sander, “A gas bearing reaction wheel supplied by ultrasonic pumps,” in *ESMATS 2021 - 19th European Space Mechanisms and Tribology*, 2021. Cited on page 24.
- [33] R. G. Ross Jr, “Vibration suppression of advanced space cryocoolers: An overview,” *Smart structures and materials 2003: Damping and isolation*, vol. 5052, pp. 1–12, 2003. Cited on page 24.

-
- [34] G. Carte, “Reaction wheel vibration isolator with elastomeric stoppers for launch load,” in *13th European Conference on Spacecraft Structures, Materials & Environmental Testing*, vol. 727, p. 9, 2014. Cited on pages 24 and 59.
- [35] S.-C. Kwon, M.-S. Jo, and H.-U. Oh, “Experimental validation of fly-wheel passive launch and on-orbit vibration isolation system by using a superelastic sma mesh washer isolator,” *International Journal of Aerospace Engineering*, vol. 2017, 2017. Cited on pages 25 and 59.
- [36] D. Kamesh, R. Pandiyan, and A. Ghosal, “Passive vibration isolation of reaction wheel disturbances using a low frequency flexible space platform,” *Journal of sound and vibration*, vol. 331, no. 6, pp. 1310–1330, 2012. Cited on page 26.
- [37] Z. Wei, D. Li, Q. Luo, and J. Jiang, “Performance analysis of a flywheel microvibration isolation platform for spacecraft,” *Journal of Spacecraft and Rockets*, vol. 52, no. 4, pp. 1263–1268, 2015. Cited on pages 26 and 59.
- [38] D. Stewart, “A platform with six degrees of freedom,” *Proceedings of the institution of mechanical engineers*, vol. 180, no. 1, pp. 371–386, 1965. Cited on pages 26, 29, and 60.
- [39] K. J. Pendergast and C. J. Schauwecker, “Use of a passive reaction wheel jitter isolation system to meet the advanced x-ray astrophysics facility imaging performance requirements,” in *Space Telescopes and Instruments V*, vol. 3356, pp. 1078–1094, SPIE, 1998. Cited on page 26.
- [40] B. De Marneffe, M. Avraam, A. Deraemaeker, M. Horodinca, and A. Preumont, “Vibration isolation of precision payloads: A six-axis electromagnetic relaxation isolator,” *Journal of Guidance, Control, and Dynamics*, vol. 32, no. 2, pp. 395–401, 2009. Cited on page 26.
- [41] Y. Zheng, Q. Li, B. Yan, Y. Luo, and X. Zhang, “A stewart isolator with high-static-low-dynamic stiffness struts based on negative stiffness magnetic springs,” *Journal of Sound and Vibration*, vol. 422, pp. 390–408, 2018. Cited on pages 26 and 60.
- [42] J. Spanos, Z. Rahman, and G. Blackwood, “A soft 6-axis active vibration isolator,” in *Proceedings of 1995 American Control Conference-ACC’95*, vol. 1, pp. 412–416, IEEE, 1995. Cited on pages 26 and 60.
- [43] L. P. Davis, D. R. Carter, and T. T. Hyde, “Second-generation hybrid d-strut,” in *Smart Structures and Materials 1995: Passive Damping*, vol. 2445, pp. 161–175, International Society for Optics and Photonics, 1995. Cited on pages 26, 27, and 59.
- [44] A. Hanieh, *Active isolation and damping of vibrations via Stewart platform*. PhD thesis, Universite Libre de Bruxelles, 2003. Cited on page 26.

REFERENCES

- [45] A. Stabile, G. S. Aglietti, G. Richardson, and G. Smet, “Design and verification of a negative resistance electromagnetic shunt damper for spacecraft micro-vibration,” *Journal of Sound and Vibration*, vol. 386, pp. 38–49, 2017. Cited on pages 26 and 27.
- [46] V. V. Yotov, A. Stabile, G. Aglietti, G. Richardson, P. Spanoudakis, F. Cosandier, P. Schwab, E. Wegrzyn, G. De Zanet, and G. Smet, “Development and testing of an electromagnetic platform for microvibration suppression,” in *AIAA SCITECH 2023 Forum*, p. 2067, 2023. Cited on pages 26 and 27.
- [47] A. Bronowicki, “Forensic investigation of reaction wheel nutation on isolator,” in *49th AIAA/ASME/ASCE/AHS/ASC Structures, Structural Dynamics, and Materials Conference, 16th AIAA/ASME/AHS Adaptive Structures Conference, 10th AIAA Non-Deterministic Approaches Conference, 9th AIAA Gossamer Spacecraft Forum, 4th AIAA Multidisciplinary Design Optimization Specialists Conference*, p. 1953, 2008. Cited on pages 26 and 60.
- [48] D.-O. Lee, G. Park, and J.-H. Han, “Hybrid isolation of micro vibrations induced by reaction wheels,” *Journal of Sound and Vibration*, vol. 363, pp. 1–17, 2016. Cited on page 27.
- [49] L. Vaillon, B. Petitjean, B. Frapard, and D. Lebihan, “Active isolation in space truss structures: from concept to implementation,” *Smart materials and structures*, vol. 8, no. 6, p. 781, 1999. Cited on page 29.
- [50] V. E. Gough, “Universal tyre test machine,” *Proc. FISITA 9th Int. Technical Congr., London, 1962*, pp. 117–137, 1962. Cited on page 29.
- [51] A. Souleille, T. Lampert, V. Lafarga, S. Hellegouarch, A. Rondineau, G. Rodrigues, and C. Collette, “A concept of active mount for space applications,” *CEAS Space Journal*, vol. 10, no. 2, pp. 157–165, 2018. Cited on pages 34 and 107.
- [52] V. Lafarga, V. Gadanho, G. Rodrigues, and C. Collette, “Hybrid isolator for space applications,” in *ECSSMet*, vol. 192, European Space Agency, 2018. Cited on pages 34 and 108.
- [53] Y. Chen, B. Fang, T. Yang, and W. Huang, “Study of whole-spacecraft vibration isolators based on reliability method,” *Chinese Journal of Aeronautics*, vol. 22, no. 2, pp. 153–159, 2009. Cited on page 35.
- [54] C. D. Johnson, P. S. Wilke, and S. C. Pendleton, “Softride vibration and shock isolation systems that protect spacecraft from launch dynamic environments,” in *Proceedings of the 38th aerospace mechanisms symposium, Langley Research Center*, pp. 89–102, 2006. Cited on page 35.

-
- [55] W. D. Lan, V. Kaushish, and J. H. Newman, “Progress in reducing vibration levels on the naval postgraduate school cubesat launcher,” 2015. Cited on page 35.
- [56] W. Chi, D. Cao, and W. Huang, “Design of active whole-spacecraft vibration isolation based on voice-coil motor,” in *Sensors and Smart Structures Technologies for Civil, Mechanical, and Aerospace Systems 2014*, vol. 9061, pp. 1041–1047, SPIE, 2014. Cited on page 35.
- [57] A. Rittweger, H.-G. Beig, P. Konstanzer, and R. Bureo Dacal, “Feasibility demonstration of an active payload adapter for ariane 5,” in *Spacecraft Structures, Materials and Mechanical Testing 2005*, vol. 581, 2005. Cited on page 35.
- [58] H. Strauch, C. Jetzschmann, and J. Albus, “Robust controller design and testing of an active isolation for a payload-launcher system,” in *9th international ESA conference on guidance, navigation and control system, Porto*, 2014. Cited on page 35.
- [59] P. Jean, *Isolation vibratoire par contrôle semi-actif d’amortisseurs magnéto-rhéologiques pour l’interface lanceur/charge utile*. PhD thesis, Conservatoire national des arts et métiers-CNAM, 2006. Cited on page 35.
- [60] P. Jean, R. Ohayon, and D. Le Bihan, “Semi-active control using magneto-rheological dampers for payload launch vibration isolation,” in *Smart Structures and Materials 2006: Damping and Isolation*, vol. 6169, p. 61690H, International Society for Optics and Photonics, 2006. Cited on page 35.
- [61] A. Preumont, *Vibration control of active structures: an introduction*, vol. 246. Springer, 2018. Cited on pages 36 and 47.
- [62] A. Preumont, A. Francois, F. Bossens, and A. Abu-Hanieh, “Force feedback versus acceleration feedback in active vibration isolation,” *Journal of sound and vibration*, vol. 257, no. 4, pp. 605–613, 2002. Cited on page 36.
- [63] B. De Marneffe, “Active and passive vibration isolation and damping via shunted transducers,” *These, Faculté des Sciences Appliquées, Université Libre de Bruxelles*, 2007. Cited on page 44.
- [64] S. R. Moheimani, “A survey of recent innovations in vibration damping and control using shunted piezoelectric transducers,” *IEEE transactions on control systems technology*, vol. 11, no. 4, pp. 482–494, 2003. Cited on page 44.
- [65] N. W. Hagood and A. Von Flotow, “Damping of structural vibrations with piezoelectric materials and passive electrical networks,” *Journal of sound and vibration*, vol. 146, no. 2, pp. 243–268, 1991. Cited on page 49.
- [66] R. Seiler and C. Allegranza, “Mechanism noise signatures: identification and modelling,” in *European Space Mechanisms and Tribology Symposium*, 2009. Cited on page 58.

REFERENCES

- [67] F. Liebold, S. Wiegand, and R. Käso, “Reaction wheel disturbance characterization by analysis of micro-vibration measurements,” in *Applied Mechanics and Materials*, vol. 232, pp. 445–449, Trans Tech Publ, 2012. Cited on page 58.
- [68] A. Prashant, M. Madheswaran, V. Kartik, V. R. Naidu, P. Govindan, and P. Aravindakshan, “System development for micro vibration measurements on spacecrafts,” in *2016 International Conference on Control, Instrumentation, Communication and Computational Technologies (ICCICCT)*, pp. 98–103, IEEE, 2016. Cited on page 58.
- [69] H. Zhu, S. He, Z. Xu, X. Wang, C. Qin, J. Yang, and L. Zhang, “Iterative feedback control based on frequency response model for a six-degree-of-freedom micro-vibration platform,” *Journal of Vibration and Control*, 2021. Cited on page 59.
- [70] Z.-D. Xu, Z.-H. Chen, X.-H. Huang, C.-Y. Zhou, Z.-W. Hu, Q.-H. Yang, and P.-P. Gai, “Recent advances in multi-dimensional vibration mitigation materials and devices,” *Frontiers in Materials*, vol. 6, p. 143, 2019. Cited on page 59.
- [71] M. B. McMickell, T. Kreider, E. Hansen, T. Davis, and M. Gonzalez, “Optical payload isolation using the miniature vibration isolation system (mvis-ii),” in *Industrial and Commercial Applications of Smart Structures Technologies 2007*, vol. 6527, p. 652703, International Society for Optics and Photonics, 2007. Cited on page 59.
- [72] S. Yi, B. Yang, and G. Meng, “Microvibration isolation by adaptive feedforward control with asymmetric hysteresis compensation,” *Mechanical Systems and Signal Processing*, vol. 114, pp. 644–657, 2019. Cited on page 59.
- [73] R. A. Masterson, D. W. Miller, and R. L. Grogan, “Development and validation of reaction wheel disturbance models: empirical model,” *Journal of sound and vibration*, vol. 249, no. 3, pp. 575–598, 2002. Cited on page 60.
- [74] J. Shields, C. Pong, K. Lo, L. Jones, S. Mohan, C. Marom, I. McKinley, W. Wilson, and L. Andrade, “Characterization of cubesat reaction wheel assemblies,” *Journal of Small Satellites*, vol. 6, no. 1, pp. 565–580, 2017. Cited on page 60.
- [75] P. M. Le, *Micro-disturbances in reaction wheels*. PhD thesis, 2017. Cited on page 60.
- [76] Z. J. Geng and L. S. Haynes, “Six degree-of-freedom active vibration control using the stewart platforms,” *IEEE Transactions on control systems technology*, vol. 2, no. 1, pp. 45–53, 1994. Cited on page 61.
- [77] P. Orlov, *Fundamentals of Machine Design*, vol. 5. MIR Moscow, 1977. Cited on page 65.
- [78] M. Verma, V. Lafarga, and C. Collette, “Perfect collocation using self-sensing electromagnetic actuator: Application to vibration control of flexible structures,” *Sensors and Actuators A: Physical*, vol. 313, p. 112210, 2020. Cited on pages 70 and 107.

-
- [79] C. Collette and F. Matichard, "Sensor fusion methods for high performance active vibration isolation systems," *Journal of sound and vibration*, vol. 342, pp. 1–21, 2015. Cited on page 70.
- [80] R. Lorenz, "Self-sensing motion control for electrical and hybrid electrical vehicles," *IEE Power Conversions & Applications Lecture, Midlands Engineering Centre, Birmingham*, 2001. Cited on page 70.
- [81] A. Technologies, "Agilent 4294a precision impedance analyzer - data sheet." Cited on page 71.
- [82] G. Cazzulani, F. Resta, F. Ripamonti, and R. Zanzi, "Negative derivative feedback for vibration control of flexible structures," *Smart Materials and Structures*, vol. 21, no. 7, p. 075024, 2012. Cited on page 73.
- [83] R. Jamshidi and C. Collette, "Optimal negative derivative feedback controller design for collocated systems based on h_2 and h_∞ method," *Mechanical Systems and Signal Processing*, vol. 181, p. 109497, 2022. Cited on page 73.
- [84] A. Saberi, P. Sannuti, and B. Chen, *H2 Optimal Control*. Prentice-Hall international series in systems and control engineering, Prentice Hall, 1995. Cited on page 73.
- [85] P. Piezotronics, "Pcb accelerometer - model 352a24 technical specifications." Cited on pages 76 and 83.
- [86] B. Ding, *Development of high resolution interferometric inertial sensors*. PhD thesis, Université Libre de Bruxelles, 2021. Cited on page 81.
- [87] Siemens, "Siemens qsources miniature shaker - data sheet." Cited on page 83.
- [88] P. Stoica, R. L. Moses, *et al.*, *Spectral analysis of signals*. Pearson Prentice Hall Upper Saddle River, NJ, 2005. Cited on page 88.
- [89] V. Lafarga, R. Jamshidi, G. Rodrigues, R. Seiler, and C. Collette, "Multi-degree-of-freedom active isolation platform for microvibrations," *Journal of Spacecraft and Rockets*, vol. 61, no. 1, pp. 16–33, 2024. Cited on page 107.
- [90] M. Verma, V. Lafarga, M. Baron, and C. Collette, "Active stabilization of unmanned aerial vehicle imaging platform," *Journal of Vibration and Control*, vol. 26, no. 19-20, pp. 1791–1803, 2020. Cited on page 107.
- [91] M. Verma, V. Lafarga, T. Dehaeze, and C. Collette, "Multi-degree of freedom isolation system with high frequency roll-off for drone camera stabilization," *IEEE access*, vol. 8, pp. 176188–176201, 2020. Cited on page 107.

REFERENCES

- [92] V. Lafarga, M. Verma, G. Rodrigues, and C. Collette, “Multi degree of freedom micro-vibration isolator with frameless actuators,” in *ECSSMet*, European Space Agency, 2020. Cited on page 108.

Appendices

Appendix A

Equivalence of Force and Motion Transmissibilities

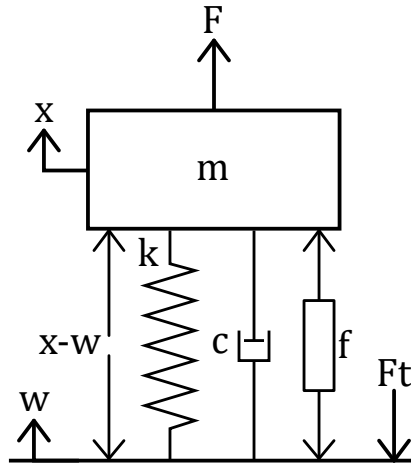


Figure A.1: 1 DOF system with base motion and input forces as inputs, and mass motion and transmitted force as outputs

The equations of motion of the mass, spring dashpot system with input motion at the base shown in Fig. A.1 can be written as

$$ms^2X + cs(X - W) + k(X - W) = F + f \quad (\text{A.1})$$

$$F_t = k(X - W) + cs(X - W) - f \quad (\text{A.2})$$

where m is the mass of the system, k is the stiffness, c is the damping, F and f represent an external force acting on the system and the actuator force respectively. F_t is the transmitted force to the base. X and W are the motion of the mass and the base respectively, and s is the Laplace variable.

From the above system of equations, the motion transmissibility T_{WX} , force

APPENDIX A. EQUIVALENCE OF FORCE AND MOTION TRANSMISSIBILITIES

transmissibility T_{FFt} and compliance T_{FX} can be extracted as a function of the actuator force. This is done in order to compare the effect of different control strategies on these transfer functions

$$T_{WX} = \frac{X}{W} = \frac{k + cs}{ms^2 + cs + k} + \frac{1}{ms^2 + cs + k} \frac{f}{W} \quad (\text{A.3})$$

$$T_{FFt} = \frac{F_t}{F} = \frac{k + cs}{ms^2 + cs + k} - \frac{ms^2}{ms^2 + cs + k} \frac{f}{F} \quad (\text{A.4})$$

$$T_{FX} = \frac{X}{F} = \frac{1}{ms^2 + cs + k} + \frac{1}{ms^2 + cs + k} \frac{f}{F} \quad (\text{A.5})$$

By setting the input force by the actuator to zero, simulating a system without active control, it can be seen that both the motion and force transmissibility are of equal magnitude. With only a difference in sign due to the convention chosen.

In order to introduce relative motion control into the system, let

$$f = -H(s)(X - W) \quad (\text{A.6})$$

where $H(s)$ represents the controller used. Substituting Eq. (A.6) into Eq. (A.3) results in

$$T_{WX} = \frac{k + cs + H(s)}{ms^2 + cs + k + H(s)} \quad (\text{A.7})$$

Doing the same with Eq. (A.4) requires solving for Eq. (A.5) too, resulting in the equations

$$T_{FFt} = \frac{k + cs}{ms^2 + cs + k} + \frac{ms^2 H(s)}{ms^2 + cs + k} \frac{X}{F} \quad (\text{A.8})$$

$$T_{FX} = \frac{1}{ms^2 + cs + k + H(s)} \quad (\text{A.9})$$

Finally, injecting Eq. (A.9) into Eq. (A.8) and simplifying results in

$$\frac{F_t}{F} = \frac{H(s) + k + cs}{ms^2 + cs + k + H(s)} \quad (\text{A.10})$$

which is equivalent to X/W .

Analogously, absolute motion control can be introduced by substituting Eq. (A.11)

into the set of Eq's. (A.3-A.5)

$$f = -H(s)(X) \quad (\text{A.11})$$

resulting in

$$T_{WX} = \frac{k + cs}{ms^2 + cs + k + H(s)} \quad (\text{A.12})$$

$$T_{FFt} = \frac{H(s) + k + cs}{ms^2 + cs + k + H(s)} \quad (\text{A.13})$$

$$T_{FX} = \frac{1}{ms^2 + cs + k + H(s)} \quad (\text{A.14})$$

The transfer functions T_{FFt} and T_{FX} remain equivalent with both control architectures.

